EMBRY-RIDDLE
Aeronautical University
SCHOLARLY COMMONS

PhD Dissertations and Master's Theses

Summer 8-2021

A Reduced-Order Model Bi-Modal Excitation of a Supersonic Planar Jet

Benjamin Malczewski
malczewb@my.erau.edu

Follow this and additional works at: https://commons.erau.edu/edt

 Part of the Aeronautical Vehicles Commons

Scholarly Commons Citation

Malczewski, Benjamin, "A Reduced-Order Model Bi-Modal Excitation of a Supersonic Planar Jet" (2021). *PhD Dissertations and Master's Theses*. 620.
https://commons.erau.edu/edt/620

This Thesis - Open Access is brought to you for free and open access by Scholarly Commons. It has been accepted for inclusion in PhD Dissertations and Master's Theses by an authorized administrator of Scholarly Commons. For more information, please contact commons@erau.edu.

A REDUCED-ORDER MODEL BI-MODAL EXCITATION OF A SUPERSONIC PLANAR JET

By

Benjamin Malczewski

A Thesis Submitted to the Faculty of Embry-Riddle Aeronautical University

In Partial Fulfillment of the Requirements for the Degree of

Master of Science in Aerospace Engineering

August 2021

Embry-Riddle Aeronautical University

Daytona Beach, Florida

A REDUCED-ORDER MODEL FOR BI-MODAL EXCITATION OF A SUPERSONIC PLANAR JET

By

Benjamin Malczewski

This Thesis was prepared under the direction of the candidate's Thesis Committee Chair, Dr. Reda Mankbadi, Department of Aerospace Engineering, and has been approved by the members of the Thesis Committee. It was submitted to the Office of the Senior Vice President for Academic Affairs and Provost, and was accepted in the partial fulfillment of the requirements for the Degree of Master of Science in Aerospace Engineering.

THESIS COMMITTEE

Chairman, Dr. Reda Mankbadi	Member, Dr. Vladimir Golubev
Member, Dr. William MacKunis	Member, Dr. Tasos Lyrintzis
Graduate Program Coordinator, Dr. Daewon Kim	8/24/2021 Date
Dean of the College of Engineering, Dr. Maj Mirmirani	Date
Associate Provost of Academic Support, Dr. Christopher Grant	Date

ACKNOWLEDGEMENTS

There are several individuals I would like to give special thanks to. Without their support and guidance, this work would not have been possible. First and foremost, I would like to acknowledge my thesis advisor and committee chair, Dr. Reda Mankbadi. He has been my primary source of guidance throughout this process, and his insight and background on the subject matter have proven themselves to be invaluable time and time again throughout this project. I would like to thank my other committee members as well for taking the time to review and assess this work. I would like to give a special thanks to Dr. Chau-Lyan Chang for his assistance with using LASTRAC and taking time out of his schedule to help me when I ran into trouble using the code. Support from the Office of Naval Research under Grant No. N00014-21-1-2102 monitored by Dr. Steven Martens is greatly appreciated. Finally, I would like to thank my family and friends for their motivational support throughout my time working on this project.

ABSTRACT

This work analytically and numerically examines the effects of bi-modal excitation on a Mach 1.5 heated planar jet. Starting with the Navier-Stokes equations, triple decomposition is applied to the flow components. A reduced order model is derived, turning the Navier-Stokes partial differential equations into a set of coupled ordinary differential equations, relating the momentum thickness and amplitudes of a fundamental and subharmonic mode to the streamwise location along the jet. Computational fluid dynamics data from the minor plane of a Mach 1.5 heated rectangular jet is used to verify a hyperbolic tangent profile for the mean flow at various streamwise locations. Locally-parallel linear stability theory is used to compute the shape assumptions for the coherent structure components involved in the set of ordinary differential equations. The set of ordinary differential equations is first solved for a single mode.

The trends for the single mode excitation qualitatively compared well with previous work. In the initial region, the nonlinear amplitude generally agreed well with the linear solution. Bi-modal excitation is then examined for the fundamental Strouhal number 0.10, which has been identified as a dominant noise source. Cases were considered separately with adding the subharmonic and the harmonic as a means of reducing the amplitude of the fundamental. Adding the subharmonic had minimal effects on reducing the fundamental unless both initial amplitudes are large. However, adding the harmonic could be very effective at reducing the fundamental even at low initial amplitudes. It is ultimately determined that adding the subharmonic may or may not be effective as a noise-reducing mechanism but adding the harmonic can be effective depending on the initial phase difference between the two excitations.

TABLE OF CONTENTS

LIST OF FIGURES

Figure Page

Figure Page

Figure Page

LIST OF TABLES

NOMENCLATURE

x^+	Nondimensional streamwise coordinate
y^+	Nondimensional transverse coordinate
u	Streamwise velocity along the x-direction
v	Transverse velocity along the y-direction
w	Spanwise velocity along the z-direction
α	Complex streamwise wave number
$-\alpha_i$	Streamwise growth rate
α_r	Real component of streamwise wave number
β	Initial phase difference between fundamental and subharmonic amplitude
Δ	Laplacian operator
η_x	Nondimensional coordinate where shear layer velocity is half of jet centerline
μ	Kinematic viscosity
ρ	Density
ρ_j	Density at the jet outlet
ϕ	Phase angle of I_{fs}
θ	Momentum thickness
θ^+	Nondimensional momentum thickness
ω	Nondimensional frequency
A	Nonlinear amplitude of fundamental
A_0	Initial amplitude of fundamental
B	Nonlinear amplitude of subharmonic

B_0	Initial amplitude of subharmonic
CC	Complex conjugate
C_r	Phase speed velocity
E_f	Nonlinear amplitude of the fundamental
$E_{f/2}$	Nonlinear amplitude of the subharmonic
E_{2f}	Nonlinear amplitude of the harmonic
f	Dimensional frequency
g_i	Generic flow component
H	Jet height
I_{mf}	Integral representing energy transfer from mean flow to coherent structure
I_{fd}	Integral representing coherent mode dissipation
I_{af}	Integral representing mean flow advection of coherent mode kinetic energy
I_{am}	Mean flow advection integral
I_{md}	Mean flow viscous dissipation integral
I_{fs}	Complex interaction integral between fundamental and subharmonic
I_{ww}	Interaction integral between fundamental and subharmonic
K	Mean flow kinetic energy
k	Eigenfunction normalization coefficient
l_0	Length scale
N	Linear growth rate
n	Spanwise wave number
p	Pressure

Q	Kinetic energy of large-scale structure
q	Kinetic energy of small-scale turbulence
R	Specific gas constant
R^+	Nondimensionalized specific gas constant
Re	Reynolds number
Re_{eff}	Effective Reynolds number
$\tilde{r}_{ij}$	Wave induced stress
St	Strouhal number
T	Temperature
U_j	Jet inlet velocity
U_0	Jet centerline velocity
W	Jet width

1. Introduction

The effect of bi-modal excitation has previously been explored with a Reduced-Order Model (ROM) using an integral technique (Mankbadi, 1985), though this was for a low-speed round jet. Here, a ROM is derived for a supersonic planar jet, and using results from linear stability analysis (Chang, 2004), we are able to perform a similar type of analysis.

1.1. Research Scope

This work examines the effects of bi-modal excitation on the large-scale turbulent structures in a supersonic planar jet using an integral technique. This integral technique is derived by taking the Navier-Stokes equations (NSE) and splitting the flow variables into three parts: a mean flow component, large scale coherent structure, and fine scale random turbulence. With appropriate shape assumptions, the NSE are transformed from a set of partial differential equations (PDE) to a set of coupled ordinary differential equations (ODE) with various integral terms that are functions of momentum thickness. This set of ODE's solves for the momentum thickness and both excitation amplitudes versus streamwise location.

The aforementioned integrals appearing in the ODEs are computed using linear stability theory with NASA's LASTRAC code (Chang, 2004), which takes a mean flow profile as input and outputs the complex streamwise wave number, phase speed velocity, as well as the transverse shape functions. The mean flow profiles are taken to be of the hyperopic tangent shape that we showed to ft the CFD results for a Mach 1.5 heated rectangular jet (Mankbadi & Salehian, 2021). Using the results from LASTRAC, the integrals are computed as functions of momentum thickness.

The solution to the set of ODE's is analyzed in various ways. Firstly, single-mode excitation is analyzed for various Strouhal numbers and initial amplitudes. With single-mode excitation, comparison is made between the initial growth rate of the excitation amplitude from the solution of the ODE's and from linear theory. Similar work has been done by (Dahl et al., 2003; Dahl & Mankbadi, 2002), but for round jets.

Finally, the solutions of the ODE's are presented for bi-modal excitation for the fundamental Strouhal number of 0.10, which has been shown to be a dominant noise source (Mankbadi & Salehian, 2021). The objective is to add either a subharmonic or harmonic excitation that will interact with the fundamental and reduce it. The initial amplitude of the subharmonic and fundamental is desired to be less than or equal to that of the fundamental so that no significant noise sources are added to the jet. Reduction of the fundamental indicates the potential for bi-modal excitation to reduce the peak noise of the jet.

1.2. Relevance of Research

Jet noise is a significant concern for the design of both military and commercial aircraft. There is a lot of interest in mechanisms that can be used to reduce jet noise whether it is for commercial aircraft flying over densely populated areas or military aircraft taking off from an aircraft carrier in close proximity to personnel. There is an interest in the use of rectangular jets particularly in military applications due to the relative ease of integration into an airframe (Chakrabarti et al., 2020a). In the minor plane of high aspect ratio rectangular jets, the jet can be approximated as a 2-dimensional planar jet with an infinite span, which is what the current work focuses on.

Various previous works have focused on the use of single-mode excitation as a means to actively reduce jet noise. Similar to the current work, (Dahl & Mankbadi, 2002; Dahl et al., 2003) have used an integral technique to predict the nonlinear development of wave structures in compressible round jets. Mankbadi (1985) has also used a similar integral approach for bi-modal excitation, but for a low-speed round jet as well. The key difference here is that the integral approach is being used for bi-modal excitation as well as for a supersonic planar jet.

Many previous works use large eddy simulations (LES) as a computational tool to predict and model jet noise such as (Wu et al., 2019; Chakrabarti et al., 2020b; Nichols et al., 2011). LES results are then often compared to experiments. While LES has been shown to resourceful in predicting jet noise and results have compared well to experiments, it is very computationally expensive. For example, Nichols et al. (2011) performed LES using meshes with 45 million and 86 million control volumes using up to 20,000 cores, and simulations still took many days to complete. With the large computational demand of LES, it is useful to have tools with low computational demand that can reasonably predict outcomes from LES. The present work focuses on the use of an integral technique to create a reduced order model that can model the nonlinear amplitudes in bi-modal excitation of a supersonic planar jet as well as the growth of momentum thickness along the streamwise direction. The computations here involve performing linear stability analysis and using those results in relatively simple programs, none of which require the use of computing clusters. Once set up, computations can be run in a matter of seconds as opposed to multiple days. Results can provide reasonable accuracy by which to guide the setup of expensive computations and experiments.

2. Review of Relevant Literature

The current work focuses on bi-modal excitation of a supersonic planar jet. There are various areas of work that are relevant. There have been many studies focused on the excitation of round jets as a means to reduce the noise. Many of these studies used only a single mode for excitation, but there are handful that have used bi-modal. Both will be discussed. Our work focuses on a planar jet, which is an approximate representation of a rectangular jet in its minor plane. Thus, we will cover some past work on rectangular jets. There have also been a few works regarding excitation in rectangular jets, which will also be discussed.

2.1. Single-Mode Excitation

Samimy et al. (2018) have experimentally analyzed high speed shear layers of a round jet. A part of this work involved analyzing the development of large-scale structures in round jets. Here, plasma actuators were used to excite the jet with various Strouhal numbers. They found that the spreading of the jet increased as the excitation Strouhal number approached the "preferred" Strouhal number of the jet. Contours of their results for the unexcited jet and symmetric mode can be seen below.

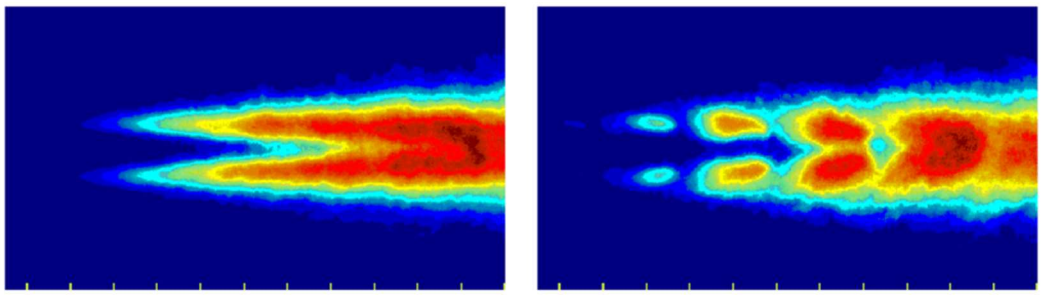

Figure 2.1 Phase-averaged streamwise planar images for unexcited jet (left) and axisymmetric mode (right) (Samimy et al., 2018).

2.2. Supersonic Rectangular Jets

Nichols et al. (2011) performed LES on a Mach 1.4, isothermal, under-expanded, rectangular jet. They observed a flapping motion of the jet in the minor axis. This flapping motion was coupled with strong upstream acoustic radiation, which took the form of a screech tone. Whereas other research has shown axis switching in the plume of the jet (Chakrabarti et al., 2020b), Nichols et al. (2011) showed a smooth transition from a rectangular to circular cross-section of the plume.

Chakrabarti et al. (2020b) examined a heated overexpanded rectangular jet using high-fidelity LES. Here, they showed amplification of the shear layer in the major plane as the plume evolved. In the very near field, they found the dominant noise source to be from an asymmetric mode, but further downstream, a symmetric mode was recovered.

Wu et al. (2019) performed LES on cold rectangular jets to examine screech. They found that the velocity fluctuations near the nozzle exit were low, which suggests that the shear layer is initially laminar. They also showed axis switching for the case of the under-expanded jet.

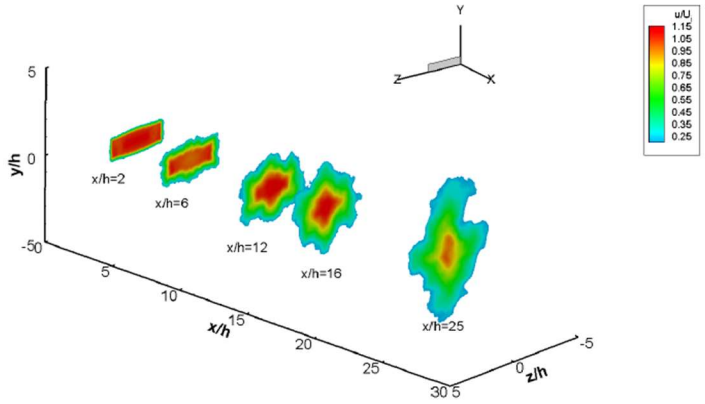

Figure 2.2 Jet plume contours of U/U_j for under-expanded rectangular jet (Wu et al., 2019).

2.3. Excited Rectangular Jets

Crawley et al. (2012) performed experiments with a Mach 1.5 rectangular jet. Excitation was imposed via plasma actuators. They showed that plasma actuation could either amplify or reduce the acoustic radiation depending on the excitation Strouhal number and polar angle.

2.4. Bi-Modal Excitation

Arbey and Ffowcs-Williams (1984) investigated excitation as a means to actively cancel pure tones in a low-speed round jet with experiments. In this work, the jet was excited at harmonically related frequencies. They concluded that harmonics or subharmonic excitation was an effective means of controlling harmonic generation depending on the phase between the two excitations. This was true with both the harmonic and subharmonic, though it was noted that it was more difficult to exert control with the subharmonic.

Mankbadi (1985) looked the interaction between the fundamental and subharmonic instability waves for a turbulent round jet. Similar to the present work, an integral approach was used. It was concluded that at lower Strouhal numbers, only the first subharmonic would amplify by the fundamental, whereas at higher Strouhal numbers, many subharmonics could amplify. The effects of initial amplitude were studied, and it was found that increases in initial amplitude decreased the streamwise lifespan of the fundamental. The initial phase difference between the fundamental and subharmonic were also analyzed, which showed an effect on the growth of the subharmonic.

Mankbadi et al. (1999) used open loop excitation on a Mach 2.1 round jet. This was done for both a single mode and with bi-modal excitation. The bi-modal excitation was done at a fundamental and subharmonic frequency. The bi-modal excitation showed a significant effect on pressure distribution when compared to single-mode excitation.

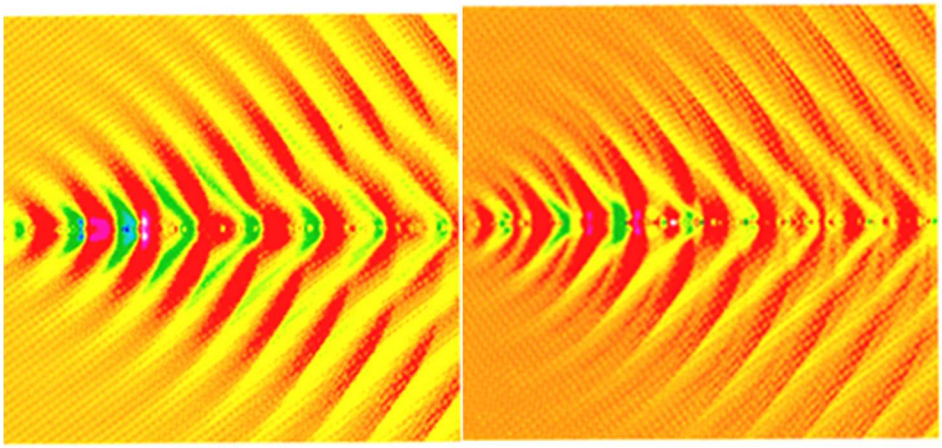

Figure 2.3 Instantaneous pressure distribution with single excitation (left) and bi-modal excitation (right) (Salehian & Mankbadi, 2020b).

3. Formulation of the Problem

Here, we will go into the derivation of our ODE's and shape assumptions. In short, we will start with the Navier-Stokes equations, apply triple decomposition to the flow components. Equations of motion for the mean flow and large-scale structures are then derived. Energy equations are then derived for the mean flow and large-scale structures. We then integrate the energy equations in the transverse direction, make appropriate shape assumptions, then finally arrive at our set of ODE's. Similar derivations have been done in (Dahl & Mankbadi, 2002; Dahl et al., 2003; Mankbadi, 1985), though it should be noted that these were done in cylindrical coordinates and the present derivation will be in cartesian coordinates.

3.1. Equations of Motion

Our first step is to derive the equations of motion. We will first start with the continuity and momentum equations in cartesian coordinates and nondimensional form:

$$\rho_t + (\rho u)_x + (\rho v)_y + (\rho w)_z = 0 \tag{3.1}$$

$$(\rho u)_t + (\rho u^2 + p)_x + (\rho uv)_y + (\rho uw)_z = \frac{1}{Re}\Delta u \tag{3.2}$$

$$(\rho v)_t + (\rho vu)_x + (\rho v^2 + p)_y + (\rho vw)_z = \frac{1}{Re}\Delta v \tag{3.3}$$

$$(\rho w)_t + (\rho wu)_x + (\rho wv)_y + (\rho w^2 + p)_z = \frac{1}{Re}\Delta w \tag{3.4}$$

Here, we define Reynolds number and the Laplacian operator as:

$$Re = \frac{\rho_j U_j H}{\mu} \tag{3.5}$$

$$\Delta = \frac{\partial^2}{\partial x^2} + \frac{\partial^2}{\partial y^2} + \frac{\partial^2}{\partial z^2} \tag{3.6}$$

We will next define the triple decomposition of the flow components. This takes the form of a mean flow, plus a large-scale structure, plus random fine-scale turbulence.

$$g_i(x,y,z,t) = G_i(x,y,z) + g_i'(x,y,z,t) + g_i''(x,y,z,t) \tag{3.7}$$

Here, uppercase variables denote mean flow, $(')$ denotes the large-scale structure, and $('')$ denotes the fine-scale random turbulence. Our definition of the Laplacian operator, equation 3.6, and triple decomposition, Equation 3.7, are then substituted into Equations 3.1-3.4. The product of density with velocity takes the form:

$$(\rho u_i) = (\bar{\rho} + \rho' + \rho")\left(\bar{U}_\iota + u_i' + u_i"\right) = \bar{\rho}\bar{U}_\iota + \widetilde{u_\iota} + \widetilde{u_\iota"} + \rho' u_i' + \rho" u_i" \tag{3.8}$$

Second-order terms, $\rho' u_i'$ and $\rho'' u_i''$, are neglected. We then define:

$$\widetilde{u_\iota} = \bar{\rho}\, u_i' + \rho' \bar{U}_\iota \tag{3.9}$$

$$\widetilde{u_\iota''} = \bar{\rho} u_i'' + \rho'' \bar{U}_\iota \tag{3.10}$$

$$\widetilde{u_a} = \widetilde{u_\iota} + \widetilde{u_\iota"} \tag{3.11}$$

Substituting these relations back into Equations 3.1-3.4 gives:

$$(\bar{\rho} + \rho' + \rho'')_t + (\overline{\rho U} + \widetilde{u_a})_x + (\overline{\rho V} + \widetilde{v_a})_y + (\overline{\rho W} + \widetilde{w_a})_z = 0 \tag{3.12}$$

$$(\overline{\rho U} + \tilde{u}_a)_t + [\bar{P} + p' + p" + (\bar{U} + u' + u")(\overline{\rho U} + \widetilde{u_a})]_x + [(\bar{V} + v' + v")(\overline{\rho U} + \tilde{u}_a)]_y$$
$$+[(\bar{W} + w' + w")(\overline{\rho U} + \tilde{u}_a)]_z = \frac{1}{Re}\Delta(\bar{U} + u' + u") \tag{3.13}$$

$$(\overline{\rho V} + \tilde{v}_a)_t + [(U + u' + u")(\overline{\rho V} + \widetilde{v_a})]_x + [\bar{P} + p' + p" + (\bar{V} + v' + v")(\overline{\rho V} + \tilde{v}_a)]_y$$
$$+[(\bar{W} + w' + w")(\overline{\rho V} + \tilde{v}_a)]_z = \frac{1}{Re}\Delta(\bar{V} + v' + v") \tag{3.14}$$

$$(\overline{\rho W} + \widetilde{w}_a)_t + [(U + u' + u")(\overline{\rho W} + \widetilde{w}_a)]_x + [(\bar{V} + v' + v")(\overline{\rho W} + \widetilde{w}_a)]_y$$
$$+[\bar{P} + p' + p" + (\bar{W} + w' + w")(\overline{\rho W} + \widetilde{w_a})]_z = \frac{1}{Re}\Delta(\bar{W} + w' + w") \tag{3.15}$$

Equations 3.12-3.15 will form the basis of the kinetic energy equations for the mean flow and the large-scale structures.

3.2. The Kinetic Energy Equations

Next, the kinetic energy equations will be derived. This is done for the mean flow, coherent structure, and random turbulence.

3.2.1. Mean Flow Kinetic Energy Equations

Next, Equations 3.12-3.15 are time averaged, giving:

$$(\bar{\rho}\bar{U})_x + (\bar{\rho}\bar{V})_y + (\bar{\rho}W)_z = 0 \tag{3.16}$$

$$\left(\bar{\rho}\bar{U}^2 + \overline{(u' + u")\widetilde{u_a}} + \bar{P}\right)_x + \left(\bar{\rho}\bar{U}\bar{V} + \overline{(v' + v")\widetilde{u_a}}\right)_y + \left(\bar{\rho}\bar{U}\bar{W} + \overline{(w' + w")\,\tilde{u}_a}\right)_z = \frac{1}{Re}\Delta\bar{U} \tag{3.17}$$

$$\left(\bar{\rho}\bar{U}\bar{V} + \overline{(u' + u")\widetilde{v_a}}\right)_x + \left(\bar{\rho}\bar{V}^2 + \overline{(v' + v")\widetilde{v_a}} + \bar{P}\right)_y + \left(\bar{\rho}\bar{V}\bar{W} + \overline{(w' + w")\widetilde{v_a}}\right)_z = \frac{1}{Re}\Delta\bar{V} \tag{3.18}$$

$$\left(\bar{\rho}\bar{U}\bar{W} + \overline{(u' + u")\widetilde{w_a}}\right)_x + \left(\bar{\rho}\bar{W}\bar{V} + \overline{(v' + v")\widetilde{w_a}}\right)_y + \left(\bar{\rho}\bar{W}^2 + \overline{(w' + w")\,\widetilde{w}} + \bar{P}\right)_z = \frac{1}{Re}\Delta\bar{W} \tag{3.19}$$

To obtain the kinetic energy equation for the mean flow, we multiply the x-momentum equation by $\bar{U}$, the y-momentum equation by $\bar{V}$, and the z-momentum equation by $\bar{W}$. The three resultant equations are then added together. We define the mean flow kinetic energy as $K = \frac{1}{2}(\bar{U}^2 + \bar{V}^2 + \bar{W}^2)$. This gives us:

$$\begin{gathered}
\left[\bar{\rho}\bar{U}K + \overline{(u' + u")\,\widetilde{u_a}}\bar{U} + \overline{(u' + u")\widetilde{v_a}}\bar{V} + \overline{(u' + u")\,\widetilde{w}}\bar{W} + \bar{U}\bar{P}\right]_x + \\
\left[\bar{\rho}\bar{V}K + \overline{(v' + v")\,\widetilde{u_a}}\bar{U} + \overline{(v' + v")\widetilde{v_a}}\bar{V} + \overline{(v' + v")\,\widetilde{w_a}}\bar{W} + \bar{V}\bar{P}\right]_y + \\
\left[\bar{\rho}\bar{U}K + \overline{(w' + w")\,\widetilde{u_a}}\bar{U} + \overline{(w' + w")\,\widetilde{v_a}}\bar{V} + \overline{(w' + w")\widetilde{w_a}}\bar{W} + \bar{W}\bar{P}\right]_z - \bar{P}\ \left(\overline{U_x} + \overline{V_y} + \overline{W_z}\right) \\
-\overline{U_x}\,\overline{(u' + u")\,\tilde{u}_a} - \overline{V_x}\,\overline{(u' + u")\,\tilde{v}_a} - \overline{W_x}\,\overline{(u' + u")\,\widetilde{w_a}} \\
-\overline{U_y}\,\overline{(v' + v")\,\tilde{u}_a} - \overline{V_y}\,\overline{(v' + v")\,\tilde{v}_a} - \overline{W_y}\,\overline{(v' + v")\,\widetilde{w_a}} \\
-\overline{U_z}\,\overline{(w' + w")\,\tilde{u}_a} - \overline{V_z}\,\overline{(w' + w")\,\tilde{v}_a} - \overline{W_z}(\overline{w' + w")\,\widetilde{w_a}} \\
= \frac{1}{Re}\left[\Delta K - (U_{ix})^2 - \left(U_{iy}\right)^2 - (U_{iz})^2\right]
\end{gathered} \tag{3.20}$$

Where:

$$(U_{ix})^2 = (\bar{U}_x)^2 + (\bar{V}_x)^2 + (\bar{W}_x)^2 \tag{3.21}$$

$$\left(U_{iy}\right)^2 = \left(\bar{U}_y\right)^2 + \left(\bar{V}_y\right)^2 + \left(\bar{W}_y\right)^2 \tag{3.22}$$

$$(U_{iz})^2 = (\bar{U}_z)^2 + (\bar{V}_z)^2 + (\bar{W}_z)^2 \tag{3.23}$$

We finally obtain:

$$\begin{aligned} &\frac{\partial}{\partial x_j}\left(\bar{\rho}\bar{U}_J K\right) + \frac{\partial}{\partial x_j}\left[\overline{(u_\iota' + u_\iota")\,\widetilde{u_{J_a}}}\bar{U}_\iota + +\bar{U}_J\bar{P}\right] \\ &= \bar{P}\ \frac{\partial U_j}{\partial x_j} + \overline{(u_\iota'\tilde{u}_J + u_\iota"\,\widetilde{u_J"})}\ \frac{\partial \bar{U}_\iota}{\partial x_j} + \frac{1}{Re}\left[\Delta K - \left(\frac{\partial U_i}{\partial x_j}\right)^2\right] \end{aligned} \tag{3.24}$$

It is noted that the coherent perturbation in the above equation includes both the fundamental and subharmonic.

3.2.2. Large Scale Structure Kinetic Energy Equation

The continuity & momentum equations for the large-scale structures are obtained by first phase-averaging the full momentum equations for a given frequency and a given spanwise number, n, then subtracting the mean flow equations from the corresponding phase-averaged equations. The resulting equation contains the entire spanwise mode of that frequency. To separate the special z component, we multiply by $\exp(-i\,n\,z)$ and integrate over z. Higher order terms are neglected, as well as the $(u_i'\tilde{u}_j - \overline{u_i'\tilde{u}_j})$ terms. The governing momentum equations for an (mn) large-scale structures component become:

$$\tilde{\rho}_t + \tilde{u}_x + \tilde{v}_y + \tilde{w}_z = 0 \tag{3.25}$$

$$\begin{aligned} &\tilde{u}_t + (p' + \bar{\rho}\bar{U}u' + \tilde{u}\bar{U})_x + (\bar{\rho}\bar{U}v' + \tilde{u}\bar{V})_y + (\bar{\rho}\bar{U}w' + \tilde{u}\bar{W})_z \\ &\quad + \frac{\partial}{\partial x_j}[< u_j"\widetilde{u"} > - \overline{u_j"\tilde{u}"}] = \frac{1}{Re}\Delta u' \end{aligned} \tag{3.26}$$

$$\tilde{v}_t + (\bar{\rho}\bar{V}u' + \tilde{v}\bar{U})_x + (p' + \bar{\rho}\bar{V}v' + \tilde{v}\bar{V})_y + (\bar{\rho}\bar{V}w' + \tilde{v}\bar{W})_z + \frac{\partial}{\partial x_j}[< u_j"\tilde{v}" > - \overline{u_j"\tilde{v}"}] = \frac{1}{Re}\Delta v' \quad (3.27)$$

$$\tilde{w}_t + (\bar{\rho}\bar{W}u' + \tilde{w}\bar{U})_x + (\bar{\rho}\bar{W}v' + \tilde{w}\bar{V})_y + (p' + \bar{\rho}\bar{W}w' + \tilde{w}\bar{W})_z + \frac{\partial}{\partial x_j}[< u_j"\widetilde{w"} > - \overline{u_j"\widetilde{w}"}] = \frac{1}{Re}\Delta w' \quad (3.28)$$

To obtain the kinetic energy equations for the large-scale structures, we multiply the above phase-averaged momentum equations by their corresponding velocity: u_f', v_f', or $w_f{}'$. These equations are then summed and time averaged, giving the kinetic energy for the (mn) component of the fundamental and subharmonic. Similar to the mean flow, we can describe the kinetic energy of the large-scale structures by $Q = \frac{1}{2}(u'^2 + v'^2 + w'^2)$. The kinetic energy equations for an (mn) component then become:

$$\frac{\partial(\bar{\rho}\bar{U}_j\bar{Q})}{\partial x_j} + \frac{\partial}{\partial x_j}[\overline{\widetilde{u_\iota}\widetilde{r_{\iota j}}} + \overline{\widetilde{u_j}p'} + \overline{\widetilde{u_\iota} < u_\iota'\widetilde{u_j} >}] = \overline{u_j'\frac{\partial p'}{\partial x_j}} - \overline{u_\iota'\widetilde{u_j}}\frac{\overline{\partial U_\iota}}{\partial x_j} + \overline{< u_\iota'\widetilde{u_j} > \frac{\partial u_\iota'}{\partial x_j}} + \overline{\widetilde{r_{\iota j}}\frac{\partial u_\iota'}{\partial x_j}} + \frac{1}{Re}\left[\Delta\bar{Q} - \frac{\partial(\overline{u_{\iota j}'})^2}{\partial x_j}\right] \quad (3.29)$$

Equation 3.29 can be re-written for both the fundamental (f) and subharmonic (s).

$$\frac{\partial(\bar{\rho}\bar{U}_j\bar{Q}_f)}{\partial x_j} + \frac{\partial}{\partial x_j}[\overline{\widetilde{u_{\iota f}}\widetilde{r_{\iota jf}}} + \overline{\widetilde{u_{jf}}p_f'} + \overline{\widetilde{u_{\iota f}} < u_\iota'\widetilde{u_j} >_s}] = \overline{u_{jf}'\frac{\partial p_f{}'}{\partial x_j}} - \overline{u_{\iota f}'\widetilde{u_{jf}}}\frac{\overline{\partial U_\iota}}{\partial x_j} + \overline{< u_\iota'\widetilde{u_j} >_s \frac{\partial u_{\iota f}'}{\partial x_j}} + \overline{\widetilde{r_{\iota jf}}\frac{\partial u_{\iota f}'}{\partial x_j}} + \frac{1}{Re}\left[\Delta\overline{Q_f} - \frac{\partial(\overline{u_{\iota j}'}_f)^2}{\partial x_j}\right] \quad (3.30)$$

$$\frac{\partial(\bar{\rho}\bar{U}_j\bar{Q}_s)}{\partial x_j} + \frac{\partial}{\partial x_j}[\overline{\widetilde{u_{\iota s}}\widetilde{r_{\iota js}}} + \overline{\widetilde{u_{js}}p_s'} - \overline{\widetilde{u_{\iota f}} < u_\iota'\widetilde{u_j} >_s}] = \overline{u_{js}'\frac{\partial p_s{}'}{\partial x_j}} - \overline{u_{\iota s}'\widetilde{u_{js}}}\frac{\overline{\partial U_\iota}}{\partial x_j} - \overline{< u_\iota'\widetilde{u_j} >_s \frac{\partial u_{\iota f}'}{\partial x_j}} + \overline{\widetilde{r_{\iota js}}\frac{\partial u_{\iota s}'}{\partial x_j}} + \frac{1}{Re}\left[\Delta\overline{Q_s} - \frac{\partial(\overline{u_{\iota j}'}_s)^2}{\partial x_j}\right] \quad (3.31)$$

3.2.3. Fine-Scale Turbulence Kinetic Energy Equations

In a similar process to the large-scale structure, we can obtain the kinetic energy equation for the small-scale turbulence. We will start by subtracting the mean flow continuity equation and the large-scale structure continuity equations from the full one in Equation 3.1. The same process is also done for the momentum equations.

$$\widetilde{\rho"}_t + \widetilde{u"}_x + \widetilde{v"}_y + \widetilde{w"}_z = 0 \tag{3.32}$$

$$\widetilde{u"}_t + \left(\bar{\rho}\bar{U}u" + \widetilde{u"}\bar{U}\right)_x + \left(\bar{\rho}\bar{U}v" + \widetilde{u"}\bar{V}\right)_y + \left(\bar{\rho}\bar{U}w" + \widetilde{u"}\bar{W}\right)_z - \frac{\partial}{\partial x_j}[< u_j"\widetilde{u"} > - \overline{u_j"\tilde{u}"}] = \frac{1}{Re}\Delta u" \tag{3.33}$$

$$\widetilde{v"}_t + \left(\bar{\rho}\bar{V}u" + \tilde{v}"\bar{U}\right)_x + \left(p" + \bar{\rho}\bar{V}v" + \widetilde{v"}\bar{V}\right)_y + \left(\bar{\rho}\bar{V}w" + \widetilde{v"}\bar{W}\right)_z - \frac{\partial}{\partial x_j}[< u_j"\widetilde{v"} > - \overline{u_j"\tilde{v}"}] = \frac{1}{Re}\Delta v" \tag{3.34}$$

$$\widetilde{w"}_t + \left(\bar{\rho}\bar{W}u" + \widetilde{w"}\bar{U}\right)_x + \left(\bar{\rho}\bar{W}v" + \widetilde{w"}\bar{V}\right)_y + \left(p" + \bar{\rho}\bar{W}w" + \widetilde{w"}\bar{W}\right)_z - \frac{\partial}{\partial x_j}[< u_j"\widetilde{w"} > - \overline{u_j"\tilde{w}"}] = \frac{1}{Re}\Delta w" \tag{3.35}$$

We then multiply each of the above momentum equations with their respective turbulent velocity, u_i''. The resultant equations are then time averaged and added together. Triple correlations with an odd number of random components are taken to be zero, and those with an even number of random components are non-zero. We can define:

$$q = \frac{1}{2}\left(\overline{u"^2} + \overline{v"^2} + \overline{w"^2}\right) \tag{3.36}$$

$$\tilde{r}_{ij} = < u_i"\widetilde{u"}_j > - \overline{u_i"u_j"} \tag{3.37}$$

Finally, we obtain:

$$\frac{\partial(\bar{\rho}\,\bar{U}\,q)}{\partial x_j} + \frac{\partial}{\partial x_j}\left[\overline{\widetilde{r_{ij}}u_i'} + \overline{\widetilde{u_j}"(p" + q)} + \overline{\widetilde{u_j}q}\right]$$

$$= -\overline{u_i"\widetilde{u_j}"}\frac{\partial \bar{U}}{\partial x_j} - \overline{\widetilde{r_{ij}}\frac{\partial u_i'}{\partial x_j}} + \frac{1}{Re}\left[\overline{u_j"\,\Delta\,u_j"}\right] \qquad (3.38)$$

3.3. Integral Form of the Energy Equation

With the kinetic energy equations derived, we can now obtain the integral equations. First, we will make some assumptions to simplify the problem:

1. The advection of the kinetic energy by each flow component by the mean flow is much larger than that by the perturbation components. Consequently, the second square bracket, [ ], on the left-hand side of the kinetic energy equations is neglected relative to the first.
2. We will ignore the pressure-velocity correlation of the mean flow, $\left(\overline{u'p_x'} + \overline{v'p_y'} + \overline{w'p_z'}\right)$. This term was kept in (Lee & Liu, 1998; Dahl & Mankbadi, 2002), but was later shown by Dahl et al. (2003) to be negligible.
3. Boundary layer-type approximations are made. We will assume that $\bar{W}, \bar{V}$ are smaller than $\bar{U}$ and $\frac{\partial(\bar{\ })}{\partial x}, \frac{\partial(\bar{\ })}{\partial z} \ll \frac{\partial(\bar{\ })}{\partial y}$ for all mean quantities. This is clearly shown in Figure 3.1. This will not be applied to fluctuating quantities.
4. Reynolds stresses of the coherent structure component, $(\overline{u'\tilde{v}})$, are much larger than the other components. Simulations by Salehian and Mankbadi (2019, 2020a) have showed this to be true.

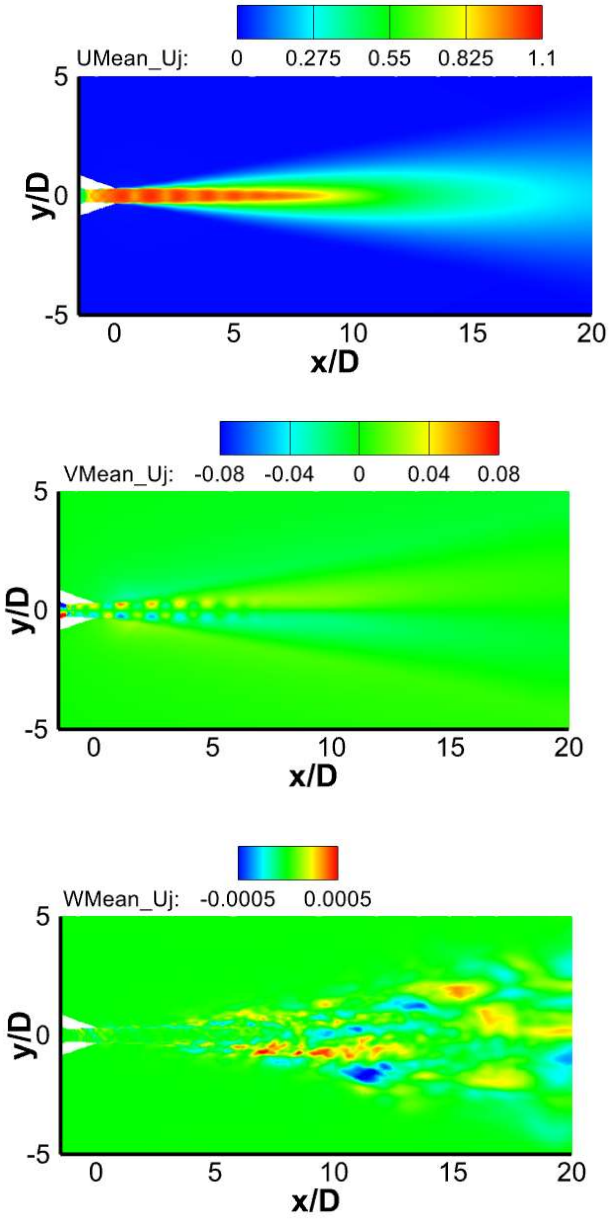

Figure 3.1 Simulations of unexcited Mach 1.5 jet: $\bar{U}/U_j$ (top), $\bar{V}/U_j$ (middle), $\bar{W}/U_j$ (bottom). Salehian and Mankbadi (2019, 2020a).

With the above simplifications, we can then integrate and average over the z-direction, which results in the time-averaged quantities being independent of z, though it is noted that the wave components will include a spanwise wavenumber, n. Integrating

across the y-direction causes the diffusion terms to vanish. We finally arrive at the following equations for the mean flow, fundamental, subharmonic, and turbulence:

$$\frac{d}{dx}\int_{-\infty}^{\infty}\frac{1}{2}\rho\overline{U}^3\,dy = -\int_{-\infty}^{\infty}(-\overline{v_f'\tilde{u}_f})\;\overline{U}_y\,dy - \int_{-\infty}^{\infty}\overline{(-v_s'\tilde{u}_s)}\;\overline{U}_y\,dy$$
$$-\frac{1}{Re}\int_{-\infty}^{\infty}\left(\overline{U}_y\right)^2 dy - \int_{-\infty}^{\infty}(-\overline{u''\tilde{v}''})\;\overline{U}_y\,dy \tag{3.39}$$

$$\frac{d}{dx}\int_{-\infty}^{\infty}\bar{\rho}\overline{U}\bar{Q}_f\,dy = \int_{-\infty}^{\infty}\overline{(-u_f'\tilde{v}_f)}\,\overline{U}_y\,dy - \int_{-\infty}^{\infty}\overline{\left\{< -u_j'\tilde{u}_j >_s \frac{\partial u_{if}'}{\partial x_j}\right\}}\,dy$$
$$-\frac{1}{Re}\int_{-\infty}^{\infty}\left[(\overline{u_{ix}'})^2 + \left(\overline{u_{iy}'}\right)^2 + (\overline{u_{iz}'})^2\right]_f dy - \int_{-\infty}^{\infty}\Phi_f dy \tag{3.40}$$

$$\frac{d}{dx}\int_{-\infty}^{\infty}\bar{\rho}\overline{U}\overline{Q_s}\,dy = \int_{-\infty}^{\infty}\overline{(-u_s'\tilde{v}_s)}\,\overline{U}_y\,dy + \int_{-\infty}^{\infty}\overline{\left\{< -u_i'\tilde{u}_j >_s \frac{\partial u_{if}'}{\partial x_j}\right\}}\,dy$$
$$-\frac{1}{Re}\int_{-\infty}^{\infty}\left[(\overline{u_{ix}'})^2 + \left(\overline{u_{iy}'}\right)^2 + (\overline{u_{iz}'})^2\right]_s dy - \int_{-\infty}^{\infty}\Phi_s dy \tag{3.41}$$

$$\frac{d}{dx}\int_{-\infty}^{\infty}\bar{\rho}\overline{U}\bar{q}\,dy = \int_{-\infty}^{\infty}(-\overline{v''\tilde{u}''})\;\overline{U}_y\,dy$$
$$+\int_{-\infty}^{\infty}\Phi_f dy + \int_{-\infty}^{\infty}\Phi_s dy - \frac{1}{Re}\int_{-\infty}^{\infty}[-\overline{u_j''\,\Delta\,u_j''}\,]dy \tag{3.42}$$

Where:

$$\Phi = \overline{\tilde{r}_{ij}\frac{\partial u_i'}{\partial x_j}} \tag{3.43}$$

We note that:

$$\int_{-\infty}^{\infty}(-\overline{v'\tilde{u}})\;\overline{U}_y\,dy = \int_{-\infty}^{\infty}(-\overline{\rho v'u'} + \overline{\rho' v'U}\,)\;\overline{U}_y\,dy \tag{3.44}$$

In Equation 3.44, Dahl and Mankbadi (2002) kept the second term on the right-hand side. Dahl et al. (2003) later showed that this term was negligible relative to the first.

The physical interpretation of the terms appearing in the energy equation is clear. For the mean flow, the left side is the mean flow advection and the mean flow kinetic energy.

The first and second term on the right-hand side of Equation 3.39 is the energy transfer from the mean flow to the coherent structure, and the third term is the viscous dissipation of the mean flow energy. For the coherent mode, Equations 3.40 and 3.41, the left-hand side is the mean flow advection of the coherent mode kinetic energy. On the right-hand side, the first term is the energy transfer from the mean flow to the coherent mode, the second term is the fundamental-subharmonic interaction, the third term is the coherent mode energy dissipation, and the last term is the interaction with the fine-scale turbulence. In Equation 3.42, the left-hand side is the advection by the mean flow. On the right-hand side, the first term is the production by the mean flow, the second and third terms are the interaction with the waves, and the last term is the turbulence dissipation.

It is noted that the terms containing coherent stresses multiplied by coherent strain represents wave-wave interactions. Because of the assumed periodicity, the time-average of triple correlation frequencies, k, l, p, is zero unless $k \pm l = \pm p$. We then say that:

$$(-\overline{\tilde{v}'\tilde{u}}) = \sum_{mn} (v'_{mn}\tilde{u}^*_{mn}) + CC + \sum_{m,k,l;k\neq l} v'_{ml}\tilde{u}^*_{mk} \exp(i(N_k - N_l)z) + CC \qquad (3.45)$$

Above, the first summation is independent of z. The second summation is dependent on z and can change the interaction in the z-direction. It exists only if there various N of the same frequency. These terms disappear when integrated over z. Thus, they redistribute the mean flow energy over z, but goes to zero when integrated. Thus, the mean flow production of the waves is given by the linear superposition of each frequency component stress. Let us consider the wave-wave interaction term:

$$\int_{-\infty}^{\infty} \overline{\left\{ < -u'_i\tilde{u}_j > \frac{\partial u'}{\partial x_j} \right\}} \, dy \qquad (3.46)$$

Because of the time average and integration over z, the interaction among three waves, $m, k, l,$ is generally zero, unless:

$$\omega_k \pm \omega_l = \pm \omega_m \tag{3.47}$$

$$n_k \pm n_l = \pm n_m \tag{3.48}$$

This not a very restrictive condition. Thus, two waves can generate other waves and the process continues. However, we are only considering the interactions between the subharmonic and the fundamental.

3.4. Turbulence and Effective Reynolds Number

We are trying to replicate a high Reynolds number turbulent rectangular jet. Mankbadi (1985, 1991) has shown how to properly account for this where 2-way turbulence-coherent structure interactions are considered. Though this is a complex process, we can use a simple approach, which has been used successfully.

We must first make a few assumptions. First, we will assume that the effect of the coherent structure on the background random turbulence is negligible. However, the effect of the random turbulence on the coherent structure is considered. We will assume that the eddy viscosity hypothesis applies to both the mean flow and the coherent structure when considering turbulence effects. Finally, we will assume that the eddy viscosity of the turbulence-coherent structure interaction is the same as that of the turbulence-mean flow interaction (Reynolds & Hussain, 1972). Thus:

$$\bar{\mu}_t = \tilde{\mu}_t = \mu_t \tag{3.49}$$

where ($\bar{}$) denotes the meanflow, ($\tilde{}$) denotes the coherent structure, and the subscript *"t"* denotes turbulence. We will use an effective viscosity, $\mu_{eff} = \mu + \mu_t$, where μ is the

molecular viscosity and μ_t is the turbulent viscosity. The effective Reynolds number can be described as:

$$\frac{1}{Re_{eff}} = \frac{1}{Re_l} + \frac{1}{Re_t} \tag{3.50}$$

In the present analysis, an algebraic turbulence model is used to model the effective Reynolds number. The model used is similar to the Wind-US code (Thomas, 1979), which uses the PDT model:

$$\nu_t = C^2 U^2 / \left[\frac{\partial U}{\partial y}\right] \tag{3.51}$$

We can simplify the above equation and obtain the same formular proposed in Schlichting (1960).

$$\nu_t = C^2 U \theta^+ \tag{3.52}$$

The effective Reynolds number can then be written as:

$$\frac{1}{Re_{eff}} = \frac{\nu + \nu_t}{\frac{1}{2}HU} = \frac{1}{Re} + \frac{C^2 U \theta^+}{\frac{1}{2}HU} = \frac{1 + Re\ C\ \theta^+}{Re} \tag{3.53}$$

$$Re_{eff} = \frac{1}{\frac{1}{Re} + c\theta^+} \tag{3.54}$$

Since the Reynolds number is very large in this case, Equation 3.54 can be simplified:

$$Re_{eff} = \frac{1}{c\ \theta^+} \tag{3.55}$$

Above, the coefficient, c, is determined by solving the final ODE equations without excitation. The growth of momentum thickness is then compared to the momentum thickness from the CFD results by Mankbadi and Salehian (2021). Results of this process are shown later in Section 3.6.

In the present analysis, Re is replaced by Re_{eff}. It should be noted that the use of effective Reynolds number is derived for use in the nonlinear solution to the ODE's. Linear stability analysis will still use the very high laminar Reynolds number. Thus, the results from linear stability analysis are effectively inviscid and independent of Re_{eff}.

Thus, instead of linking the turbulence explicitly in the integrated equation, we absorb it in the effective Reynolds number. Thus, the integrated equations for the planar laminar shear layer reduce to:

$$\frac{d}{dx}\int_{-\infty}^{\infty}\frac{1}{2}\rho\overline{U}^3\,dy = -\int_{-\infty}^{\infty}-\overline{\bar{\rho}u_f'v_f'}\;\overline{U}_y\,dy - \int_{-\infty}^{\infty}-\bar{\rho}\overline{u_s'v_s'}\;\overline{U}_y\,dy - \frac{1}{Re}\int_{-\infty}^{\infty}\left(\overline{U}_y\right)^2 dy \tag{3.56}$$

$$\frac{d}{dx}\int_{-\infty}^{\infty}\bar{\rho}\overline{U}\overline{Q}_f\,dy = \int_{-\infty}^{\infty}-\overline{\bar{\rho}u_f'v_f'}\,\overline{U}_y\,dy - \int_{-\infty}^{\infty}\overline{\left\{< -u_j'\tilde{u}_j >_s \frac{\partial u_{if}'}{\partial x_j}\right\}}\,dy - \frac{1}{Re}\int_{-\infty}^{\infty}\left[\overline{(u_{ix}')}^2 + \overline{\left(u_{iy}'\right)}^2 + \overline{(u_{iz}')}^2\right]_f dy \tag{3.57}$$

$$\frac{d}{dx}\int_{-\infty}^{\infty}\bar{\rho}\overline{U}\overline{Q}_s\,dy = \int_{-\infty}^{\infty}-\overline{\bar{\rho}u_s'v_s'}\,\overline{U}_y\,dy - \int_{-\infty}^{\infty}\overline{\left\{< -u_j'\tilde{u}_j >_s \frac{\partial u_{is}'}{\partial x_j}\right\}}\,dy - \frac{1}{Re}\int_{-\infty}^{\infty}\left[\overline{(u_{ix}')}^2 + \overline{\left(u_{iy}'\right)}^2 + \overline{(u_{iz}')}^2\right]_s dy \tag{3.58}$$

3.5. Shape Assumptions

To solve the system of integrated energy equations, shape assumptions need to be made for the transverse profiles. The coherent structure profiles are assumed to follow that of the locally parallel linear stability theory. Each coherent component can then be written as:

$$u_i' = \hat{u}_i(y,x)A(x)\exp\left[(i\int_0^x \alpha_r\,d\xi) - i\omega t + inz\right] + CC \tag{3.59}$$

Here, the (^) denotes the eigenfunctions representing the transverse shape function in the y-direction. These eigenfunctions are dependent on the mean flow profile at a particular streamwise location in the jet. In Equation 3.59, n is the wave number in the z-direction and CC denotes the complex conjugate. $A(x)$ is the complex amplitude function of x and is determined with nonlinear analysis. Here, the linear growth rate is determined by the imaginary component $(-\alpha_i)$ is absorbed into $A(x)$. Since we are only considering the fundamental and subharmonic modes, we get:

$$g_f'(x,y,z,t) = A(x)\hat{g}_f\big(y,x,\omega_f,n_f\big)\exp\left[i\int_0^x \alpha_{rf}(\xi)d\xi - i\omega_f t + i\beta)\right] + CC \quad (3.60)$$

$$g_s'(x,y,z,t) = B(x)\hat{g}_s(y,x,\omega_s,n_s)\exp\left[i\int_0^x \alpha_{rs}(\xi)d\xi - i\omega_s t)\right] + CC \quad (3.61)$$

Here, β is the initial phase difference between the two modes. We normalize the eigenfunctions such that:

$$\int_0^\infty (|\hat{u}|^2 + |\hat{v}|^2 + |\hat{w}|^2)dy = 1 \quad (3.62)$$

We characterize the mean flow by the momentum thickness, θ, rather than a physical distance, x, therefore making the integral terms in our ODE's functions of momentum thickness. With this shape assumption, our system of ODE's describing the mean flow and the nonlinear amplitudes become:

$$\frac{d\theta}{dx}\frac{dI_{am}}{d\theta} = -|A|^2 I_{mf} - |B|^2 I_{ms} - \frac{1}{Re}I_{md} \quad (3.63)$$

$$\frac{d\big(I_{af}|A|^2\big)}{dx} = |A|^2\left(I_{mf} - \frac{1}{Re}I_{fd}\right) - I_{ww}|A||B|^2 \quad (3.64)$$

$$\frac{d(I_{as}|B|^2)}{dx} = |B|^2\left(I_{ms} - \frac{1}{Re}I_{sd}\right) + I_{ww}|A||B|^2 \quad (3.65)$$

The mean flow is affected by the coherent structure since the equation for the momentum thickness includes the energy absorbed by the coherent structure from the mean flow on the right-hand side. We then define the integrals in Equations 3.63-3.65 as:

$$I_{am} = \frac{1}{2}\int_0^\infty \bar{\rho}\bar{U}^3\, dy \tag{3.66}$$

$$I_{mf} = -\int_0^\infty (\hat{v}\hat{u}^* + CC)_f\, \bar{\rho}\, \frac{\partial \bar{U}}{\partial y}\, dy \tag{3.67}$$

$$I_{ms} = -\int_0^\infty (\hat{v}\hat{u}^* + CC)_s\, \bar{\rho}\, \frac{\partial \bar{U}}{\partial y}\, dy \tag{3.68}$$

$$I_{md} = \int_0^\infty \left(\bar{U}_y\right)^2 \quad dy \tag{3.69}$$

$$I_{af} = \int_0^\infty (|\hat{u}|^2 + |\hat{v}|^2 + |\hat{w}|^2)_f\, \bar{\rho}\ \bar{U}\ \ dy \tag{3.70}$$

$$I_{as} = \int_0^\infty (|\hat{u}|^2 + |\hat{v}|^2 + |\hat{w}|^2)_s\ \bar{\rho}\, \bar{U}\ \ dy \tag{3.71}$$

$$I_{fd} = 2\int_0^\infty \left[(|\alpha|^2 + n^2)\,(|\hat{u}|^2 + |\hat{v}|^2 + |\hat{w}|^2) + \left(\left|\frac{\partial \hat{u}}{\partial y}\right|^2 + \left|\frac{\partial \hat{v}}{\partial y}\right|^2 + \left|\frac{\partial \hat{w}}{\partial y}\right|^2\right)\right]_f dy \tag{3.72}$$

$$I_{sd} = 2\int_0^\infty \left[(|\alpha|^2 + n^2)\,(|\hat{u}|^2 + |\hat{v}|^2 + |\hat{w}|^2) + \left(\left|\frac{\partial \hat{u}}{\partial y}\right|^2 + \left|\frac{\partial \hat{v}}{\partial y}\right|^2 + \left|\frac{\partial \hat{w}}{\partial y}\right|^2\right)\right]_s dy \tag{3.73}$$

In Equations 3.64 and 3.65, the term I_{ww} represents the interaction between the fundamental and subharmonic modes.

$$I_{ww} = -\left\{\left(e^{i\beta_0 + i\int_0^x (\alpha_{rf} - 2\alpha_{rs})d\xi}\right) I_{fs} + CC\right\} \tag{3.74}$$

$$I_{fs} = \int_{-\infty}^\infty \left\{\hat{u}_s^*\hat{u}_s^*\, \frac{\partial \hat{u}_f}{\partial x} + \hat{u}_s^*\hat{v}_s^*\, \left(\frac{\partial \hat{u}_f}{\partial y} + \frac{\partial \hat{v}_f}{\partial x}\right) + \hat{v}_s^*\hat{v}_s^*\, \frac{\partial \hat{v}_f}{\partial y} + \hat{w}_s^*\hat{u}_s^*\, \frac{\partial \hat{w}_f}{\partial x} + \hat{w}_s^*\hat{v}_s^*\, \frac{\partial \hat{w}_f}{\partial y}\right\} \tag{3.75}$$

I_{fs} is a complex quantity. Both the real and imaginary components are significant in our analysis. We then write:

$$I_{fs} = \left|I_{fs}\right| e^{i\phi} \tag{3.76}$$

$$\psi = \int_0^x \left(\alpha_{rf} - 2\alpha_{rs}\right) d\xi \tag{3.77}$$

We then write:

$$I_{ww} = -2 \left|I_{fs}\right| \cos\{\phi + \beta + \psi\} \tag{3.78}$$

Which we can approximately write as:

$$I_{ww} = -2 \left|I_{fs}\right| \cos\{\phi + \beta\} \tag{3.79}$$

We can simplify Equation 3.75. We will assume that $\frac{\partial}{\partial x}$ are small and we will neglect the velocity in the z-direction, thus $\widehat{w}$ is zero. Equation 3.75 significantly reduces to:

$$I_{fs} = \int_{-\infty}^{\infty} \left\{ \hat{u}_s^* \hat{v}_s^* \left(\frac{\partial \hat{u}_f}{\partial y} \right) + \hat{v}_s^* \hat{v}_s^* \frac{\partial \hat{v}_f}{\partial y} \right\} dy \tag{3.80}$$

3.6. Calculation of the Effective Reynolds Number

To determine Re_{eff}, results from Dahl and Mankbadi (2002) are used. The Reynolds number was fitted as a function of momentum thickness; thus, it is a variable quantity. A multiplier was then applied to the fitted Reynolds number, which compensates for differences in the jets being considered.

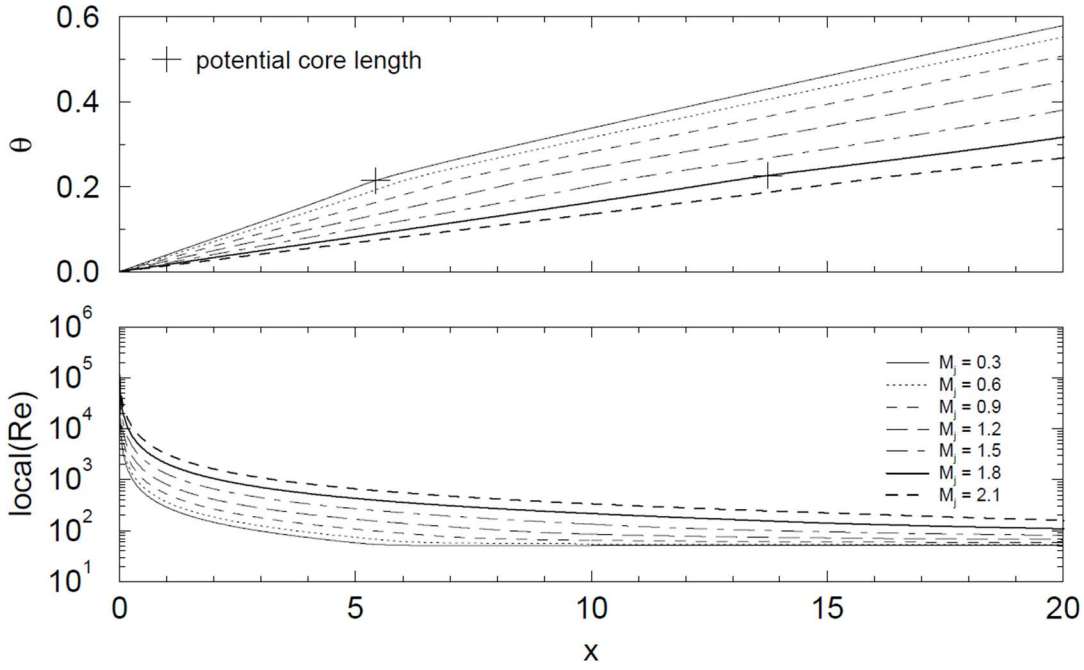

Figure 3.2 Local Reynolds number from Dahl and Mankbadi (2002).

The multiplier was determined by solving Equation 3.63 with only the viscous terms. The multiplier was chosen such that the solution to Equation 3.63 fit well with the CFD results from Mankbadi and Salehian (2021). This gives the effective Reynolds number in the form presented in Equation 3.55. The results for comparison and effective Reynolds number can be seen below.

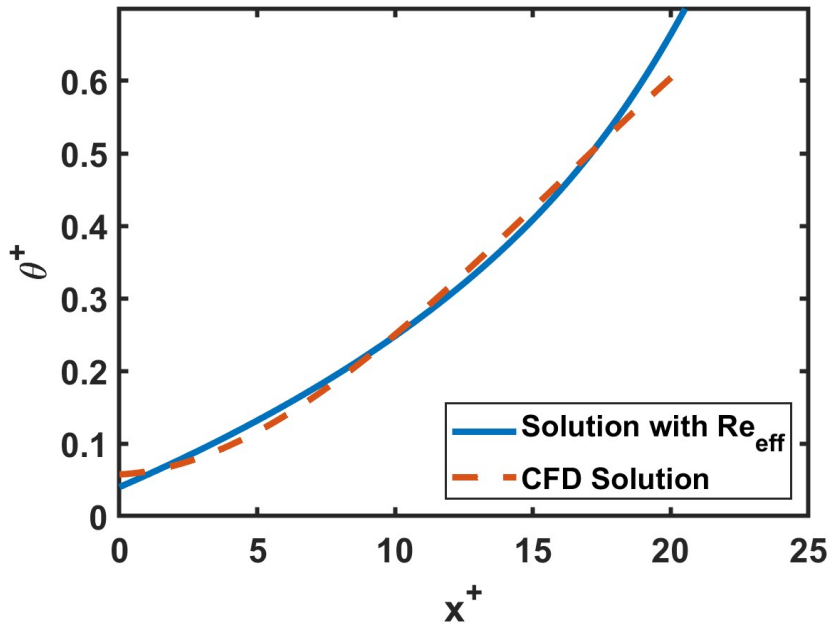

Figure 3.3 Solution to ODE with only viscous terms and CFD solution from Mankbadi and Salehian (2021).

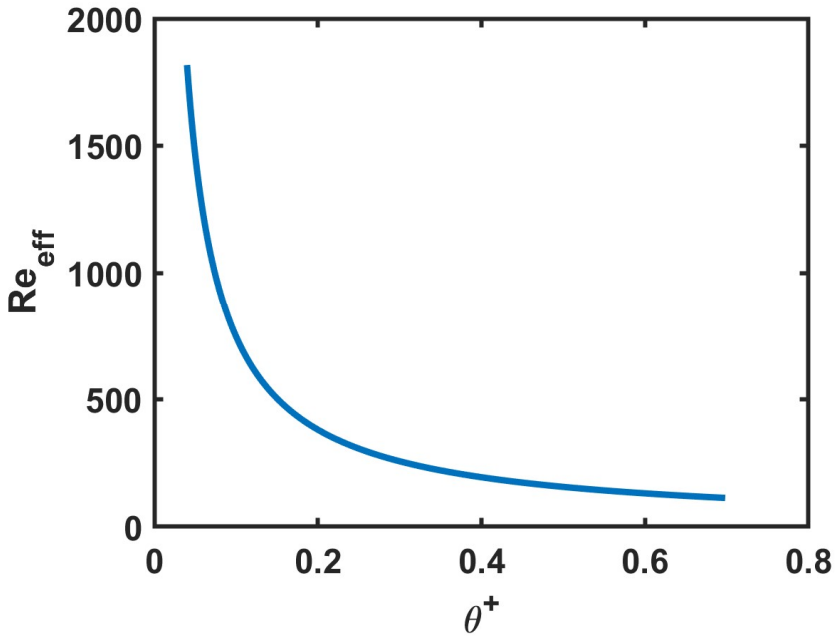

Figure 3.4 Effective Reynolds number

4. Calculations of the Integrals using the Shape Assumptions

To obtain the integrals appearing in the set of ODES obtained in Chapter 3 (Equations 3.63-3.65), we need to make some assumptions regarding the transverse shapes of the base flow as well as the coherent structure. This will be discussed in Sections 4.1 and 4.2, respectively, and is followed by calculations of the needed integrals in Section 4.3.

4.1. The Base Flow

The mean flow is needed, not only to be used for calculating the integrals involved but is also an input for calculating the coherent structure profiles based on the locally-parrel linear instability theory, which will be discussed in section 4.2. In this work, we are trying to represent the coherent structure in the rectangular supersonic jet of the University of Cincinnati facility (Mora et al., 2016). This jet was also simulated in (Salehian & Mankbadi, 2019; Mankbadi & Salehian, 2021) [MS]. The jet considered is perfectly expanded with an exit Mach number of 1.5 and heated with total temperature ratio of 3. The jet has a width, W, and heigh, H, with an aspect ratio of 2, as shown in Figure 4.1.

In the following, spatial coordinates are non-dimensionalized by a length scale, which was taken to be the half-height of the jet (H/2); $u, v,$ and w velocities by a velocity scale; temperature by a temperature scale; density by a density scale; and pressure by $\rho_\infty U_0^2$. Non-dimensional quantities will be denoted with the "+" superscript. Reynolds number is calculated using:

$$Re = \frac{\rho_\infty l_0 U_j}{\mu} \tag{4.1}$$

Where μ is the dynamic viscosity, which is taken to be $1.846 \times 10^{-5} \frac{kg}{m-s}$. The parameters for non-dimensionalization are summarized in Table 4.1, which are based on experiments from Mora et al. (2016).

Table 4.1

Non-Dimensionalization Parameters for Mach 1.5 Planar Jet

Parameter	**Symbol**	**Value [unit]**
Reynolds Number	R_e	155,000
Length Scale	$l_0 = \frac{H}{2}$	0.0052 [m]
Velocity Scale	U_j	449.16 [m/s]
Temperature Scale	$T_\infty = ambient\ Temp$	300 [K]
Density Scale	$\rho_\infty = ambient\ density$	1.225 $[kg/m^3]$
Pressure Scale	$\rho_\infty U_0^2$	247,137 [Pa]

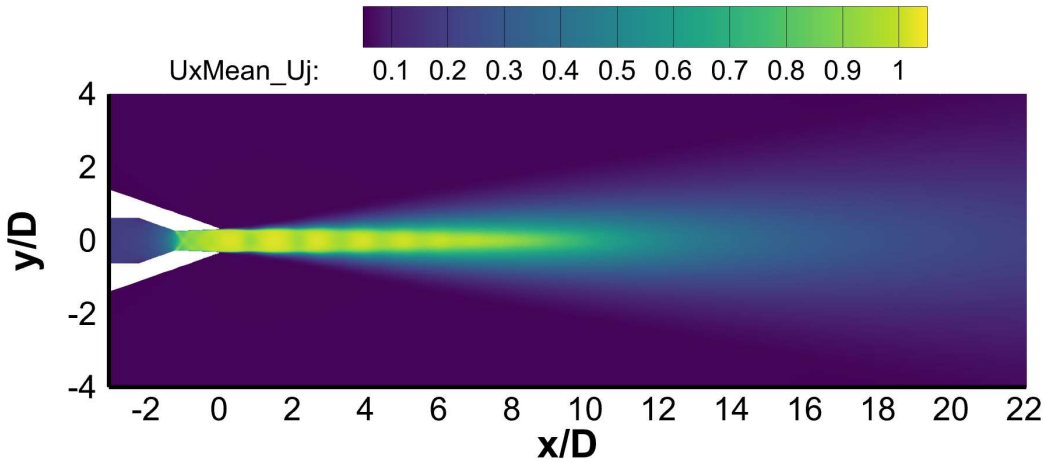

Figure 4.1 Mach 1.5 jet mean velocity contour

We took the mid-line vertical plane of the rectangular jet to present the planar jet that we are considering and focused on the initial shear layers before they merge (see Figure 4.2). It is then assumed that the planar jet profile takes the form of the hyperbolic tangent profile. This is expressed as:

$$u^+(y^+) = \frac{U_j}{2}\left(1 + \tanh\left(\frac{\eta_x}{4\theta^+}\left(\frac{\eta_x}{|y^+|} - \frac{|y^+|}{\eta_x}\right)\right)\right) \tag{4.2}$$

Multiple profiles were created from the data from MS. For each profile, the non-dimensional momentum thickness, θ^+, was computed:

$$\theta^+ = \int_0^\infty \frac{u^+(y^+)}{U_1 - U_2}\left(1 - \frac{u^+(y^+)}{U_1 - U_2}\right) dy^+ \tag{4.3}$$

In Equation 4.3, U_1 is the larger velocity at the axis of symmetry and U_2=0 is the smaller velocity in the far-field, which is zero in this case. Both U_1 and U_2 are made dimensionless using the velocity scale in Table 4.1. As stated before, the y-coordinates were non-dimensionalized by the jet half-height, which is H/2= 0.0052 meters. At the jet exit, the momentum thickness was found to be $\theta^+ = 0.04$. The profiles considered extended to a momentum thickness of $\theta^+ = 0.70$, which corresponds to a streamwise location, x/(H/2), of 24. In the rectangular jet data from MS, this corresponds to a streamwise location, x/D, of 6, where D is the width of the jet. Beyond a momentum thickness of $\theta^+ = 0.70$ the upper and lower shear layers in the jet meet and any linear stability results regarding the symmetric mode would no longer be physical. Additionally, the distance at which the velocity is half that of the velocity at the line of symmetry, η_x, was calculated.

$$\eta_x = y^+|_{u=\frac{U_0}{2}} \tag{4.4}$$

The value of η_x increases along the streamwise direction of the jet and is used when fitting the mean flow profiles to the CFD data. The hyperbolic tangent profile fits the CFD data very well and can be seen in Figure 4.3

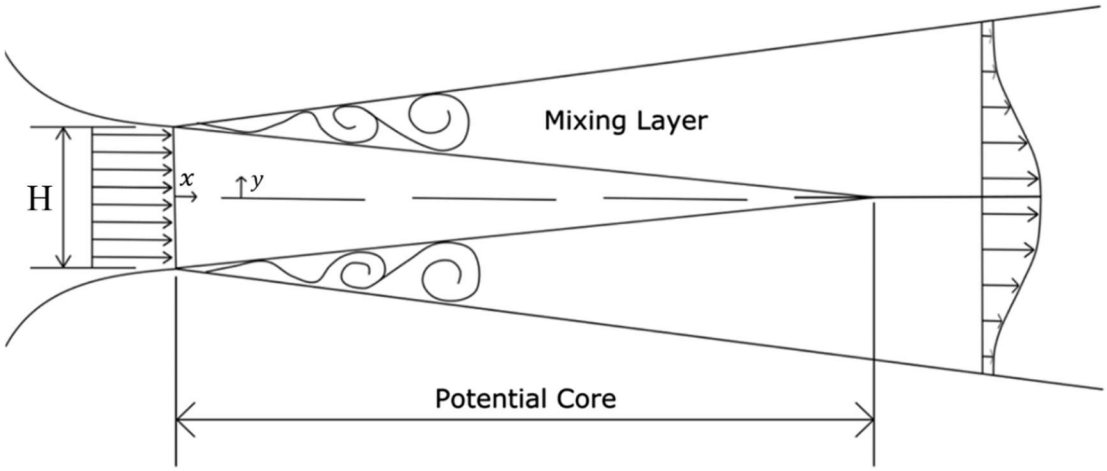

Figure 4.2 Planar jet cross-sectional view

.

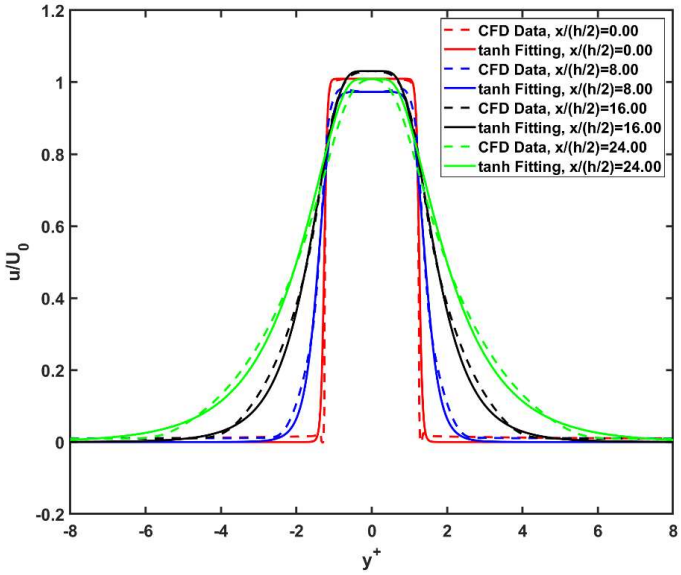

Figure 4.3 Hyperbolic tangent U-velocity fitting to CFD data.

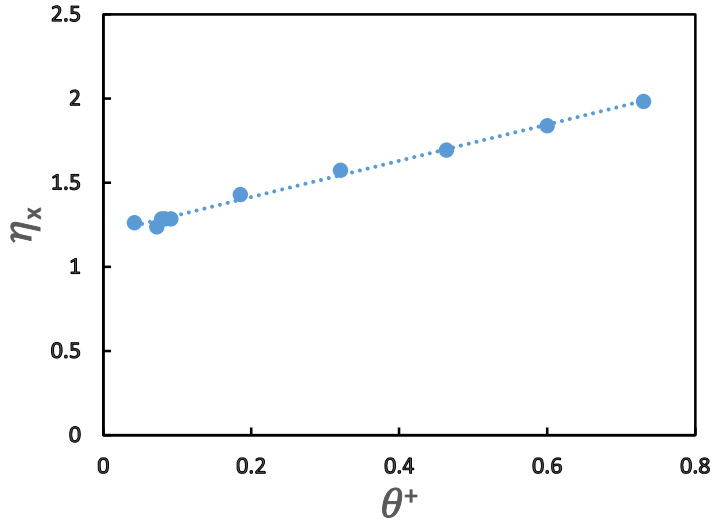

Figure 4.4 η_x versus momentum thickness for MS jet.

The temperature profile was then computed using Crocco's Formulation, which relates the temperature to the velocity. It can be written as:

$$T(u^+) = \frac{-\frac{1}{2}(u^+)^2 + c_1 u^+ + c_2}{c_p} \tag{4.5}$$

The constants, c_1 and c_2, can be found by implementing the boundary conditions. These are that at $u^+ = U_1$, $T = T_1$, and that at $u^+ = U_2$, $T = T_2$. U_1 is taken to be U_j and U_2 is taken to be zero in this case. Likewise with temperature, T_1 is taken to be the larger temperature at the symmetry line and T_2 to be the smaller at the ambient, which is 2.075 and 1 respectively. Inserting the boundary conditions into Equation 4.5, we find the constants to be:

$$c_1 = \frac{c_p(T_1 - T_2) + \frac{1}{2}\left(U_j^2\right)}{U_j} \tag{4.6}$$

$$c_2 = c_p T_1 + \frac{1}{2}U_j^2 - U_j \frac{c_p(T_1 - T_2) + \frac{1}{2}(U_j^2)}{U_j} \tag{4.7}$$

Crocco's formulation agreed well with the CFD data (Mankbadi & Salehian, 2021), though it can also be seen that there are some irregularities in the CFD data in Figure 4.5, especially further downstream. The plot can be seen below.

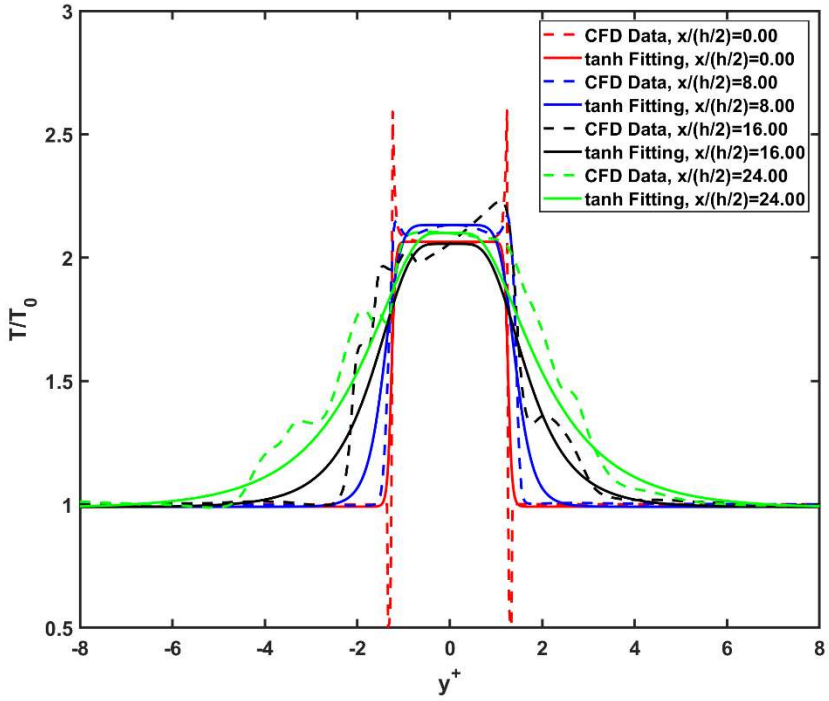

Figure 4.5 Temperature profile fitting to CFD data

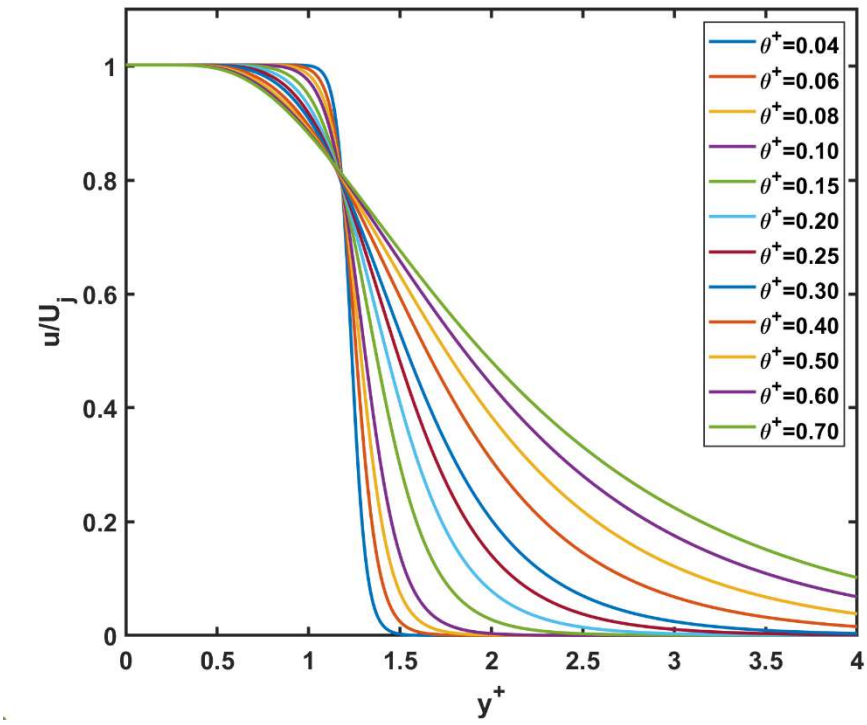

Figure 4.6 Mean flow velocity profiles at various momentum thickness

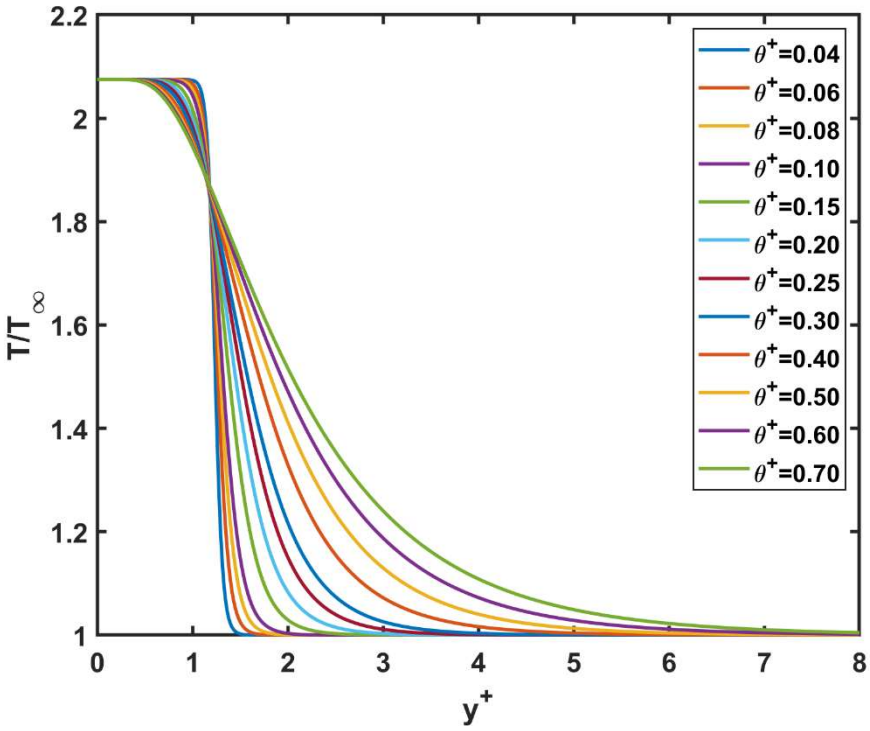

Figure 4.7 Temperature profiles at various momentum thickness

The velocity and temp profiles used in our computations are given in Figures 4.6 and 4.7. To compute the density profile, the ideal gas law was used.

$$\rho = \frac{p}{RT} \tag{4.8}$$

The profile for pressure is constant across the jet for a perfectly expanded jet. Working out units from Equation 4.8, the specific gas constant, R, is non-dimensionalized by U_j^2/T_∞. This gives a value of $R^+ = 0.427$.

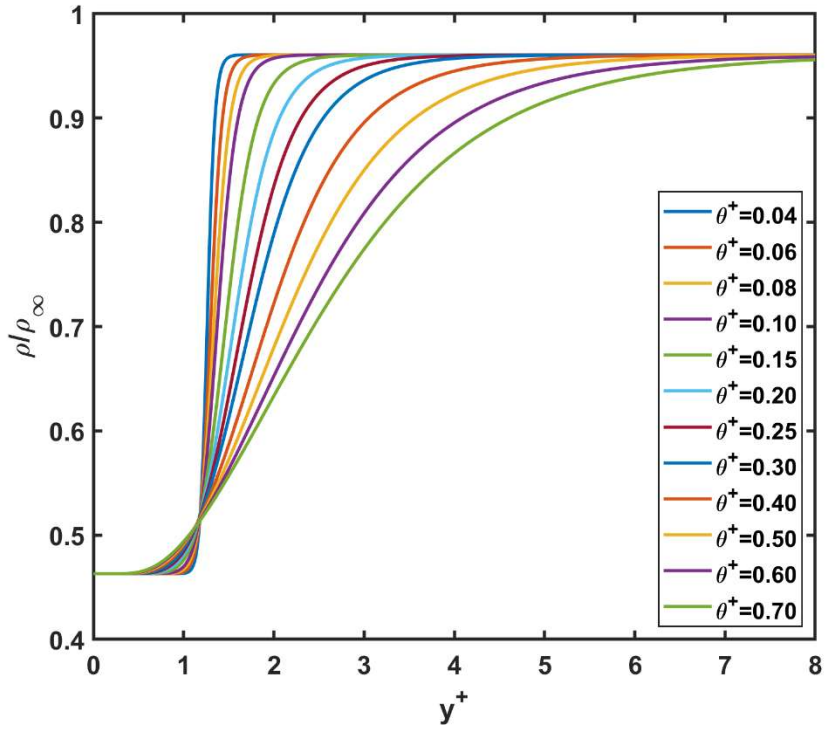

Figure 4.8 Density profiles at various momentum thickness

4.2. Shape Assumptions for the Coherent Structure, Linear Stability Solution

As pointed out earlier, the transversal shape of the coherent structure is given by the locally-parallel linear stability theory. For this purpose, we will be using the NASA

Langley LASTRAC (Chang, 2004). A description of the code can be found in Appendix A.

The code requires the mean flow to be given, which we obtained from our fitted hyperbolic profiles in Figures 4.3 and 4.5, mean flow profiles were created for LASTRAC at various momentum thicknesses. A non-dimensional maximum and minimum U-velocity of 1 and 0 respectively was used. At Mach 1.5 and a total temperature ratio of 3, the resultant static temperature ratio is 2.075. Thus, T_1 was taken to be 2.075, and T_2 was taken to be 1.000. The profiles given to LASTRAC can be seen in Figures 4.7-4.9. Of note, the mean flow velocities, V-velocity, and W-velocity, were taken to be zero across the profiles. The mean flow files include a Reynolds number, length scale, velocity scale, temperature scale, and density scale. These are the parameters by which the mean flow profile is non-dimensionalized.

In the initial region of the jet, the upper and lower shear layers have not merged yet. A 2D planar jet has a symmetric and an asymmetric mode. Only the symmetric mode is being considered here, hence we only used the half-profiles.

Given the mean flow at each streamwise location, LASTRAC returns α_r, α_i, and C_r at various frequencies. These frequencies are converted to Strouhal number. The values for the length and velocity scales used to calculate Strouhal number are the same values from Table 4.1.

$$St = \frac{f l_0}{U_j} \tag{4.8}$$

Here, f is a dimensional frequency given in units of Hz. LASTRAC uses various physical boundaries when running its analysis. At the jet axis of symmetry ($y^+ = 0$), the

v-velocity eigenfunction is zero, and the $\frac{\partial}{\partial y^+}$ derivatives for the other flow parameters are zero. Far away from the jet ($y^+ = \infty$), the eigenfunctions go to zero.

4.2.1 Solution Versus Strouhal Number

The output from LASTRAC provides the variables α_r, α_i, and C_r as functions of Strouhal number. These results can be used to determine the Strouhal numbers that are amplified over a large range of momentum thicknesses.

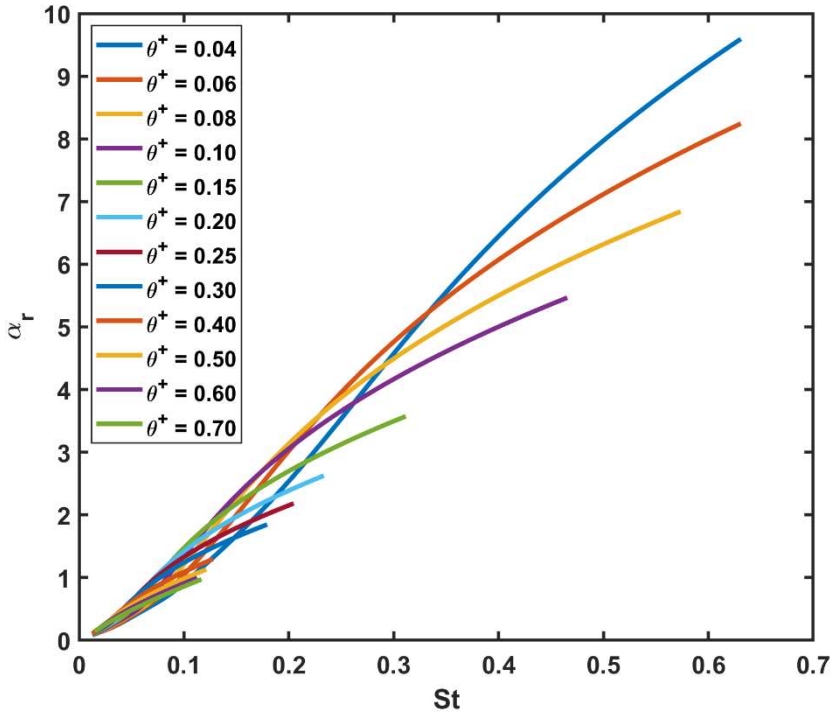

Figure 4.9 α_r versus Strouhal number at various momentum thickness.

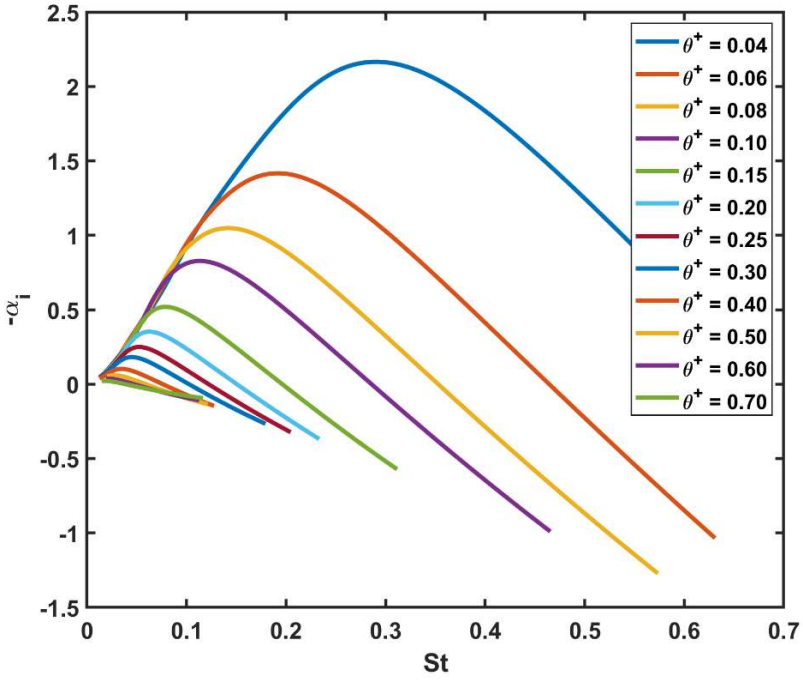

Figure 4.10 Growth rate versus Strouhal number at various momentum thickness.

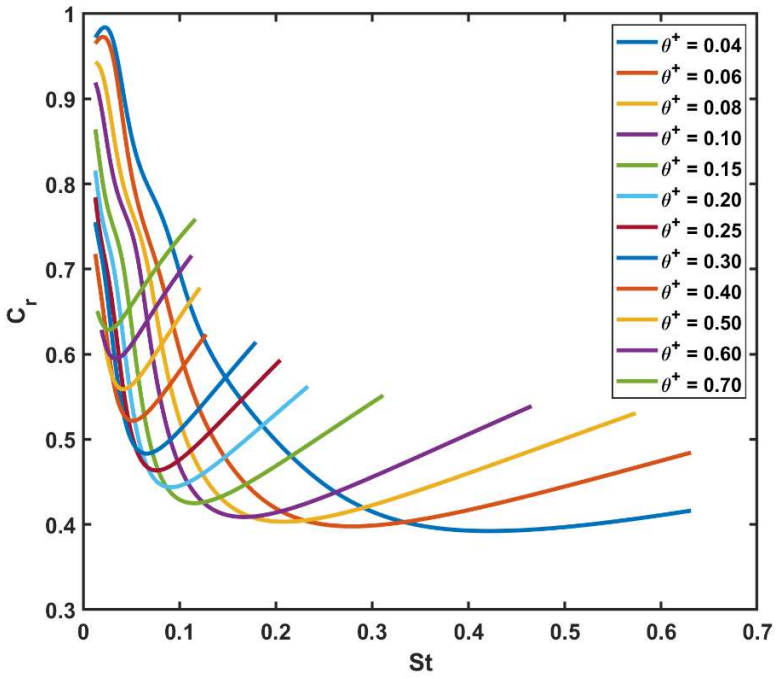

Figure 4.11 Phase speed velocity versus Strouhal number at various momentum thickness.

4.2.2. Solution for Selected Strouhal Numbers Versus Momentum Thickness

Of note, the maximum value of $-\alpha_i$ decreases with an increase in momentum thickness, which is expected. From the set of plots above, Strouhal numbers of 0.025, 0.05, 0.10, 0.20, and 0.40 were selected for further analysis. At these Strouhal numbers, α_r, $-\alpha_i$, and C_r were plotted versus the momentum thickness.

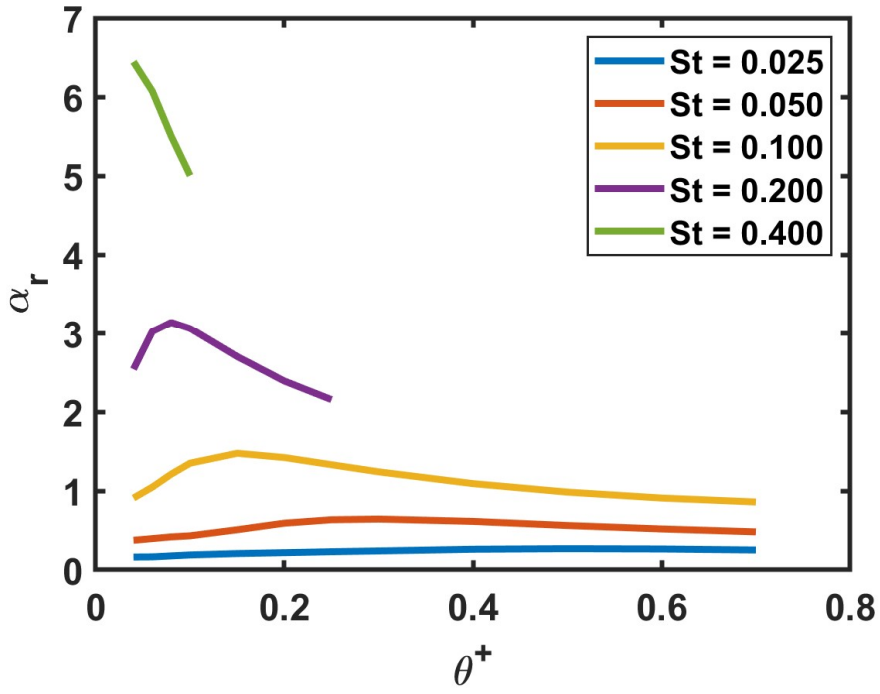

Figure 4.12 α_r versus momentum thickness at various Strouhal numbers

The linear growth rate was calculated using the data from Figure 4.13.

$$N = -2\int_{\theta_0^+}^{\theta^+} \alpha_i(\theta^+)\, d\theta^+ \tag{4.9}$$

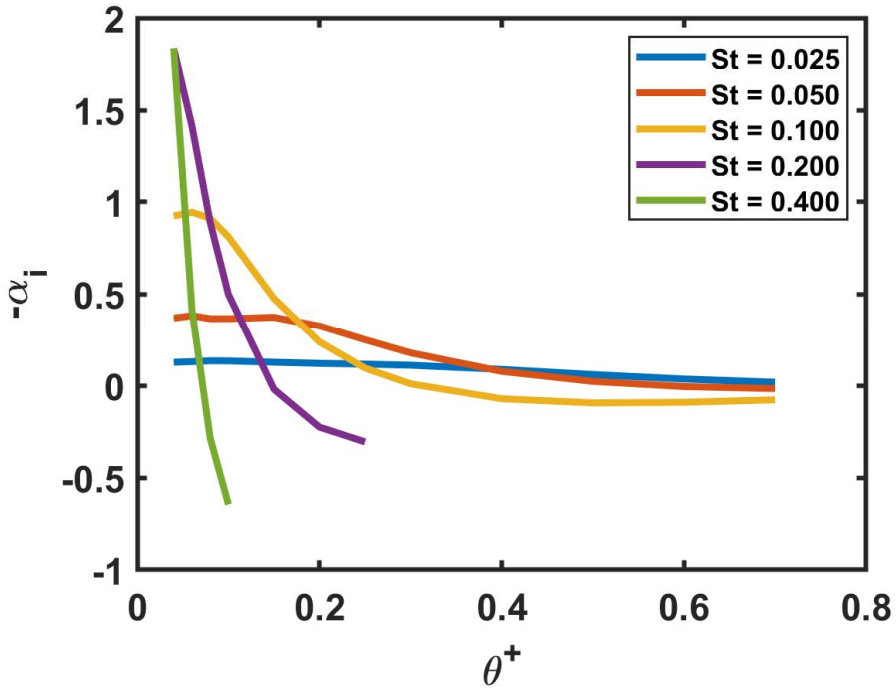

Figure 4.13 $-\alpha_i$ versus momentum thickness at various Strouhal numbers.

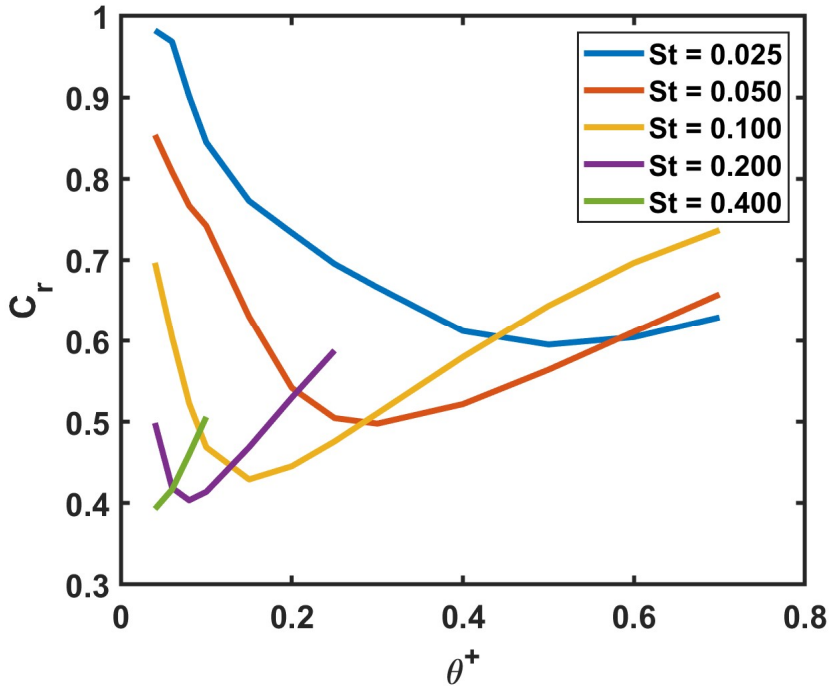

Figure 4.14 Phase speed velocity versus momentum thickness at various Strouhal numbers.

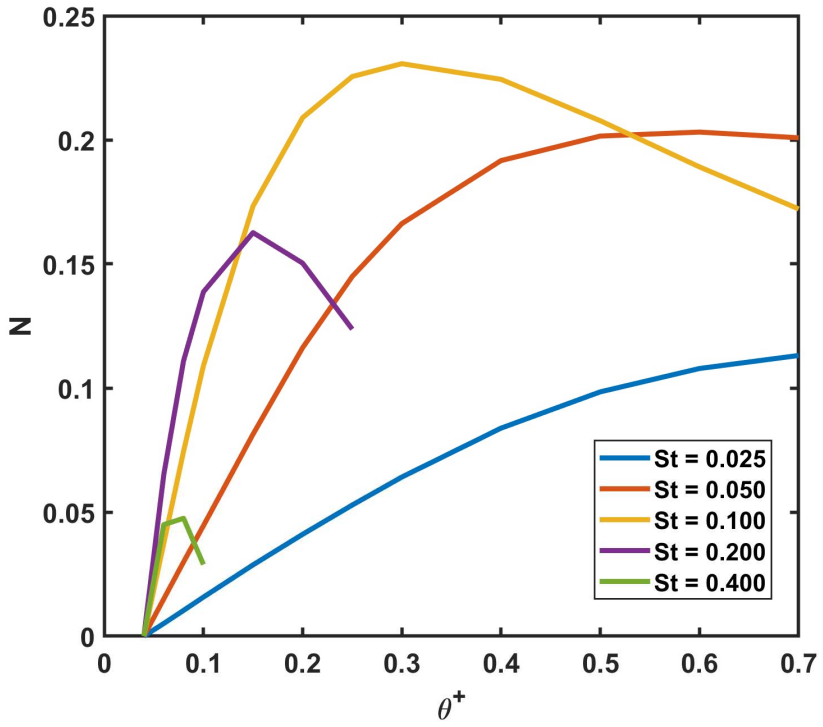

Figure 4.15 N-factor versus momentum thickness at various Strouhal numbers.

In Figure 4.15, it is shown that the linear growth rate is highest for Strouhal numbers 0.10, and 0.05. For the Strouhal numbers 0.20 and 0.40, the growth rate begins to damp at a low range of momentum thickness. The case for Strouhal number of 0.025 has amplification over the range of momentum thicknesses considered, but at a lower magnitude than for Strouhal numbers 0.10 and 0.05. Thus, the chosen Strouhal numbers to be considered for the fundamental-subharmonic and fundamental-harmonic interactions later are 0.05, 0.10 and 0.20.

At each frequency, LASTRAC also outputs eigenfunctions for temperature, pressure, and the u, v, and w velocities. Both real and imaginary components are computed. For the computation of the integrals, the eigenfunctions need to be normalized such that:

$$1 = \int_0^{\infty} (\hat{u}^2 + \hat{v}^2)\, dy \tag{4.10}$$

This integral is first calculated with the non-normalized eigenfunctions to obtain a normalization coefficient, k. This normalization coefficient is applied to the real and imaginary components of the velocity eigenfunctions. The velocity eigenfunctions are simply normalized as:

$$\hat{u}_{r,norm} = \frac{\hat{u}_r}{k} \tag{4.11}$$

$$\hat{u}_{i,norm} = \frac{\hat{u}_i}{k} \tag{4.12}$$

$$\hat{v}_{r,norm} = \frac{\hat{v}_r}{k} \tag{4.13}$$

$$\hat{v}_{i,norm} = \frac{\hat{v}_i}{k} \tag{4.14}$$

Some examples of the normalized eigenfunction outputs can be seen below. It should be noted that only the symmetric mode is considered and the eigenfunctions go from $y^+ = 0$ to $y^+ = +\infty$.

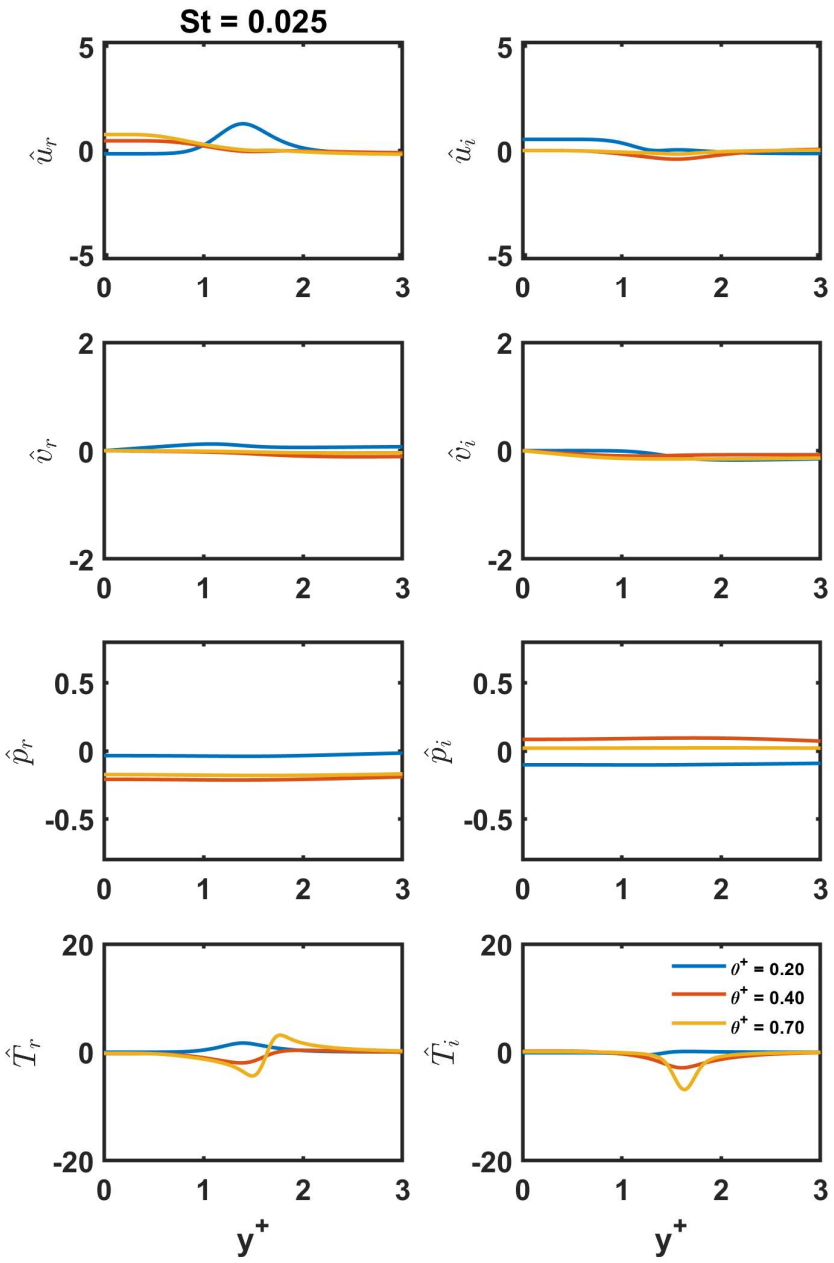

Figure 4.16 Eigenfunctions at St=0.025

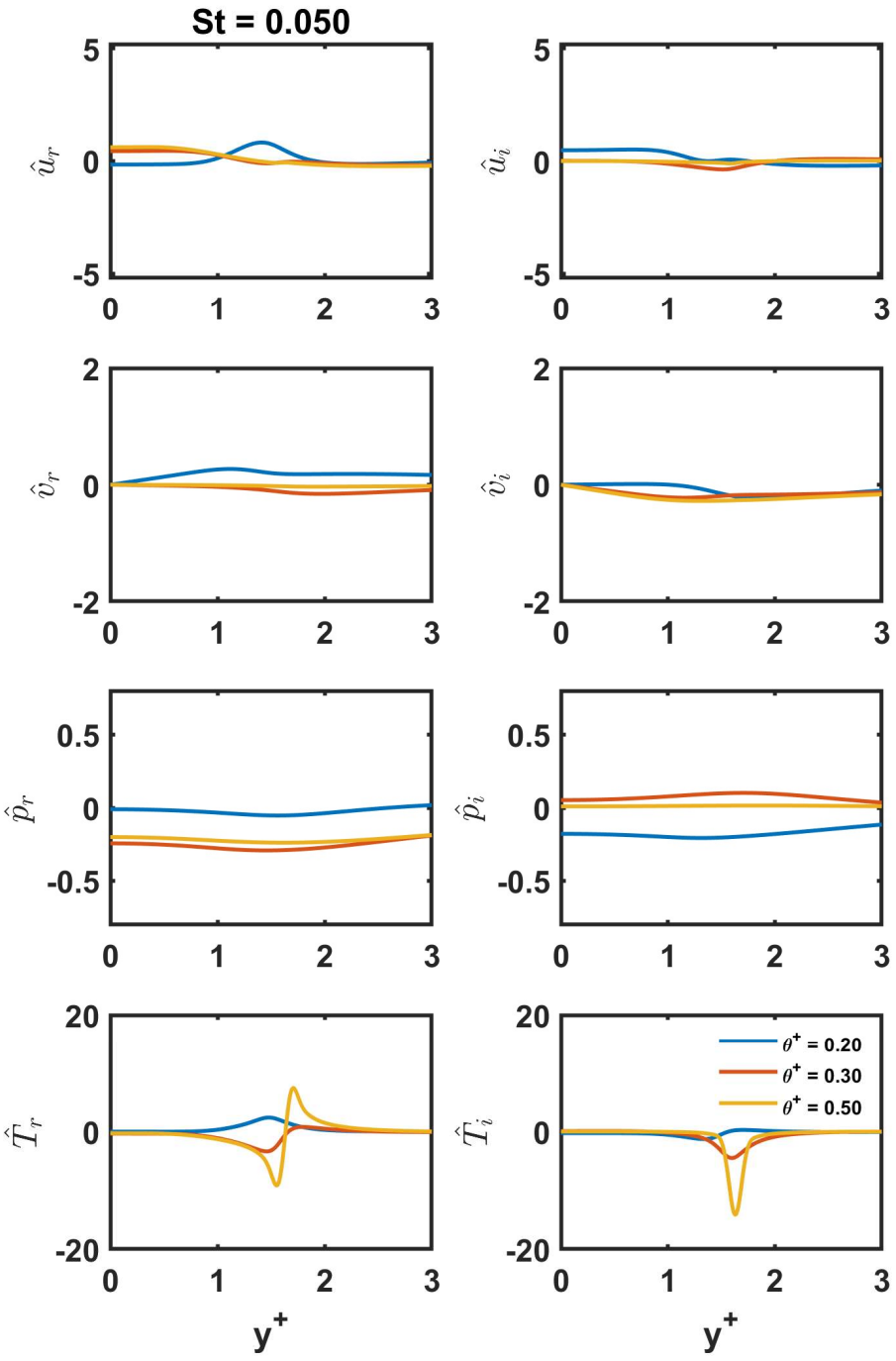

Figure 4.17 Eigenfunctions at St=0.050

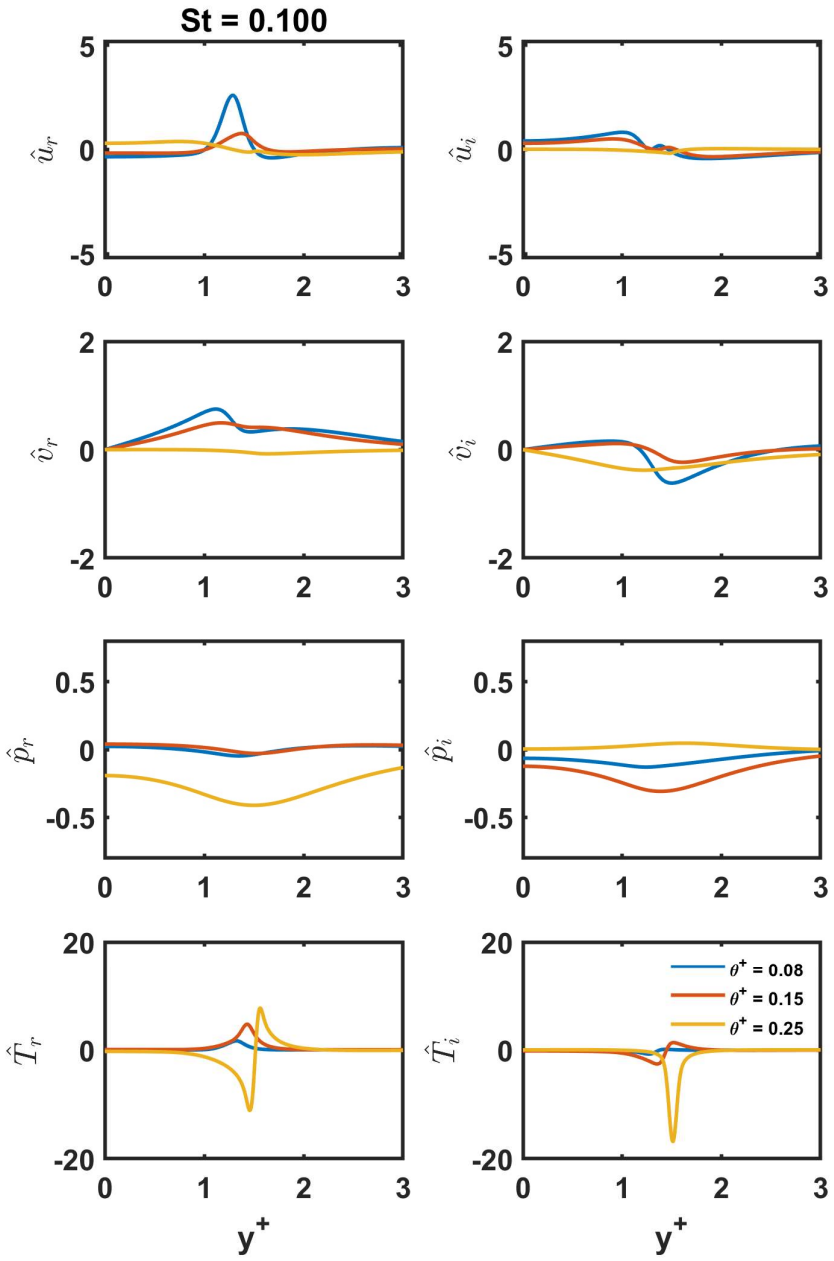

Figure 4.18 Eigenfunctions at St=0.100

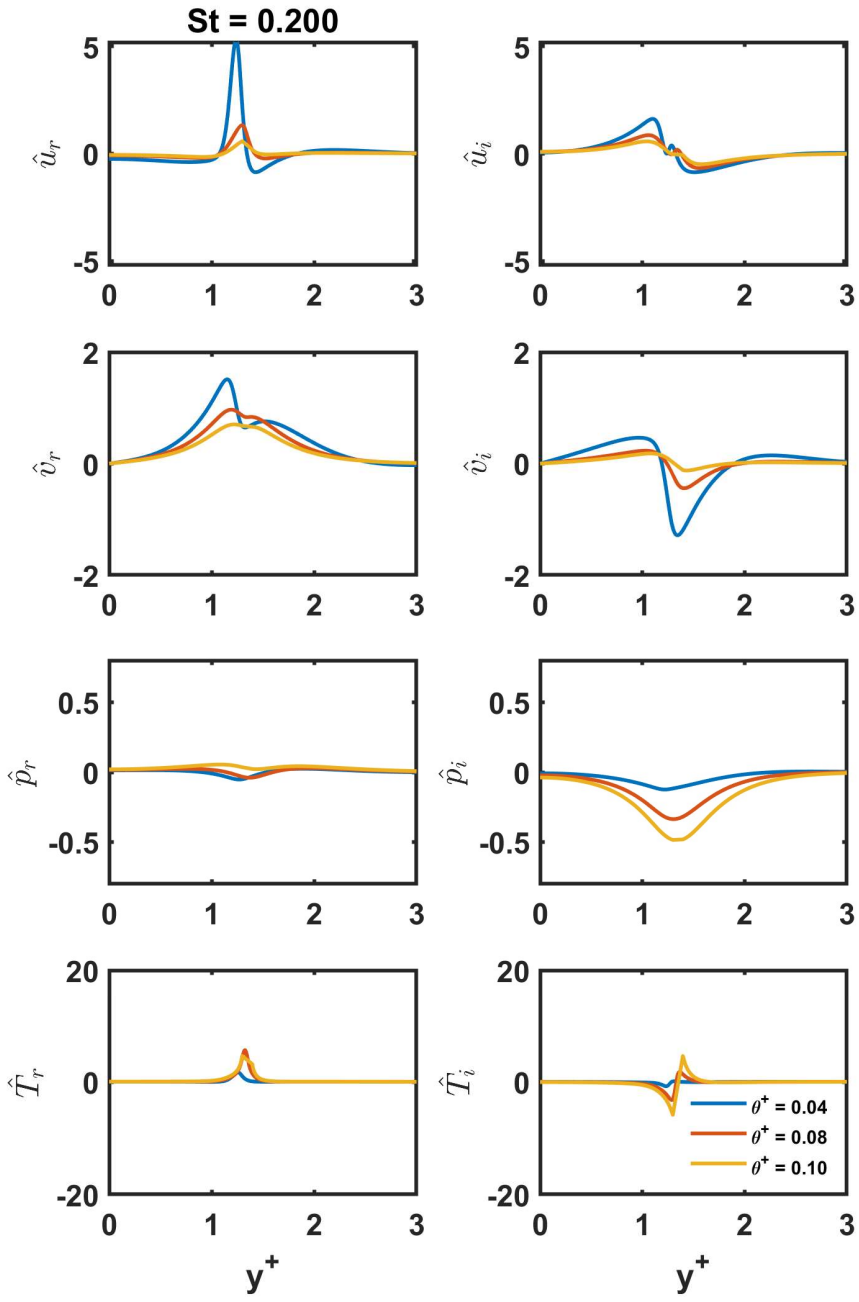

Figure 4.19 Eigenfunctions at St=0.200

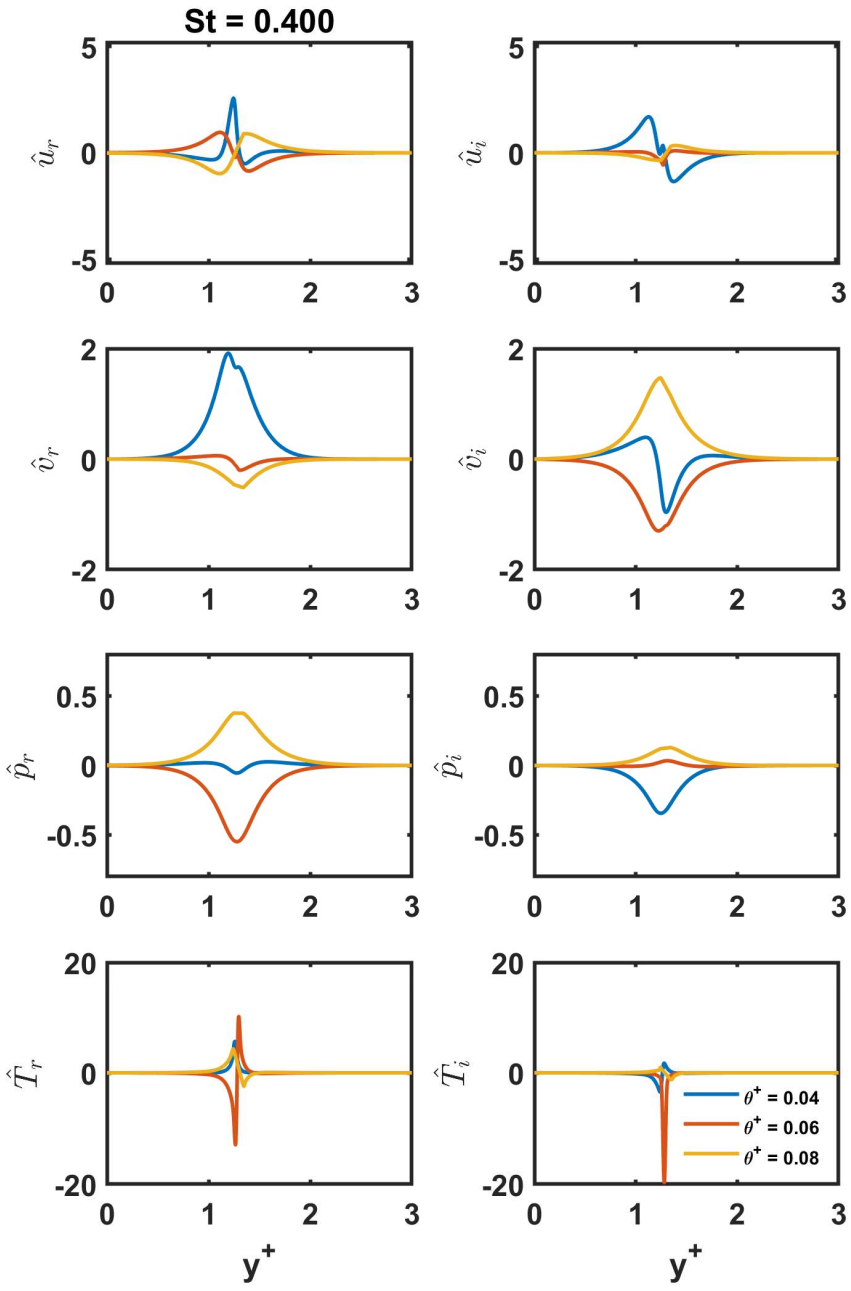

Figure 4.20 Eigenfunctions at St=0.400

4.3. Calculation of the Integrals

In Chapter 3, we derived a set of ODE's with various shape assumptions. These shape assumptions take the form of several integrals. These integrals can be functions of the mean flow as well as the eigenfunctions described in Section 4.2. The integrals are computed numerically using MATLAB. The eigenfunctions are for the half-profile of the jet. Likewise, the integrals are calculated for the half-width of the jet and not the full profile, that is, from the line of symmetry to the far-field. Before the integrals can be calculated, the eigenfunctions are normalized as described in Equations 4.10-4.14. The magnitudes of the eigenfunctions then become as follows:

$$|\hat{u}| = \sqrt{\hat{u}_{r,norm}^2 + \hat{u}_{i,norm}} \tag{4.15}$$

$$|\hat{v}| = \sqrt{\hat{v}_{r,norm}^2 + \hat{v}_{i,norm}} \tag{4.16}$$

Below are the integrals that are functions of the mean flow only:

$$I_{am} = \frac{1}{2}\int_0^\infty \rho \bar{U}^3 \, dy \tag{4.17}$$

$$I_{md} = \int_0^\infty \bar{U}_y^2 \, dy \tag{4.18}$$

Next are the integrals that depend on the eigenfunctions.

$$I_{mf} = -\int_0^\infty (\hat{v}\hat{u}^* + CC)_f \, \bar{\rho} \, \frac{\partial \bar{U}}{\partial y} \, dy \tag{4.19}$$

$$I_{af} = \int_0^\infty (|\hat{u}|^2 + |\hat{v}|^2 + |\hat{w}|^2)_f \bar{\rho}\bar{U} \;\; dy \tag{4.20}$$

$$I_{fd} = 2\int_0^\infty \left[(|\alpha|^2 + n^2) \;\; (|\hat{u}|^2 + |\hat{v}|^2 + |\hat{w}|^2) + \left(\left|\frac{\partial \hat{u}}{\partial y}\right|^2 + \left|\frac{\partial \hat{v}}{\partial y}\right|^2 + \left|\frac{\partial \hat{w}}{\partial y}\right|^2 \right) \right]_f dy \tag{4.21}$$

For I_{fd}, n and $\hat{w}$ are taken to be zero since we are considering the 2D eigenfunctions only, and α is the magnitude of the complex wave number. The above integrals are computed for each momentum thickness considered, yielding values for the integrals versus momentum thickness. The integrals are then curve fit versus momentum thickness in excel for evaluating the solution to the ODE.

4.3.1. Integrals that are Functions of the Mean Flow

The integrals, I_{am} and I_{md}, are only a function of the mean flow shape and are shown in Figures 4.21 and 4.22 in comparison with (Dahl & Mankbadi, 2002; Dahl et al., 2003) results, but we note that their results are for a round jet, while here we are considering a 2D shear layer.

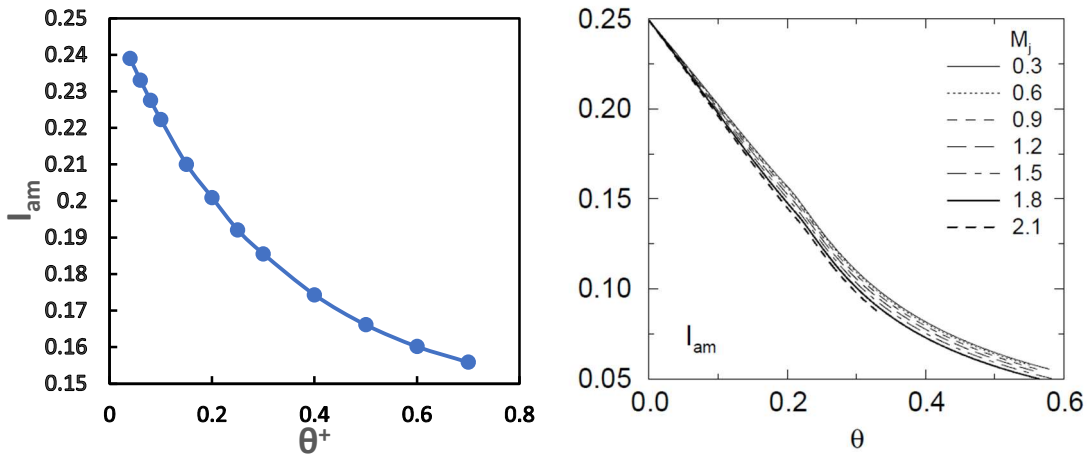

Figure 4.21 I_{am} versus momentum thickness: current results (left), and results from Dahl and Mankbadi (2002) (right).

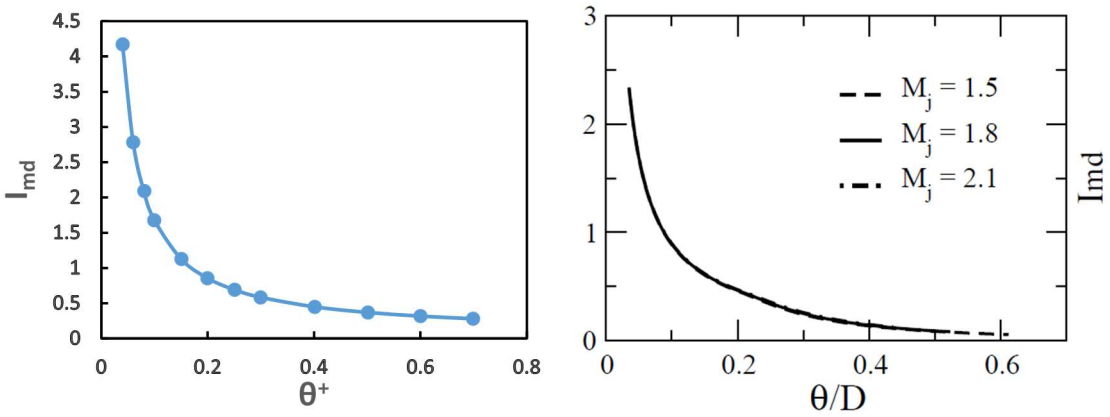

Figure 4.22 I_{md} versus momentum thickness: current results (left), results from Dahl et al. (2003) (right).

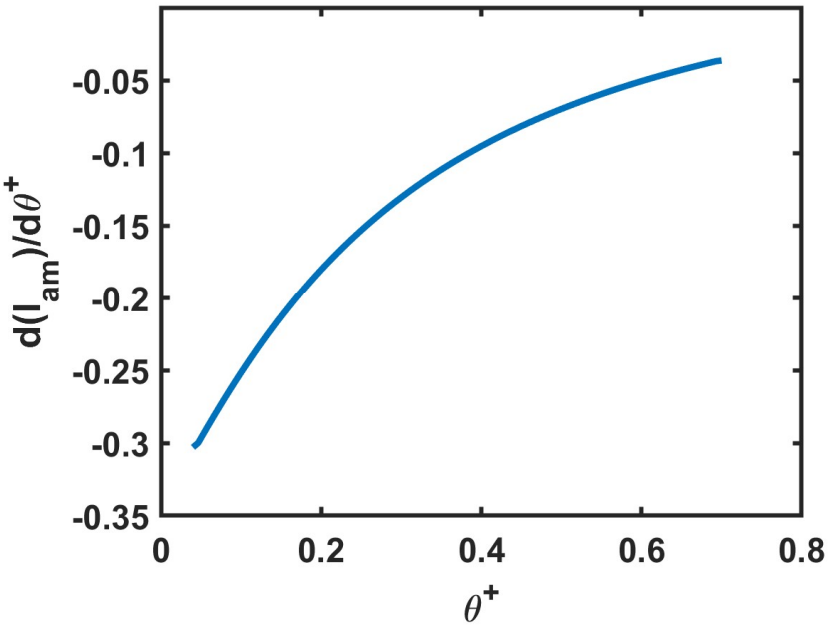

Figure 4.23 $\frac{d(I_{am})}{d\theta^+}$ versus momentum thickness

4.3.2. Integrals that are Functions of Strouhal Number

The integrals, I_{af}, I_{fd}, and I_{mf}, are functions of both the mean flow and the eigenfunction. Thus, they are also functions of Strouhal number.

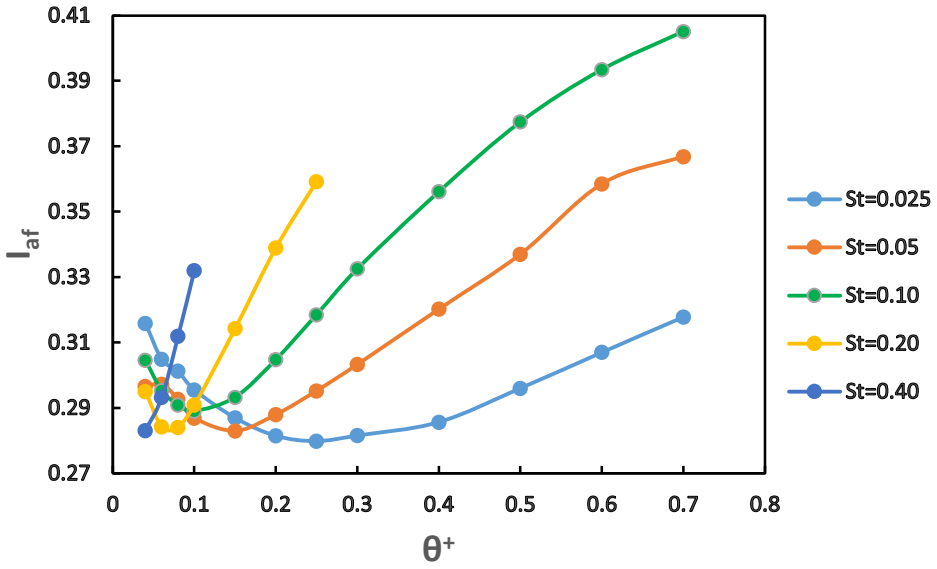

Figure 4.24 I_{af} versus momentum thickness

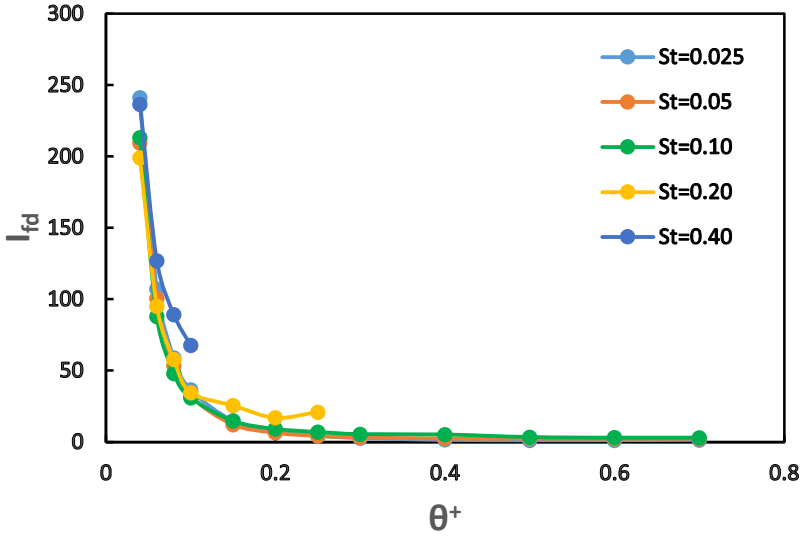

Figure 4.25 I_{fd} versus momentum thickness

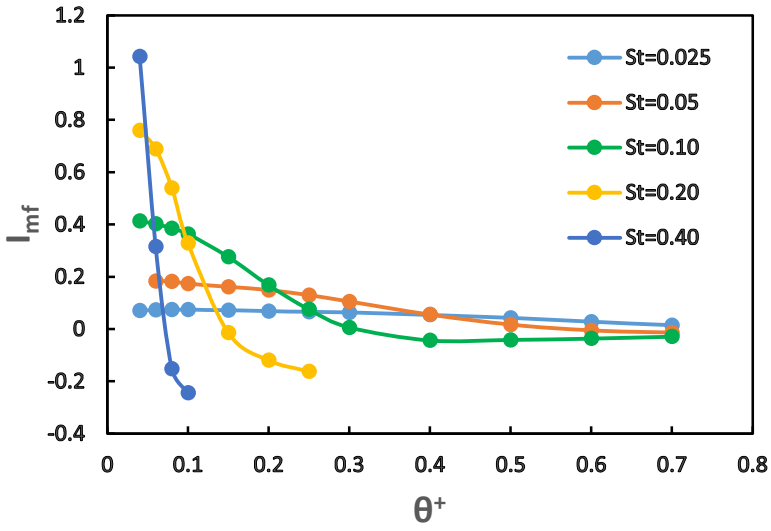

Figure 4.26 I_{mf} versus momentum thickness

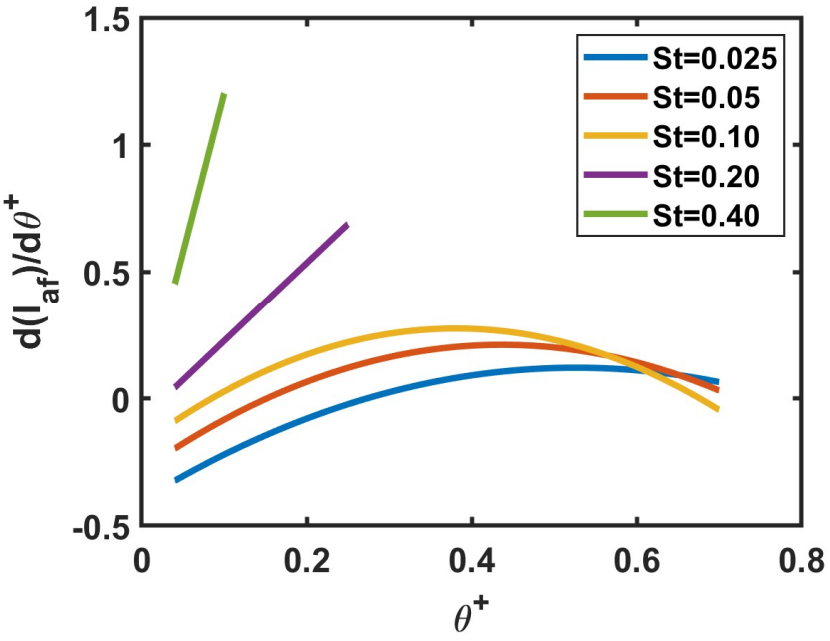

Figure 4.27 $\frac{d(I_{af})}{d\theta^+}$ versus momentum thickness

4.3.3. The Wave-Wave Interaction Integrals

Up until now, we have considered the integral terms that are defined by the mean flow and eigenfunctions of a single Strouhal number. When considering the solution

without interaction, these results are sufficient. However, when solving the set of ODE's with interaction, an additional integral term is needed, I_{ww}. This integral represents the interaction between the two modes being considered. For this work, we are considering the fundamental Strouhal number 0.10, with subharmonic St=0.05, and harmonic St=0.20. This gives the fundamental-subharmonic pair St=0.10, 0.05, and fundamental-harmonic pair St=0.10, 0.20.

$$I_{ww} = -\,2\,\left|I_{fs}\right|\,\cos\{\phi + \beta\} \tag{4.21}$$

Above, ϕ is the phase angle of the complex integral quantity, I_{fs}, and β is the phase between the two modes being considered. I_{fs} is defined as:

$$I_{fs} = \int_0^{\infty} \left\{ \hat{u}_s^* \hat{u}_s^* \frac{\partial \hat{u}_f}{\partial x} + \hat{u}_s^* \hat{v}_s^* \left(\frac{\partial \hat{u}_f}{\partial y} + \frac{\partial \hat{v}_f}{\partial x} \right) + \hat{v}_s^* \hat{v}_s^* \frac{\partial \hat{v}_f}{\partial y} \right\} dy^+ \tag{4.22}$$

Above, the subscript *"s"* indicates parameters at the lower Strouhal number, and *"f"* at the higher for a given pair.

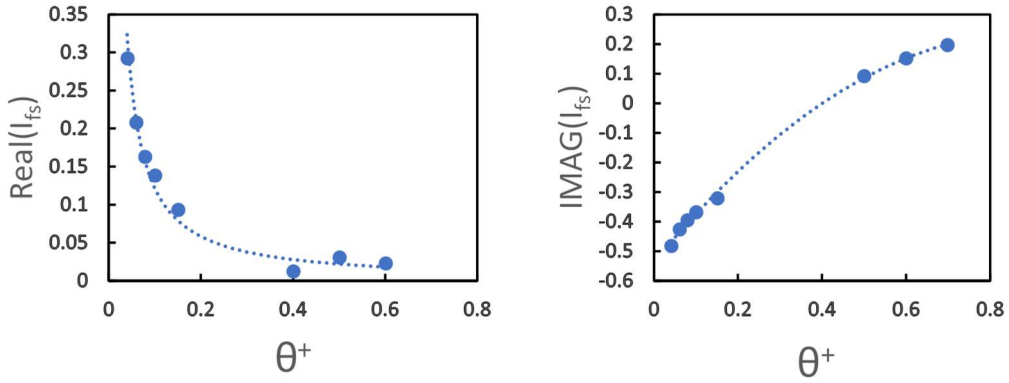

Figure 4.28 Real and Imaginary components for I_{fs} with St=0.10, 0.05

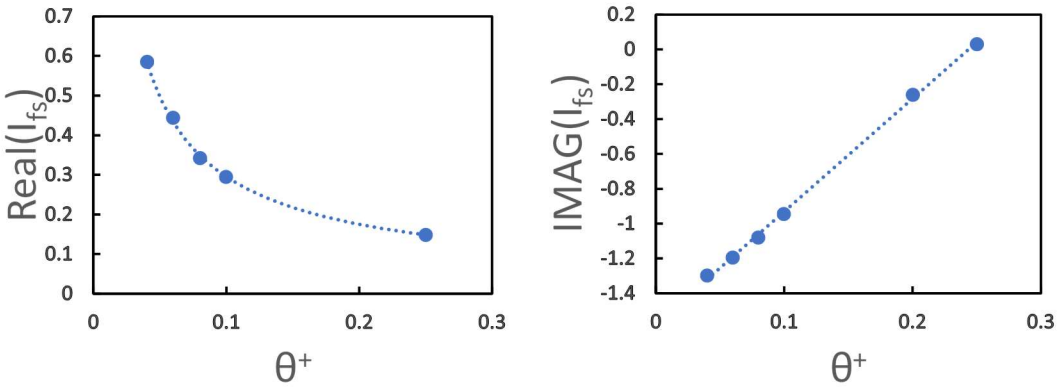

Figure 4.29 Real and imaginary components for I_{fs} with St=0.10, 0.20

5. Solution of the Amplitude Equations Without Wave-Wave Interaction

Without considering the wave-wave interaction, the system of ODE's given in Chapter 3 (Equations 3.63-3.64) reduces to:

$$\frac{d\theta}{dx}\frac{dI_{am}}{d\theta} = -|A|^2\, I_{mf} - \frac{1}{Re} I_{md} \tag{5.1}$$

$$\frac{d\left(I_{af}|A|^2\right)}{dx} = |A|^2 \left(I_{mf} - \frac{1}{Re}\, I_{fd}\right) \tag{5.2}$$

In Equations 5.1 and 5.2, it is seen that the viscous effects are dependent upon the Reynolds number considered. We consider here a variable effective Reynolds number that is taken as a function of the momentum thickness, as was previously described in Chapter 3. Cases will be run solving Equations 5.1 and 5.2 at the different Strouhal numbers considered and various initial amplitudes. Each case will be run for A_0^2 of 10^{-3}, 10^{-4}, 10^{-5}, 10^{-6}, and 10^{-8}. The linear solution is that where $A_0^2 = 10^{-8}$.

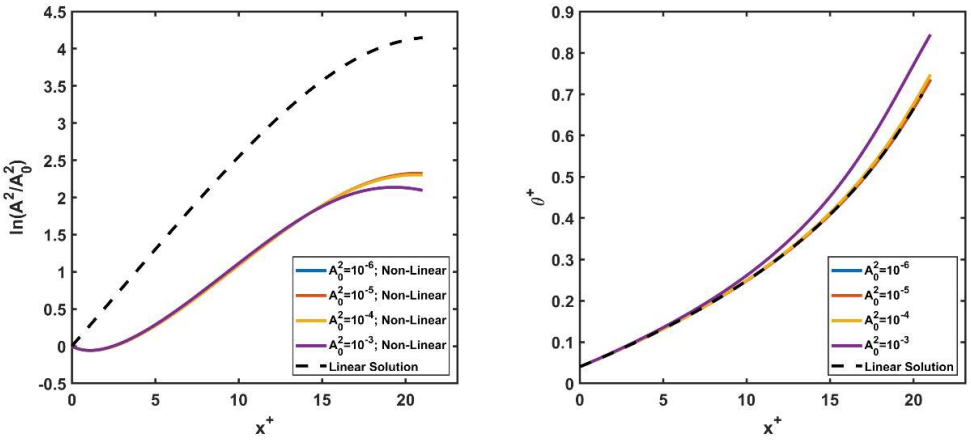

Figure 5.1 ODE solution for St=0.025

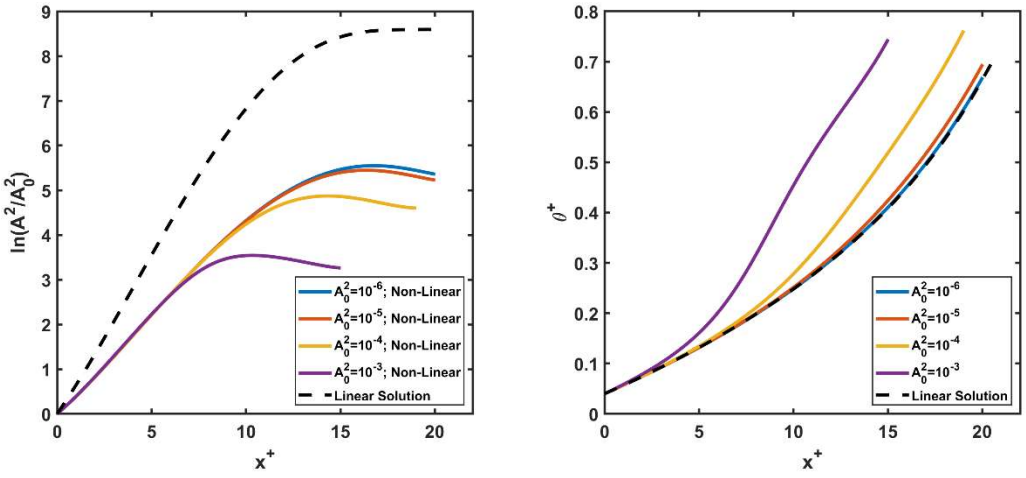

Figure 5.2 ODE solution for St=0.05

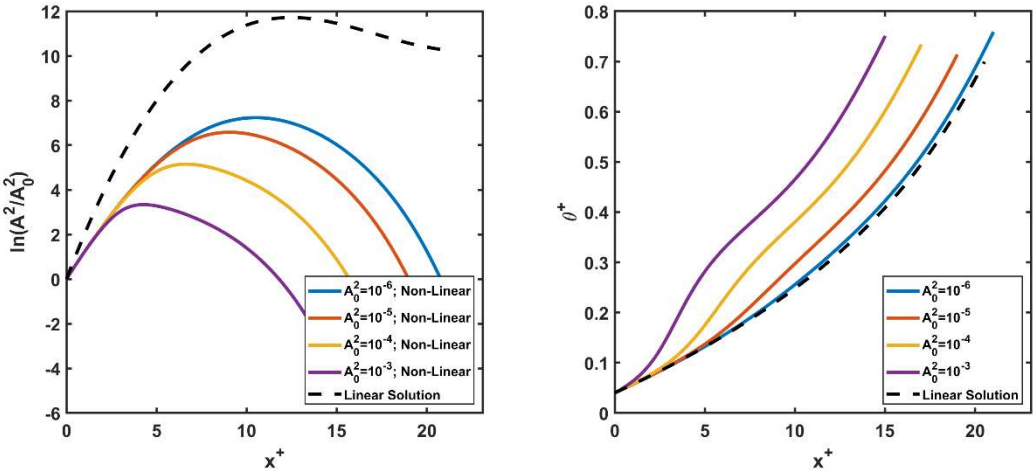

Figure 5.3 ODE solution for St=0.10

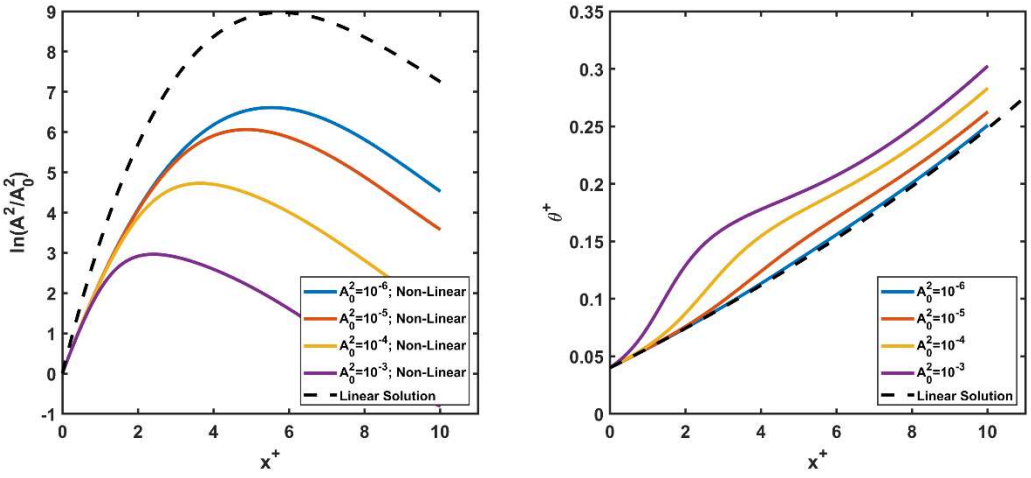

Figure 5.4 ODE solution for St=0.20

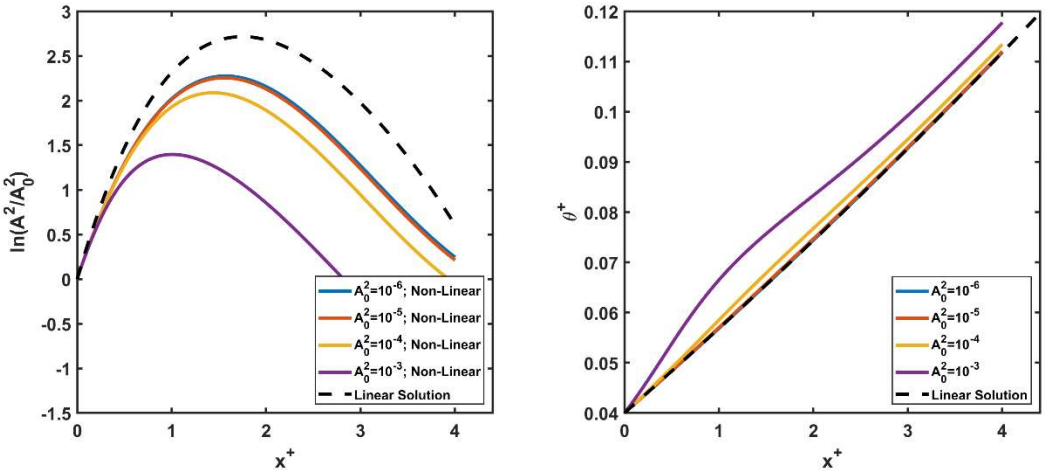

Figure 5.5 ODE solution for St=0.40

It is shown that the growth of the non-linear amplitude decreases as the initial amplitude, A_0^2, increases. This trend agrees with Dahl and Mankbadi (2002) for a supersonic round jet. The addition of excitation resulted in an increase of momentum thickness compared to the solution without excitation, which is also consistent with results from Dahl and Mankbadi (2002). As expected, the increase of momentum

thickness was more amplified as the initial amplitude was increased. The most pronounced increase in the momentum thickness growth occurred for Strouhal numbers 0.05, 0.10, and 0.20. Looking back at the results from linear stability analysis, these Strouhal numbers had the highest N-factor across the range of momentum thicknesses. This result is consistent with the work of Samimy et al. (2018), who's experiments showed a pronounced increase in jet width in this Strouhal number region, though it should be noted that this was for a high subsonic round jet.

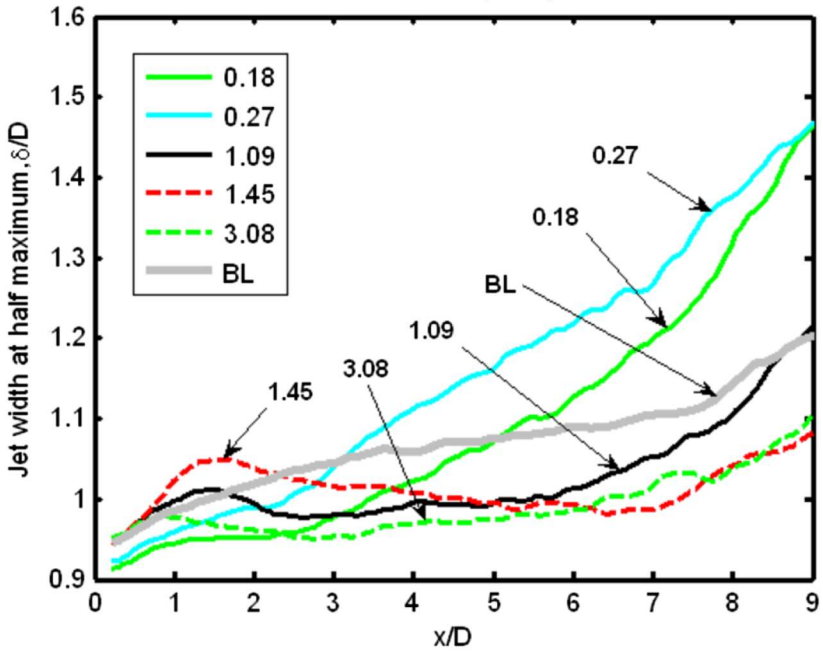

Figure 5.6 Experimental results of jet width for various Strouhal numbers and base-line for Mach 0.9 round jet with $Re_D = 0.62 \times 10^6$ (Samimy et al., 2018).

Another result that can be analyzed is the development of the nonlinear amplitude at various Strouhal numbers. The general trend can be compared with N-factor, as described in Chapter 4. We note that the trend compares very well to the results for N-

factor in Figure 4.15. In both the linear and nonlinear solutions, St =0.1 is most amplified along he streamwise direction.

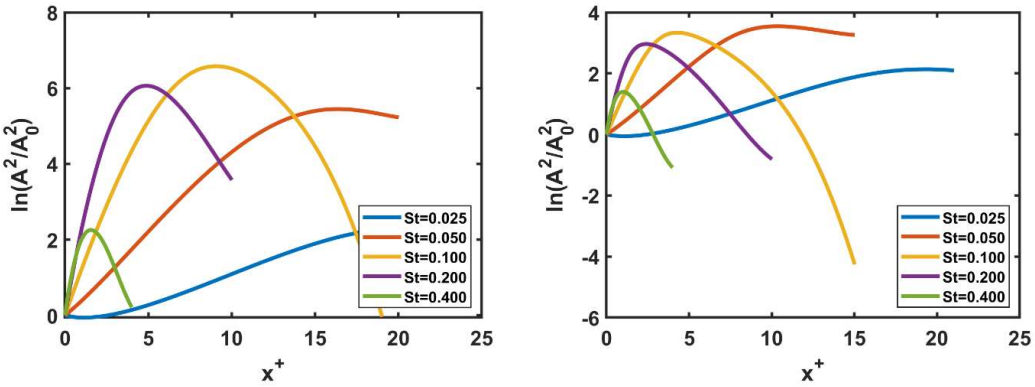

Figure 5.7 Non-linear amplitude at various Strouhal numbers for $A_0^2 = 10^{-5}$ (left) and $A_0^2 = 10^{-3}$ (right).

6. Solution of the Amplitude Equations with Wave-Wave Interaction

When the terms representing the wave-wave interaction are included, the ODE's becomes the full set presented in Chapter 3.

$$\frac{d\theta}{dx}\frac{dI_{am}}{d\theta} = -|A|^2 I_{mf} - |B|^2 I_{ms} - \frac{1}{Re} I_{md} \tag{6.1}$$

$$\frac{d\left(I_{af}|A|^2\right)}{dx} = |A|^2 \left(I_{mf} - \frac{1}{Re} I_{fd}\right) - I_{ww}|A||B|^2 \tag{6.2}$$

$$\frac{d(I_{as}|B|^2)}{dx} = |B|^2 \left(I_{ms} - \frac{1}{Re} I_{sd}\right) + I_{ww}|A||B|^2 \tag{6.3}$$

Here, A^2 corresponds to the amplitude at the larger Strouhal number and B^2 corresponds to that of the smaller. Looking at the opposite signs on the interaction term in Equations 6.2 and 6.3 indicates that the interaction transfers energy from one mode to the other.

As previously indicated, there has been a few attempts for reducing the jet noise via a single-mode excitation (Crawley et al., 2012, 2015; Samimy et al., 2012, 2018). Single-mode excitation has shown some limited successes in some few cases but not in other cases (Crawley et al., 2012). By exciting the jet at a given frequency mode, the hypotheses are that this mode will interact with the naturally present coherent modes in a way to change the frequency content of the noise sources and, hopefully, the far-field noise spectra as well.

We focus here on modifying the noise source via harmonic or subharmonic excitation. In a future work, we will look at the effect of this type of excitation on the radiated noise. In Mankbadi (1991), it was shown that the interaction of various coherent modes among themselves has a non-zero time average only if either of these two conditions applies: A) the two modes are related to each other by harmonic relations, i.e.,

if one mode is at frequency f, the other mode must be f/2, f/4, f/8, … or 2f, 4f, 6f, ...etc. B) The other possible non-zero averaged interactions when 3 modes are interaction with frequencies governed by the sum and difference relation. We focus here on the harmonic or subharmonic interaction as it has shown before to be a significant mechanic in low-Mach number jets.

We define the task here as follows: We are looking at only the shear layer in the initial region of a supersonic rectangular jet before the shear layers of the minor axes have merged. The jet is assumed to be turbulent dominated by coherent structure. The coherent structure is presented here by only the most amplified mode corresponding to the frequency at which the radiated sound spectra peaks. The amplitude of the energy of this peak is labeled as:

$$E_f = |A|^2 \tag{6.4}$$

We will explore reducing $E_f(x)$, via imposing a subharmonic at frequency (f/2) with initial energy amplitude $E_{(f/2),0}$ or by imposing a harmonic frequency (2f) with initial energy amplitude, $E_{2f,0}$. In the study presented below we take the fundamental mode that we are trying to reduce to correspond to St=0.10. For the rectangular jet that we are approximating here that was simulated by Mankbadi and Salehian (2021) and experimentally investigated by Mora et al. (2016), it was found out that frequency where the far field noise spectra peak corresponds to St=0.1. This was also shown to be most amplified in the current analysis as well. Of course, this is only an approximate value, and we also need to keep in mind that we are only approximating the jet by two symmetric shear layers, and we are only considering the symmetric mode.

The interaction process will be a function of several parameters including the Strouhal number pair considered, the initial amplitudes of the imposed waves, $E_{f,0}$, $E_{(f/2),0}$, and $E_{2f,0}$; and the initial phase angle between each of the two modes, β. As a practical guide, we would like the imposed initial level of the controlling mode to be less than that of the fundamental to avoid creating an additional significant noise source.

6.1. Bi-modal Excitation at the Fundamental and Subharmonic Frequency

The first case considered is that of the fundamental and subharmonic at Strouhal numbers 0.10 and 0.05 respectively. Equations 6.1-6.3 were solved for various combinations initial amplitudes. Values for the phase, β, were taken to be $0, \frac{\pi}{2}, \pi$, and $\frac{3\pi}{2}$.

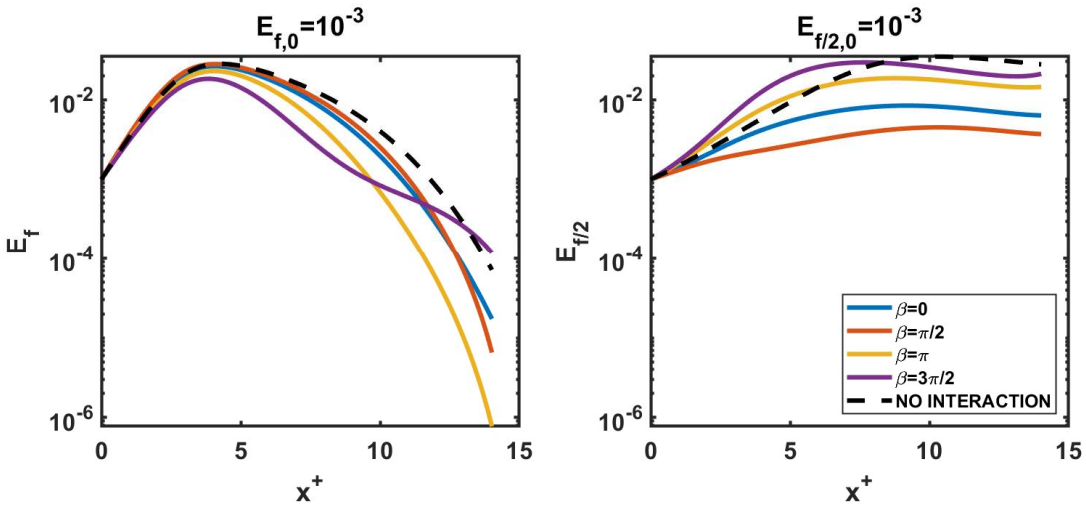

Figure 6.1 Amplitudes for St=0.10, 0.05; $E_{f,0} = 10^{-3}$, $E_{f/2,0} = 10^{-3}$

In this case, with the fundamental frequency being at St=0.1, we excite the jet at subharmonic at St=0.05. Various levels of initial amplitudes were considered, and we noted that the interaction is there, and there is some reduction of the fundamental, but it is relatively weak as shown in Figure 6.1. With both initial amplitudes smaller, while still

equal, the interaction was even less pronounced on the fundamental, which can be seen in Figure 6.3. For cases with smaller initial amplitudes and when $E_{f,0} > E_{f/2,0}$, the effects of interaction were even weaker. We note that the wave-wave interaction term appears with opposite signs in the fundamental and subharmonic equations. Thus, depending on the initial phase difference, it takes energy from one and move it to the other as shown in Figures 6.1 and 6.2.

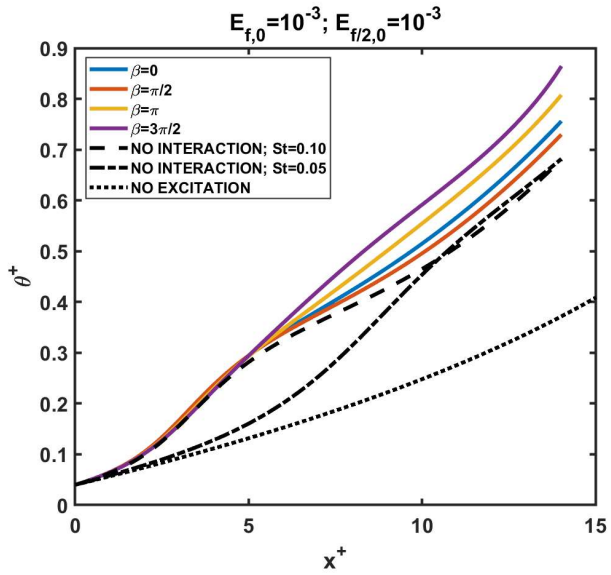

Figure 6.2 Momentum thickness versus streamwise location for St=0.10, 0.05 with $E_{f,0} = 10^{-3}$, $E_{f/2,0} = 10^{-3}$

We examine the development of the corresponding momentum thickness shown in Figure 6.2. We note several levels of the momentum thickness development. The bottom line represents the momentum thickness development if there is no coherent structure at all, meaning the shear layer growth is governed only by the effective viscous and turbulent dissipation term. We also show the development if each of the two modes are added separately without considering the interaction among the two. Then, we show the

momentum thickness when both modes interact for various initial phase difference. We note that the spreading rate is considerably enhanced for the two-mode interaction cases, particularly at $\beta = \frac{3\pi}{2}$. This will reduce the length of the potential core in a real jet.

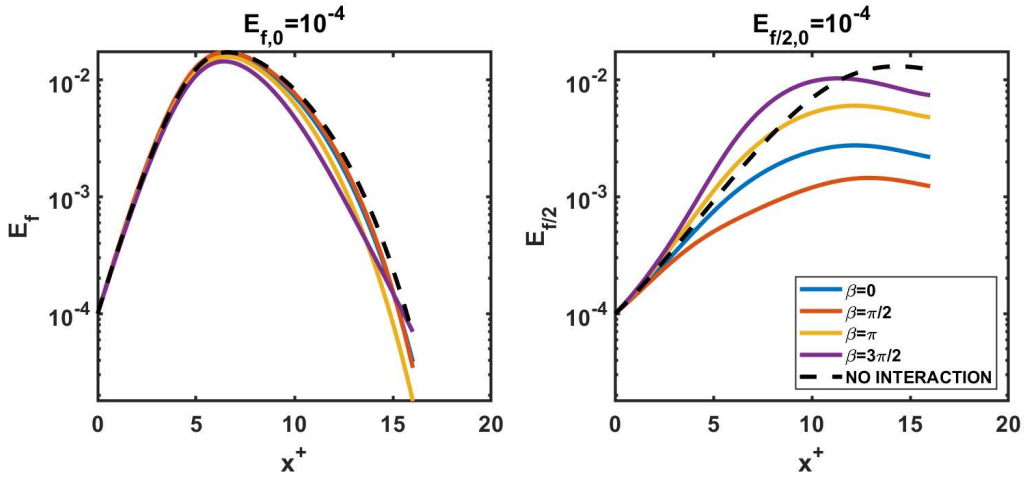

Figure 6.3 Amplitudes for St=0.10, 0.05; $E_{f,0} = 10^{-4}$, $E_{f/2,0} = 10^{-4}$

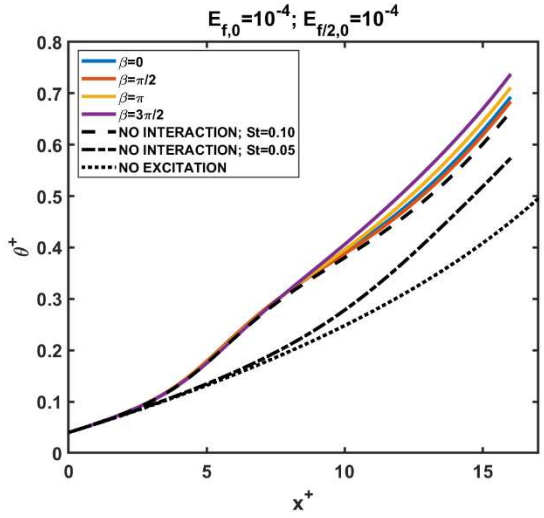

Figure 6.4 Momentum thickness versus streamwise location for St=0.10, 0.05 with $E_{f,0} = 10^{-4}$, $E_{f/2,0} = 10^{-4}$

Given that the interaction between the subharmonic and fundamental is relatively weak in reducing the fundamental mode, and that the subharmonic reaches an amplitude corresponding to that of the fundamental and persists over a larger streamwise distance, then this technique may or may not result in reducing the radiated sound. However, it is quite effective in enhancing the growth rate when the phase difference is optimized. The increase in the spreading rate of the jet has previously been shown in both computation and experiment (Mankbadi, 1991; Mankbadi et al., 1989).

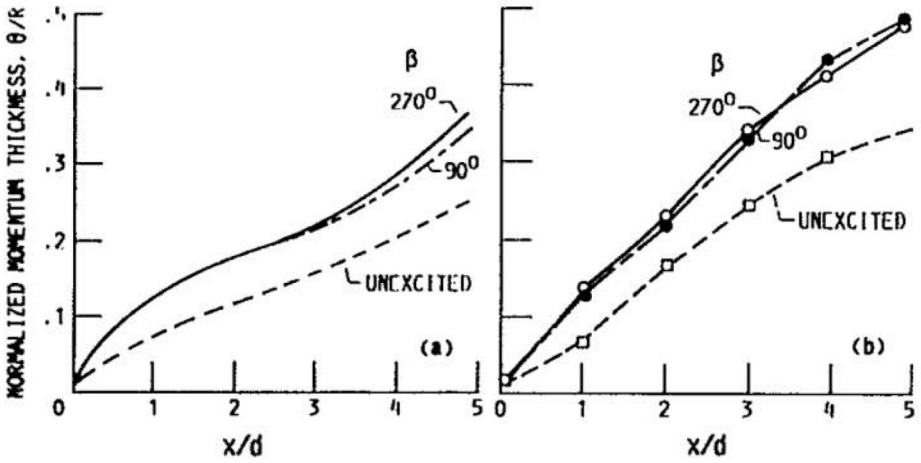

Figure 6.5 Jet momentum thickness with and without bi-modal excitation computation (left) (Mankbadi, 1991) and experiment (Mankbadi et al., 1989).

6.2 Reduction of the Fundamental Mode Via Harmonic Excitation

With the fundamental being at St=0.1, we now consider reducing it via a harmonic excitation at St =0.2. Thus, the interaction is between the Strouhal number pair, 0.10 and 0.20. We first consider the case when the excitation is at the same level as the fundamental, thus: $E_{2f,0} = E_{f,0}$, and is taken to be 10^{-5}, 10^{-4}, or 10^{-3}, and we vary the initial phase as done in Section 6.1.

In this case when we solve Equations 6.1-6.3, A^2 corresponds to the amplitude for harmonic Strouhal number 0.20, and B^2 corresponds to the fundamental Strouhal number of 0.10. At the harmonic Strouhal number of 0.20, the linear growth rate becomes damped at $\theta^+ \approx 0.15$, which can be seen in Figure 4.11. Consequently, there are only linear stability results up to $\theta^+ = 0.25$, which becomes the limit of our numerical scope here.

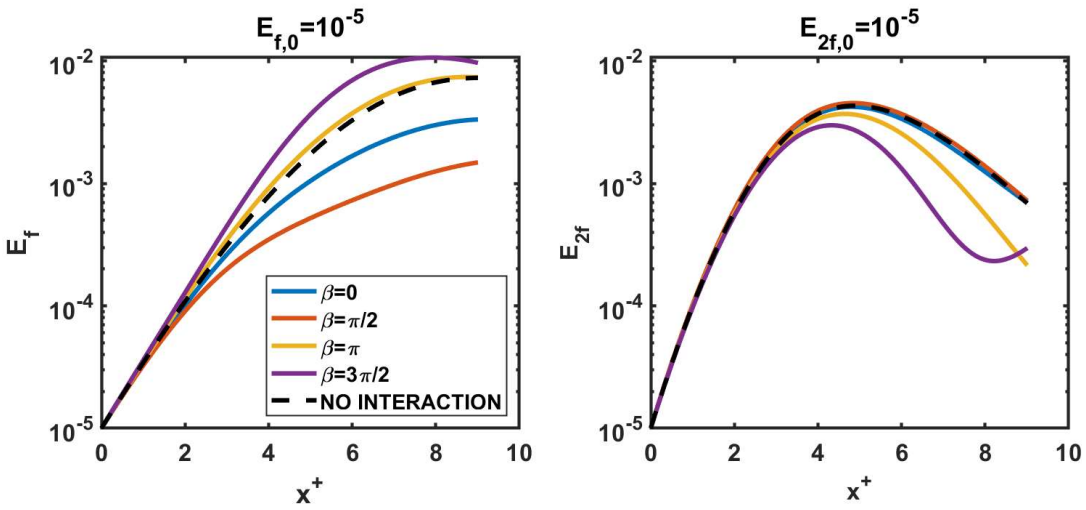

Figure 6.6 Amplitudes for St=0.10, 0.20; $E_{f,0} = 10^{-5}$, $E_{2f,0} = 10^{-5}$

Unlike with the fundamental-subharmonic pair examined previously, this damping of the fundamental resulting from the wave-wave interactions was clear even at low initial amplitudes as can be seen even when both initial amplitudes were 10^{-5}. To emphasize this point, we show in Figure 6.11, the case when the imposed amplitude is initially an order of magnitude less than that of the fundamental. We note that in this case, the momentum thickness growth is enhanced over the case with no coherent structure. In all

of the presented results in this set, the phase that reduced the fundamental the most also had a minimal effect on amplifying the harmonic.

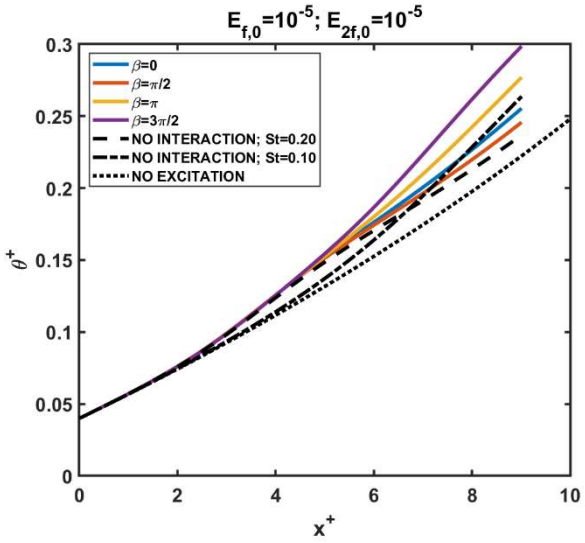

Figure 6.7 Momentum thickness versus streamwise location for St=0.10, 0.20 with $E_{f,0} = 10^{-5}$, $E_{2f,0} = 10^{-5}$

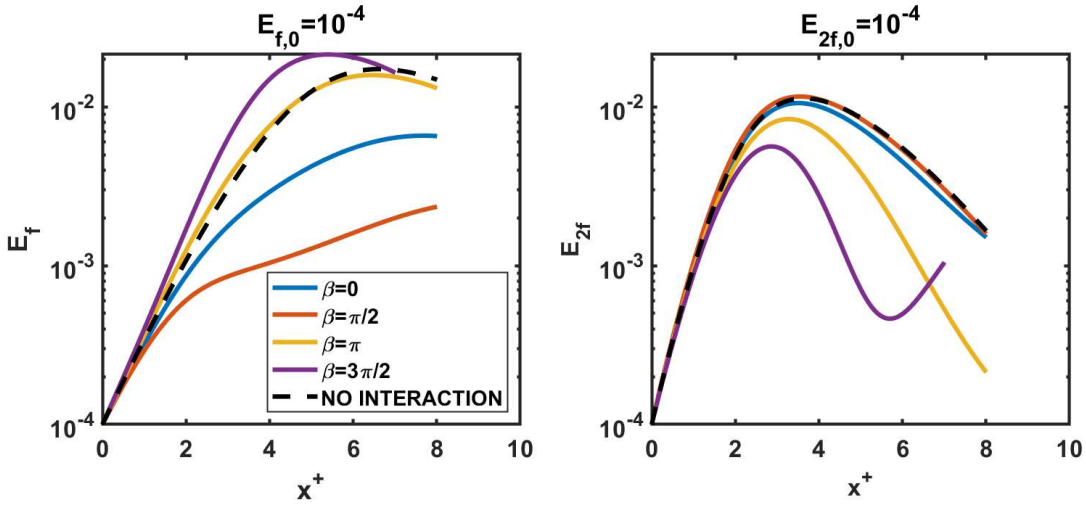

Figure 6.8 Amplitudes for St=0.10, 0.20; $E_{f,0} = 10^{-4}$, $E_{2f,0} = 10^{-4}$

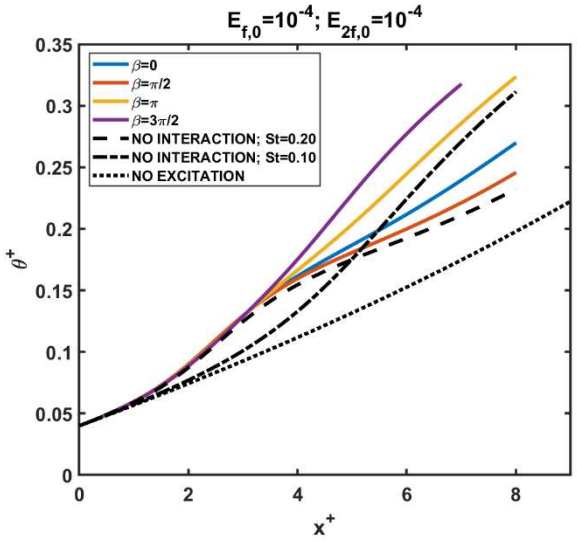

Figure 6.9 Momentum thickness versus streamwise location for St=0.10, 0.20 with $E_{f,0} = 10^{-4}$, $E_{2f,0} = 10^{-4}$

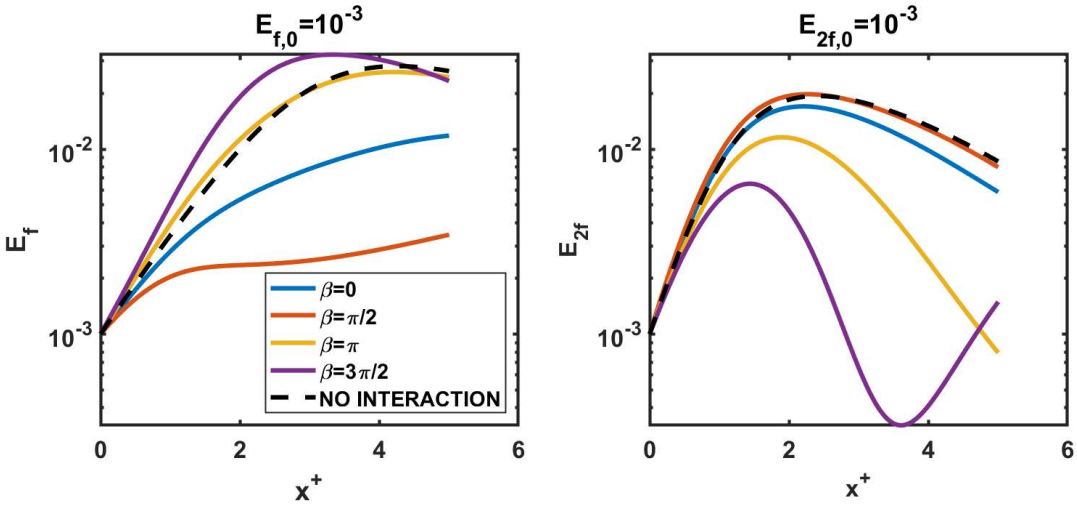

Figure 6.10 Amplitudes for St=0.10, 0.20; $E_{f,0} = 10^{-3}$, $E_{2f,0} = 10^{-3}$

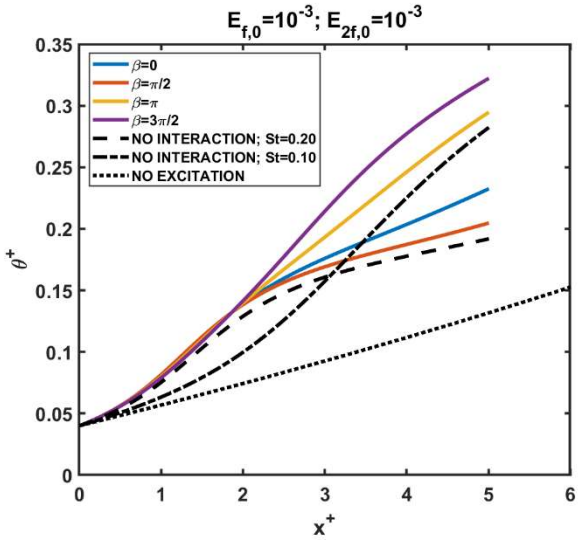

Figure 6.11 Momentum thickness versus streamwise location for St=0.10, 0.20 with $E_{f,0} = 10^{-3}$, $E_{2f,0} = 10^{-3}$

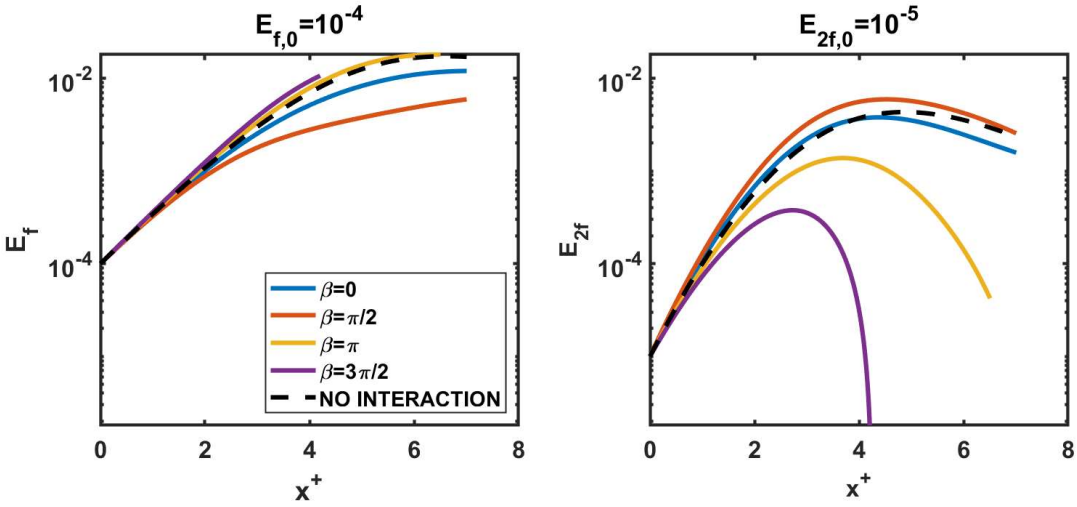

Figure 6.12 Amplitudes for St=0.10, 0.20; $E_{f,0} = 10^{-4}$, $E_{2f,0} = 10^{-5}$

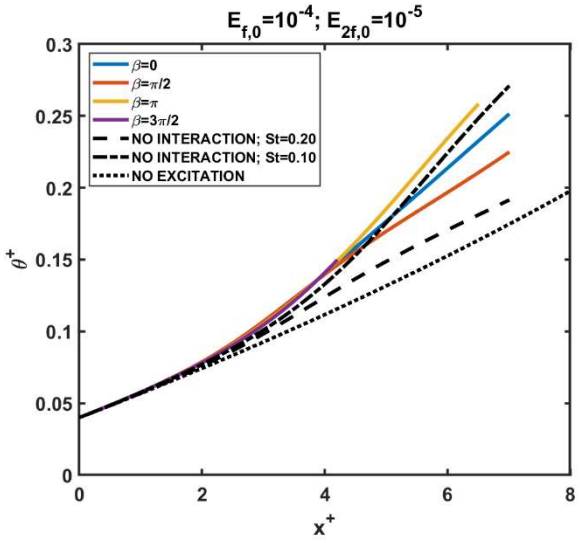

Figure 6.13 Momentum thickness versus streamwise location for St=0.10, 0.20 with $E_{f,0} = 10^{-4}$, $E_{2f,0} = 10^{-5}$

Unlike the case with subharmonic interaction, the interaction from the harmonic were able to reduce the amplitude of the fundamental when the initial amplitude was smaller than that of the fundamental. Though it should be noted that the interaction effects are less pronounced compared to when the initial amplitudes were equal as can be seen when comparing with Figure 6.7.

For all the cases presented in this section in Figures 6.5-6.12, we note that 1) The harmonic managed to produce significant reduction in the fundamental mode with the appropriate phase difference; and 2) the imposed mode reached peak is still much less than that of the fundamental, and its streamwise lifespan is short. So, the harmonic is not likely to cause significant increase in the radiated sound by itself. Thus, the peak radiated sound is projected to decrease as the fundamental has been significantly damped. We note that the effect is pronounced at $\beta = \frac{\pi}{2}$.

7. Conclusions

We considered here the case of a supersonic shear layer representing the initial shear layer of the minor axes of a heated rectangular jet. We developed a reduced-order model for the bi-modal excitation of the jet based on the nonlinear integral approach. In this model, we considered two frequency modes of the coherent structure interaction with each other as well as with the background turbulent jet flow. The model is based on modelling the large-scale coherent structure as a wave-packet that resembles nonlinear instability, where its transverse profile is obtained from the locally-parallel linear instability theory. The mean flow is represented by fitting a hyperbolic tangent profile to CFD data. With these shape assumptions, the compressible NSE can be reduced to a set of simultaneous ODE's representing the interaction of the two waves among themselves and the mean flow. The effect of the background turbulence is represented by an effective turbulent Reynolds number.

To understand the physics involved, we first considered the case of the nonlinear development of each structure frequency mode without considering their interaction with each other. Thus, their development is determined by their production by the mean flow and by their effective dissipation caused by the viscous and turbulence effects. In this case, the model is similar to that of the compressible Dahl and Mankbadi (2002) model. The present work, however, is considering the case of a 2D shear layer of rectangular jets as opposed to a round jet. Our results show the nonlinear effect in this case results in reducing the amplification of each mode, and that this reduction is more pronounced with increasing the initial level of the mode, which agrees with previous studies (Dahl & Mankbadi, 2002). Both the linear and nonlinear growth have indicated that the most

amplified mode along the jet is St=0.1. CFD simulations of Mankbadi and Salehian (2021) of the same jet have also shown that St=0.1 corresponds to the peak of the radiated sound.

We then presented results with focus on how to use the excitation to reduce the fundamental mode. The fundamental mode is defined here as the dominant noise source that results in the peak in the noise spectra.

We have presented results for bi-modal excitation with both the subharmonic and harmonic frequencies. Our objective is to reduce the streamwise peak of the amplitude of the fundamental Strouhal number, which is taken to be the dominant noise source. The additional of the subharmonic or harmonic should be done with an initial amplitude equal to or less than that of the fundamental, to prevent the addition of another significant noise source.

We first examined the addition of the subharmonic mode. Here, we observed some reduction in the peak of the fundamental mode with higher initial amplitudes, though this reduction is not very pronounced. Thus, it is not clear whether this mechanism is effective in reducing the peak noise of the jet. However, our computations show that the addition of the subharmonic has a significant effect on the growth of momentum thickness, which will lead to a reduction in the potential core.

We then considered reducing the fundamental mode with the addition of its harmonic. This was found to be very effective in reducing the fundamental mode for optimized values of the phase angle, β. It was found that the fundamental was reduced the most for $\beta = \frac{\pi}{2}$. Even with significant reduction in the fundament, there was not a significant increase in the amplitude of the harmonic. Thus, we believe that imposing the harmonic

on the fundamental will be an effective mechanism for noise reduction. Additionally, the addition of the harmonic increased the spreading of the jet, compared to the case with single-mode excitation at the fundamental Strouhal number and without excitation.

REFERENCES

Arbey, H. & Ffowcs Williams, J.E., "Active Cancellation of Pure Tones in an Excited Jet", Journal of Fluid Mechanics, vol. 149, pp. 445-454, 5 June 1984.

Chakrabarti, S., Unnikrishnan, S., Gaitonde, D., Stack, C., Baier, F., Karnam, A., Gutmark, E., (2020a) "On the Turbulence Statistics of a Hot, Overexpanded Rectangular Jet", AIAA SciTech 2020 Forum, 6-10 January 2020

Chakrabarti, S., Gaitonde, D., Unnikrishnan, S., (2020b) "The Dynamics of Azimuthal Modes in Rectangular Jets", AIAA Aviation 2020 Forum, 15-19 June 2020.

Chang, C. "Langley Stability and Transition Analysis Code (LASTRAC) Version 1.2 User Manual", NASA/TM-2004-213233, June 2004

Crawley, M., Sinha, A., Samimy, M., "Near-Field and Acoustic Far-Field Response of a High-Speed Jet to Excitation," AIAA Journal, Vol. 53, No. 7, July 2015.

Crawley, M., Kearney-Fischer, M., Samimy, M., "Control of a Supersonic Rectangular Jet using Plasma Actuators", 18th AIAA/CEAS Aeroacoustics Conference, 04-06 June 2012.

Dahl, M.D., Hixon, R., Mankbadi, R.R., "Computation of Large-Scale Structure Jet Noise Sources with Weak Nonlinear Effects Using Linear Euler", 9th AIAA/CEAS Aeroacoustics Conference and Exhibit, 12-14 May 2003.

Dahl, M.D. & Mankbadi, R.R., "Analysis of Three-Dimensional, Nonlinear Development of Wave-Like Structure in a Compressible Round Jet", 8th AIAA/CEAS Aeroacoustics Conference & Exhibit, 17-19 June 2002.

Lee & Liu, "Mixing Enhancement in High-Speed Turbulent Shear Layers, Using Excited Coherent Modes", AIAA Journal, Vol. 36, No. 11, November 1998.

Mankbadi, R.R., "Multifrequency Excited Jets", Physics of Fluids A: Fluid Dynamics 3, 595, April 1991, DOI: 10.1063/1.858121.

Mankbadi, R.R., "On the Interaction Between Fundamental and Subharmonic Instability Waves in a Turbulent Round Jet", Journal of Fluid Mechanics (1985), vol. 160, pp. 385-419.

Mankbadi, R.; Raman, G.; and Rice, E., "Phase development and its role on subharmonic control," Proceedings of the 28th Aerospace Sciences Meeting, March 1989. DOI: 10.2514/6.1990-503.

Mankbadi, R.R., & Salehian, S., "A Proposed Wavy Shield for Suppression of

Supersonic Jet Noise Utilizing Reflections", International Journal of Aeroacoustics, vol. 20, 2021.

Mora, P., Baier, F., Gutmark, E.J., Kailasanath, K., "Acoustics from a Rectangular C-D Nozzle Exhausting Over a Flat Surface", 54th AIAA Aerospace Sciences Meeting, 4-8 January 2016.

Nichols, J.W., Ham, F.E., Lele, S.K., "High-Fidelity Large-Eddy Simulation for Supersonic Rectangular Jet Noise Prediction", 17th AIAA/CEAS Aeroacoustics Conference, 05-08 June 2011.

Reynolds, W.C., & Hussain, A.K.M.F., "The Mechanics of an Organized Wave in Turbulent Shear Flow. Part 3. Theoretical Models and Comparisons with Experiments", Journal of Fluid Mechanics, vol. 54, pp. 263-288, 1972.

Salehian, S. & Mankbadi R. (2020a), "Jet Noise in Airframe Integration and Shielding", Applied Sciences, Vol. 10, Issue 511, 10 January 2020

Salehian, S. & Mankbadi, R. (2020b), "A Review of Aeroacoustics of Supersonic Jets Interacting with Solid Surfaces", AIAA SciTech 2020 Forum, 6-10 January 2020.

Samimy, M., Kearney-Fischer, J. Kim, H., and Sinha, A., "High-Speed and High-Reynolds-Number Jet Control Using Localized Arc Filament Plasma Actuators," Journal of Propulsion and Power, Vol. 28, No. 2, March–April 2012.

Samimy, M., Webb, N., Crawley, M., "Excitation of Free Shear-Layer Instabilities for High-Speed Flow Control", AIAA Journal, Vol. 56, No. 5, May 2018.

Schilchting, H., "Boundary Layer Theory", McGraw-Hill, New York, 1960.

Thomas, P.D., "Numerical Simulations for Predicting Flow Characteristics and Performance of Non-axisymmetric Nozzles, Theory", NASA CR-3147 Wind-US, 1979.

Wu, G.J., Lele, S.K., Jeun, J., "Towards Large Eddy Simulations of Supersonic Rectangular Jets Including Screech", 25th AIAA CEAS Aeroacoustics Conference, 20-23 May 2019.

APPENDIX A – LASTRAC Description

NASA's Langley Stability and Transition Analysis Code (LASTRAC) was used to obtain the linear stability results for the planar jet described in Chapter 4. The code is capable of handling both boundary layers and shear layers. Both linear stability and parabolized stability theory can be used. For the present work, linear stability analysis features were used for the shear layer. Below is a brief description of the governing equations, linear stability theory, and boundary conditions used in our analysis. A more in-depth description of the full capabilities and validation cases for LASTRAC can be found in Chang (2004).

A.1. Governing Equations

In general, x represents the streamwise direction, y represents the wall-normal direction, and z represents the spanwise direction. Elements of length are then represented by $h_1 dx$, dy, and $h_3 dz$ for the x-, y-, and z-direction respectively (Chang, 2004). To model the evolution of the disturbances, we start with the compressible Navier-Stokes equations

$$\frac{\partial \rho}{\partial t} + \nabla \cdot \left(\rho \vec{V}\right) = 0 \tag{A1}$$

$$\rho\left[\frac{\partial \vec{V}}{\partial t} + \vec{V} \cdot \nabla \vec{V}\right] = -\nabla p + \frac{1}{Re}\left(\nabla\left[\lambda\left(\nabla \cdot \vec{V}\right)\right] + \nabla \cdot \left[\mu\left(\nabla \vec{V} + \nabla \vec{V}^T\right)\right]\right) \tag{A2}$$

$$\rho C_p\left[\frac{\partial T}{\partial t} + \left(\vec{V} \cdot \nabla\right)T\right] = \nabla \cdot (k \nabla T) + \frac{\partial p}{\partial t} + \left(\vec{V} \cdot \nabla\right)p + \frac{\Phi}{Re} \tag{A3}$$

Here, μ and λ are the first and second coefficient of viscosity, respectively. Viscous dissipation, Φ, is defined by:

$$\Phi = \lambda\left(\nabla \cdot \vec{V}\right)^2 + \frac{\mu}{2}\left[\nabla \vec{V} + \nabla \vec{V}^T\right]^2 \tag{A4}$$

λ can be related to μ by the Stokes parameter, s:

$$\lambda = \frac{2}{3}(s-1)\mu \tag{A5}$$

The ideal gas relation is used as the equation of state.

$$p = \rho RT \tag{A6}$$

The Navier-Stokes equations in Equations A1-A3 are non-dimensionalized. Lengths are scaled by length scale, l, velocity by u_e, density by ρ_e, pressure by $\rho_e u_e^2$, temperature by T_e, viscosity by μ_e, and time by l/u_e. For jet flows, the values at the jet exit are used.

The variables in the Navier Stokes equations can be split into a mean flow and disturbance fluctuation in the general form:

$$q = \bar{q} + q' \tag{A7}$$

where q can represent $u, v, w, p, \rho, T, \mu, \lambda, k$. These quantities can be substituted into the Navier Stokes equations, and the mean flow can be subtracted out. This gives the governing equation for the disturbances:

$$\Gamma\frac{\partial \phi}{\partial t} + \frac{A}{h_1}\frac{\partial \phi}{\partial x} + B\frac{\partial \phi}{\partial y} + \frac{C}{h_3}\frac{\partial \phi}{\partial y} + D\phi = \frac{1}{Re_0}\left(\frac{V_{xx}}{h_1^2}\frac{\partial^2 \phi}{\partial x^2} + \frac{V_{xy}}{h_1}\frac{\partial^2 \phi}{\partial y^2} + V_{yy}\frac{\partial^2 \phi}{\partial y^2} + \frac{V_{xz}}{h_3}\frac{\partial^2 \phi}{\partial x \partial z} + \frac{V_{yz}}{h_3}\frac{\partial^2 \phi}{\partial y \partial z} + \frac{V_{zz}}{h_3^2}\frac{\partial^2 \phi}{\partial z^2}\right) \tag{A8}$$

where ϕ is the disturbance vector defined by:

$$\phi = (p', u', v', w', T')^T \tag{A9}$$

In Equation A8, $\Gamma, A, B, C, D, V_{xx}, V_{yy}$, etc. are the Jacobians of the flux vectors and $Re_0 = u_e l_0/\nu_e$ which is used to normalize the equations. The disturbance vector, ϕ, can be expressed by a discrete Fourier Series.

$$\phi(x, y, z, t) = \sum_{m=-M}^{M}\sum_{n=-N}^{N} \chi_{nm}(x, y) e^{i(n\beta z - m\omega t)} \tag{A10}$$

In Equation A10, ω and β are the temporal and spanwise wave numbers. M and N are the Fourier modes considered in time and space. χ_{nm} is the mode shape of mode (m, n). Wave number can be related to a physical frequency by:

$$\omega = \frac{2\pi l}{u_e} f \tag{A11}$$

The spanwise wave number, β, is defined by

$$\beta = \frac{2\pi}{\lambda_z} \tag{A12}$$

where λ_z is the spanwise wavelength normalized by l_0. When the disturbance amplitude is small, it is assumed that the Fourier modes evolve independently, and nonlinear interaction of the modes is negligible. Equation A8 can then be written in the linearized form:

$$\Gamma^l \frac{\partial \phi}{\partial t} + \frac{A^l}{h_1}\frac{\partial \phi}{\partial x} + B\frac{\partial \phi}{\partial y} + \frac{C^l}{h_3}\frac{\partial \phi}{\partial z} + D^l \phi = \frac{1}{Re_0}\left(\frac{V_{xx}^l}{h_1^2}\frac{\partial^2 \phi}{\partial x^2} + \frac{V_{xy}^l}{h_1}\frac{\partial^2 \phi}{\partial y^2} + V_{yy}^l \frac{\partial^2 \phi}{\partial y^2} + \frac{V_{xz}^l}{h_3}\frac{\partial^2 \phi}{\partial x \partial z} + \frac{V_{yz}^l}{h_3}\frac{\partial^2 \phi}{\partial y \partial z} + \frac{V_{zz}^l}{h_3^2}\frac{\partial^2 \phi}{\partial z^2}\right) \tag{A13}$$

A single disturbance mode can be expressed as

$$\phi = \chi(x, y) e^{i(\beta z - \omega t)} \tag{A14}$$

Equation A14 can be substituted into Equation A13 to give the linearized Navier-Stokes equation, which is a set of constant coefficient PDE's.

$$\left(\frac{A^l}{h_1} - \frac{i\beta V_{xz}^l}{h_3 Re_0}\right)\frac{\partial \chi}{\partial x} + \left(B^l - \frac{i\beta V_{yz}^l}{h_3 Re_0}\right)\frac{\partial \chi}{\partial y} + \left(D^l - i\omega\Gamma^l + \frac{i\beta C^l}{h_3} + \frac{\beta^2 V_{zz}^l}{h_3^2 Re_0}\right)\chi = \frac{1}{Re_0}\left(\frac{V_{xx}^l}{h_1^2}\frac{\partial^2 \chi}{\partial x^2} + \frac{V_{xy}^l}{h_1}\frac{\partial^2 \chi}{\partial x \partial y} + V_{yy}^l \frac{\partial^2 \chi}{\partial y^2}\right) \tag{A15}$$

To solve the linearized Navier Stokes equation numerically, the solution is discretized in the x and y directions.

$$A_{lns}\phi_{lns} = f_{lns} \tag{A16}$$

where ϕ_{lns} is the solution vector, and f_{lns} is the forcing vector associated with the boundary conditions. A_{lns} is a banded or full block matrix depending on the scheme used for discretization.

A.2. Quasi-Parallel Linear Stability Theory

In quasi-parallel linear stability theory, it is assumed that the mean flow evolves slowly in the streamwise direction relative to the normal direction. Thus, it is assumed that the mean flow variation in x is negligible. A shape assumption is then made taking the following form:

$$\chi(x, y) = \psi(y)e^{i\alpha x} \tag{A17}$$

This leads to:

$$\phi(x, y, z, t) = \psi(y)e^{i(\alpha x+\beta z-\omega\ )} \tag{A18}$$

Here, α is the local streamwise wave number at a particular streamwise station. Equation A18 can be substituted into Equation A15. The mean wall-normal velocity component and viscous terms that are on the order of $\frac{1}{Re_0^2}$ or lower are neglected. These yields:

$$\left(B^l + \frac{i\beta V_{yz}^l}{h_3 Re_0} - \frac{i\alpha V_{xy}^l}{h_1 Re_0}\right)\frac{d\psi}{dy}$$
$$+\left(D^l - i\omega\Gamma^l + \frac{i\alpha A^l}{h_1} + \frac{\alpha^2 V_{xx}^l}{h_1^2 Re_0} - \frac{i\beta V_{xz}^l}{h_3 Re_0} + \frac{i\beta C^l}{h_3} + \frac{\beta^2 V_{zz}^l}{h_3^2 Re_0}\right)\psi = \frac{V_{yy}^l}{Re_0}\frac{d^2\psi}{dy^2} \tag{A19}$$

Equation A19 is ultimately what is of interest here with our application of the LASTRAC code. Equation A19 is a set of ODE's. It constitutes an eigenvalue problem with the following dispersion relation:

$$\alpha = \alpha(\omega, \beta) \tag{A20}$$

LASTRAC formulates the stability calculations as a spatial stability problem. For a given disturbance frequency, ω, and wave number, β, the complex eigenvalue, $\alpha = \alpha_r + i\alpha_i$, is solved for numerically. If $\alpha_i < 0$, the eigenmode is unstable.

A.3. Boundary Conditions

LASTRAC uses a central differencing scheme, and thus uses the continuity equation as a 5th auxiliary equation. In the free-stream, Dirichlet boundary conditions are used.

$$\hat{u} = \hat{v} = \hat{w} = \hat{T} = 0, \quad y \to \infty \tag{A21}$$

Equation A22 works well for subsonic modes. For supersonic modes, there is a non-decaying oscillatory structure in the free stream, which causes spurious reflections. For supersonic flows, LASTRAC uses a non-reflecting boundary condition in the far field. This non-reflecting boundary condition is derived from the inviscid Euler equations since it is assumed that viscous effects are negligible in the far field. For supersonic flows in the far field, the disturbance equation takes the following form:

$$\Gamma\frac{\partial \phi}{\partial t} + \frac{A}{h_1}\frac{\partial \phi}{\partial x} + B^+\frac{\partial \phi}{\partial y} + \frac{C}{h_3}\frac{\partial \phi}{\partial z} + D\phi = 0 \tag{A22}$$

B^+ is defined as:

$$B^+ = \Gamma(L\Lambda^+ L^{-1}) \tag{A23}$$

In Equation A23, L is the left eigenvector matrix of the product of the coefficient matrix, $\Gamma^{-1}B$. Λ^+ is the modified diagonal eigenvalue matrix.

$$\Lambda^+ = diag\big(\max(0, \lambda_j)\big) \tag{A24}$$

λ_j are the eigenvalues of $\Gamma^{-1}B$.

In LASTRAC, the equations are discretized via a 1st-order scheme in the streamwise direction and 4th-order central difference scheme in the wall-normal direction. The solution is obtained in a two-step process. In the first step, the viscous terms are

neglected to recast the equation in linear form that can be solved as an eigenvalue problem. The obtained global eigenvalue spectrum generally contains all discrete modes as well as the continuous spectrum. Once the global eigenvalues are obtained, a local eigenvalue search is performed using the results from the global search as a starting point for the viscous solution using the iterative Newton's method applied to the governing equations.

APPENDIX B – Large-Eddy Simulations of Mach 1.5 Planar Jet

To later validate the results from Chapters 5 and 6, large eddy simulations (LES) are to be performed on a Mach 1.5 heated planar jet. This is done using the Air Force Research Lab's (AFRL) FDL3DI code.

B.1 Code Description

AFRL's FDL3DI code is an implicit LES code. It solves the compressible Navier-Stokes equations in conservative form.

$$\frac{\partial}{\partial t}\left(\frac{\vec{Q}}{J}\right)+\frac{\partial \overrightarrow{F_i}}{\partial \xi}+\frac{\partial \overrightarrow{G_i}}{\partial \eta}+\frac{\partial \overrightarrow{H_i}}{\partial \zeta}-\frac{1}{Re}\left[\frac{\partial \overrightarrow{F_v}}{\partial \xi}+\frac{\partial \overrightarrow{G_v}}{\partial \eta}+\frac{\partial \overrightarrow{H_v}}{\partial \zeta}\right]=\vec{S} \tag{B1}$$

$$\vec{Q}=(\rho,\rho u,\rho v,\rho w,\rho e) \tag{B2}$$

$$e=\frac{T}{\gamma(\gamma-1)M_\infty^2}+\frac{1}{2}(u^2+v^2+w^2) \tag{B3}$$

$$p=\frac{\rho T}{\gamma M_\infty^2} \tag{B4}$$

The code uses a 6th order accurate compact differencing scheme in space and a 2nd order implicit time marching scheme. The code also has efficient grid moving capabilities though these are not used in this work. There is a plethora of boundary conditions that the code comes standard with including: no-slip adiabatic wall, inviscid wall, subsonic inflow/outflow based on Riemann invariants, uniform flow at an angle of attack, quiescent fluid, extrapolation of all variables, Dirichlet conditions from initial values, symmetry plane, and many more. With the source code, user-defined boundary conditions can also be defined.

B.2 Case Setup

Here, a perfectly expanded Mach 1.5 heated planar jet is being modeled. At the inlet, a modified version of the uniform flow at an angle of attack boundary condition was used. The modification allows for the additional prescription of temperature. The jet from Salehian and Mankbadi (2020) has a total temperature ratio of 3, which gives a static temperature ratio of 2.075 for Mach 1.5. The grid generated for this computation is composed of around 1.1 million cells. This inlet was prescribed along the left-hand side of the computational domain between $y = [-0.5, 0.5]$. It should be noted that although we are using a length scale of $H/2$ in the linear stability analysis and results to the ODE, FDL3DI scales based on a length scale equal to the heigh of the jet and thus desires a jet height of 1. 1st order extrapolation of variables was prescribed at every other boundary. The grid along with the boundary conditions can be seen below. The case was run with a time step of $\Delta t = 0.000045\ s$.

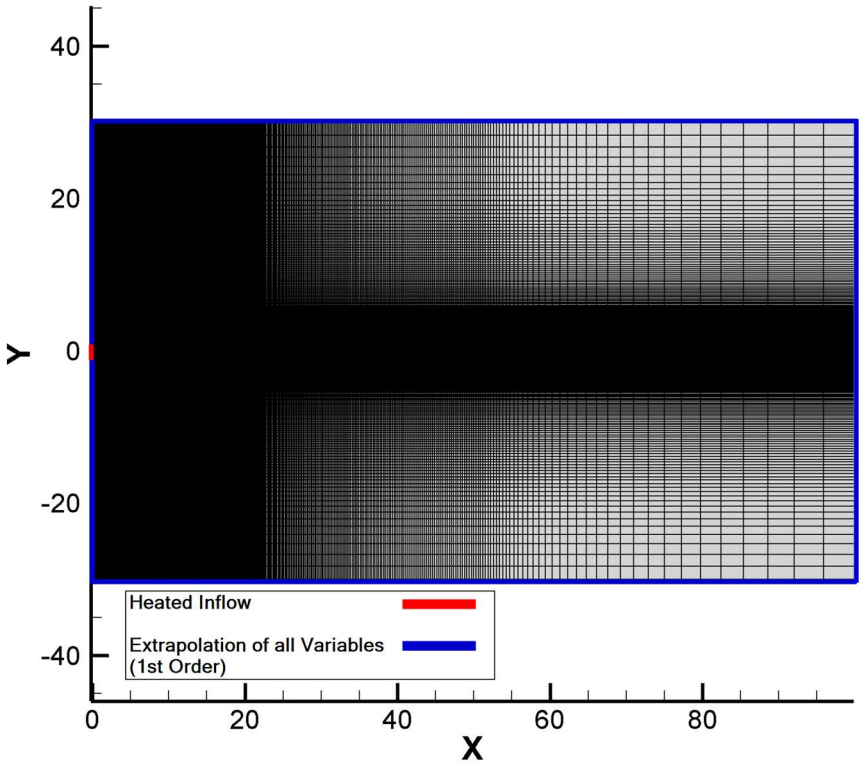

Figure B1 Computational grid with boundary conditions

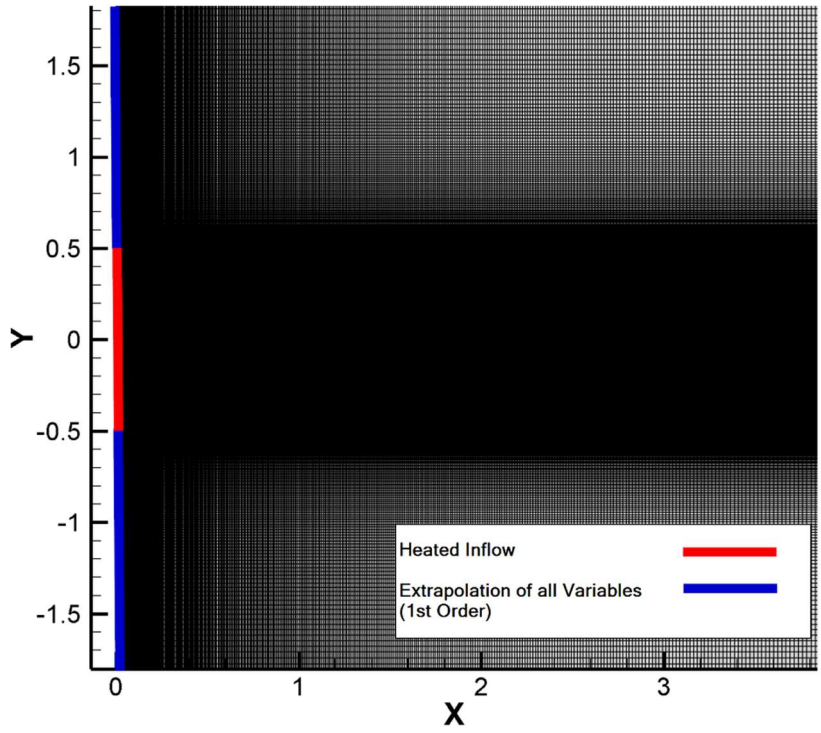

Figure B2 Magnified computational grid with boundary conditions

B.3 Results

Images below show contours for the time averaged u-velocity, temperature, and pressure. Ideally, these results should be symmetrical about $y = 0$ However, it is clear that this is not the case with the present results, indicating that there is still some work to be done with the LES.

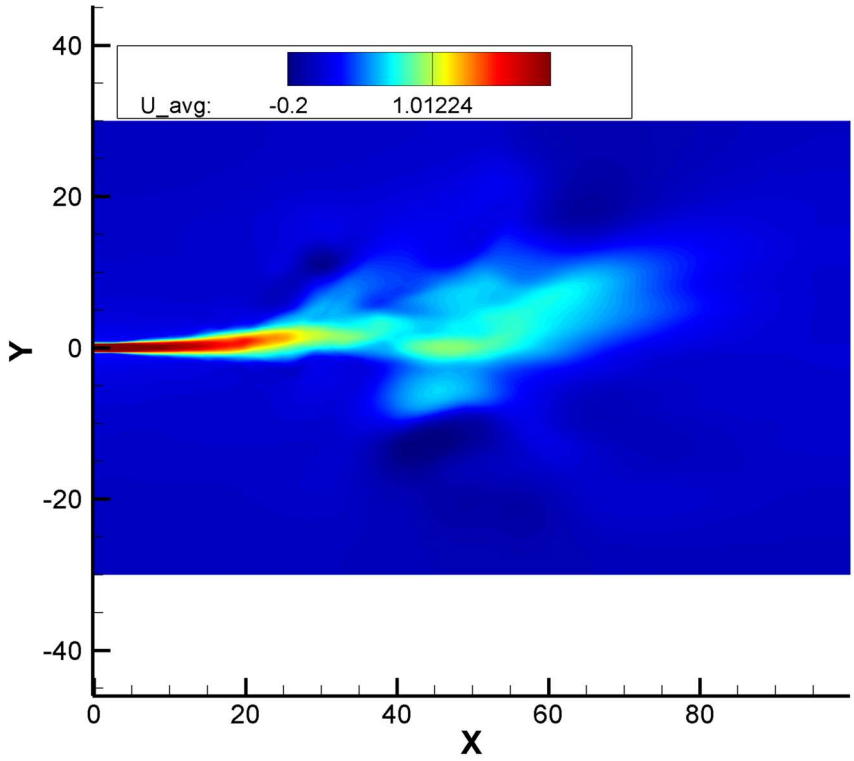

Figure B3 Time averaged u-velocity contour for Mach 1.5 planar jet LES

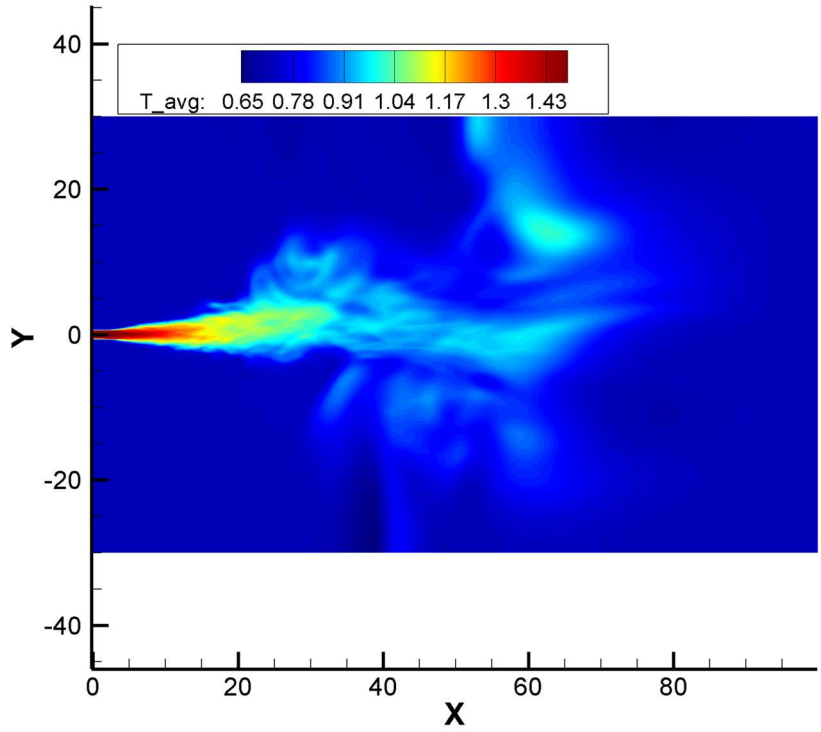

Figure B4 Time averaged temperature contour for Mach 1.5 planar jet LES

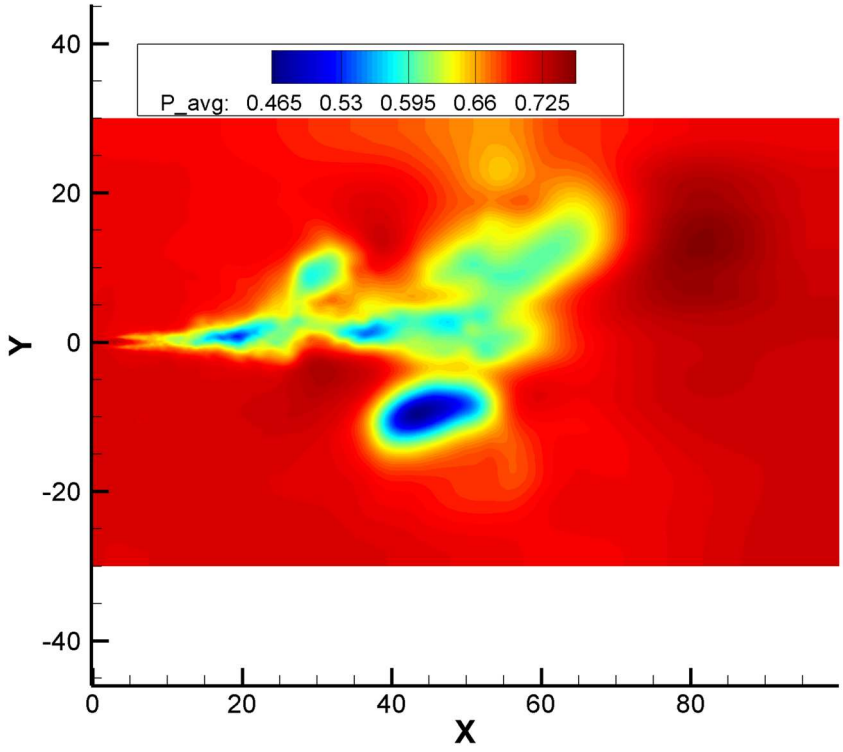

Figure B5 Time averaged pressure contour for Mach 1.5 planar jet LES

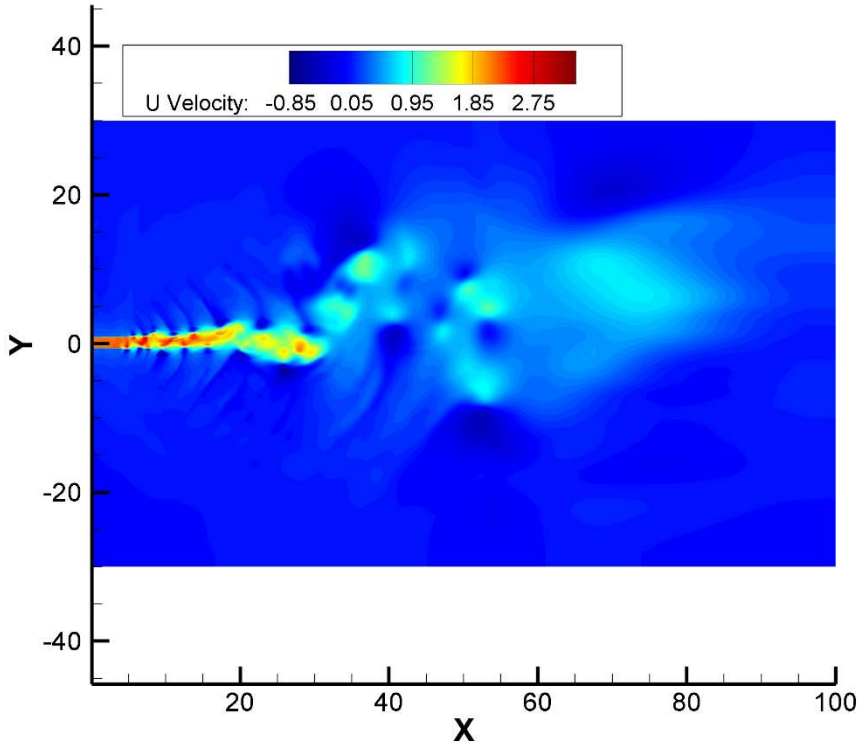

Figure B6 Snapshot contour of u-velocity for Mach 1.5 planar jet LES

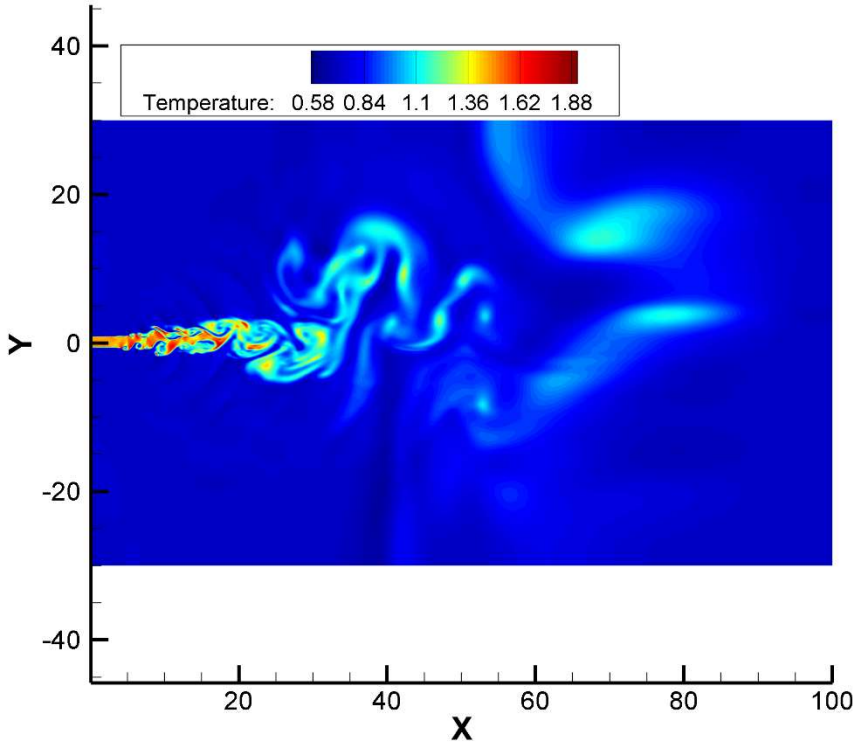

Figure B7 Snapshot contour of temperature for Mach 1.5 planar jet LES

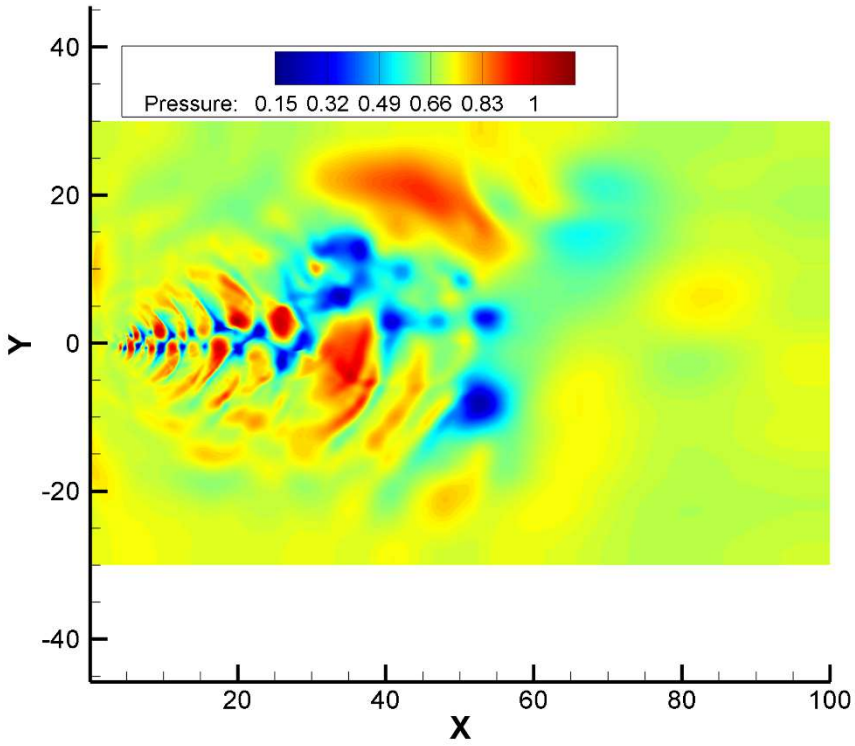

Figure B8 Snapshot contour of pressure for Mach 1.5 planar jet LES